EQUATIONS OF MOTION FOR REACTING, PARTICLE-LADEN FLOWS

Thermal Science Ltd.

December 1991

CONTRACT SERIAL NO. 23440-7-9130-01-SQ
ONTRACTOR: THERMAL SCIENCES LIMITED
TITLE: COMPUTATION OF RADIANT HEAT TRANSFER ON A NON-ORTHOGONAL MESH USING THE FINITE VOLUME METHOD (Dec. 27/91) see other part of report TITLE: MODELLING OF PULVERIZED COAL ETC.

Computation of Radiant Heat Transfer on a Non-Orthogonal Mesh using The Finite Volume Method

by

E.H. Chui and G.D. Raithby

Department of Mechanical Engineering
University of Waterloo
Waterloo, Ontario
Canada N2L 3G1

December 27, 1991

180 pp

MICROMEDIA

93-01529/

ABSTRACT

The Finite Volume Method has been shown to effectively predict radiant exchange in geometrically simple enclosures where the medium is gray, absorbing, emitting, and scattering. Cartesian and circular cylindrical meshes have always been used. The present paper shows that the method applies equally well to geometrically complex enclosures where non-orthogonal, boundary-fitted meshes are used. This development permits radiant heat transfer to be computed on the same mesh employed to solve the equations of fluid motion.

NOMENCLATURE

A_f	area of surface panel f, m^2
I	radiant intensity, $W/(m^2\ sr)$
I^i	in-scattering intensity, Eqs. (2) and (7)
I_b	blackbody intensity, $\sigma T^4/\pi$
I_B	intensity at ~~surface control volume~~ boundary
I^i_{if}	intensity at integration point if within ω^i
I^i_P	intensity at node P within ω^i
I^i_{uf}	upstream intensity for integration point on surface panel f within ω^i
K_a	absorption coefficient, $1/m$
N_x, N_y	number of control volumes in the x, and y directions
N_θ, N_ϕ	number of control volumes in polar (θ) and azimuthal (ϕ) directions
$\vec{n}$	unit normal to a surface of control volume
q	radiant heat flux, W/m^2
Q^i_f	radiant energy within ω^i crossing surface panel f, W
$\vec{r}$	position vector
R^i	the intensity sourc function within ω^i, Eq. (6)
s	distance in direction of $\vec{s}$, m
$\vec{s}$	unit vector in direction of intensity
S	path length, m
T	temperature, K
V	volume, m^3
w_i	weight on node i within a quadrilateral element based on bilinear approximation, Eq. (9)
x, y, z	Cartesian coordinates

Greek Symbols

β, γ	local coordinates for a quadrilateral element, Fig. 2A
δ	Kronecker delta function
ϵ	emissivity
θ	polar angle measured from z axis

κ	extinction coefficient, $K_a + \sigma_s, 1/m$
σ	Stefan-Boltzmann's constant
σ_s	scattering coefficient, $1/m$
ϕ	azimuthal angle measured from x axis in $x-y$ plane
Φ	scattering phase function, Eq. (2)
$\bar{\Phi}$	new variable for phase function, Eq. (8)
ψ	scattering angle, between $\vec{s}$ and $\vec{s'}$ in Eq. (2)
ω_s	scattering albedo, $\sigma_s/(\sigma_s + K_a)$
ω	solid angle, sr

Subscripts and Superscripts

b	refers to blackbody
f	refers to panel f on the surface of a control volume
if	refers to the integration point on surface panel f
l	associated with discrete solid angle ω^l
nb	refers to neighboring volumes
N, S, E, W	refer to north, south, east, west
NW, NE, SW, SE	refer to northwest, northeast, southwest, southeast
P	refers to nodal point P
uf	interpolation location for intensity upstream of point if
w	enclosure wall

INTRODUCTION

To predict the fluid flow and convective heat transfer in the geometrically complex systems of practical interest, computational methods are normally implemented on non-orthogonal, boundary-fitted meshes. Many such problems also require prediction of the radiant heat transfer, where the medium affects the heat transfer through emission, absorption and scattering. The Radiative Transfer Equation (or RTE) governs this radiant exchange. Although it is desirable to solve this equation on the same computational mesh used for the fluid flow, there has been very little discussion in the literature on solution methods that use non-orthogonal meshes (see reviews by Howell [1] and Viskanta and Mengüç [2]). The Spherical Harmonics Method (Mengúç and Viskanta [3], [4]), the Discrete Ordinate Method (Fiveland [5]), the Zonal Method (Larsen and Howell [6]), the Six Flux Method (Siddal and Selçuk [7]), and the Discrete Transfer Method of Lockwood and Shah [8] are all presented using rectangular or cylindrical meshes.

The Finite Volume Method (FVM), developed by the present authors, has also been applied only on Cartesian (Raithby and Chui [9]) and cylindrical (Chui et al [10]) meshes. The goal of this paper is to demonstrate the application of this method on non-orthogonal, quadrilateral element meshes.

Several features make the FVM attractive for the present purposes. The method was originally derived with non-orthogonal meshes in mind. It also guarantees global conservation of radiant energy, and captures the diffusion limit exactly for a strongly participating medium. The FVM has been shown to give accurate results for rectangular and cylindrical enclosures, anisotropic scattering is easy to treat, and rapid convergence can be achieved over a large range of optical thickness (Chui and Raithby [11]).

In the sections that follow, the discretization of the RTE on the non-orthogonal mesh is described, a new solution procedure is outlined, details related to special treatment at the boundaries are given, and the results of four test problems are presented. For simplicity only two-dimensional problems are considered, and the medium is assumed to be gray.

RADIATIVE TRANSFER EQUATION

The transfer of radiant energy is governed by the radiative transfer equation (RTE) (Siegel and Howell, [12]):

$$\frac{dI(\vec{r},\vec{s})}{ds} = -(K_a + \sigma_s)I(\vec{r},\vec{s}) + K_a I_b(\vec{r}) + \sigma_s \bar{I}(\vec{r},\vec{s}) \qquad (1)$$

It describes the variation of radiant intensity $I(\vec{r},\vec{s})$ at location $\vec{r}$ in direction $\vec{s}$. The four terms on the right side account for absorption, outscattering, emission and inscattering respectively. The inscattering term is defined by

$$\sigma_s \bar{I}(\vec{r},\vec{s}) = \frac{\sigma_s}{4\pi}\int_{4\pi} I(\vec{r},\vec{s'})\Phi(\vec{s},\vec{s'})d\omega' \qquad (2)$$

where $I(\vec{r},\vec{s'})$ is the incident intensity from direction $\vec{s'}$ and Φ is the scattering phase function between $\vec{s'}$ and $\vec{s}$.

The principal goal here is to obtain a discrete representation of I both in space and direction using a finite volume approach.

SPATIAL GRID

Figure 1A shows how an irregular geometry can be subdivided using a mesh made up of quadrilateral 'elements'. Each grid line intersection defines a node, denoted by a heavy dot. All dependent variables are stored at the nodes, and the equation for each variable is obtained from its discretized conservation equation for a volume surrounding the node. The volume associated with an interior node, like P in Fig. 1A, is the sum of the four cross-hatched quadrants shown in Fig. 1B. The outside surfaces of the quadrants (the dashed lines) lie along lines that join the midpoints of opposite sides of the element. The eight surface panels of the control volume are denoted by $f = 1, 2, ..., 8$. For panel f, if is the integration point lying at the centre of the panel, A_f is its surface area, and $\vec{n}_f$ is the unit outward normal. For nodes adjacent to the boundary, such as P' in Fig. 1C, the volume extends right to the physical boundary, and neighbouring nodes lie on the boundary. For two-dimensional problems, the volume is assumed to have unit depth normal to the plane of Fig. 1. Except for minor details related to the volume adjacent to the surface, the grid system just described was proposed by Baliga and ? [13] and used to make fluid flow computations by Schneider and Raw [14].

ANGULAR DISCRETIZATION

Directional dependence of radiant intensity at every spatial node is captured by subdividing direction into discrete, non-overlapping, solid angles of size ω^l. Total flexibility is allowed in choosing the individual size of ω^l provided $\sum \omega^l = 4\pi$. In practice ω^l is defined by a range of polar angle θ and of azimuthal angle ϕ.

FINITE VOLUME APPROXIMATION

Implementing the FVM, the RTE (Eq. 1) is integrated over control volume V_P and solid angle ω^l to yield the conservation constraint that the net radiant energy leaving through the surface of V_P within ω^l equals the net generation of radiant energy within V_P and ω^l by emission, absorption and scattering. Approximating this generation term by nodal point values, the conservation balance becomes

$$\sum_{f=1}^{8} Q_f^l = \left[-(K_{a,P} + \sigma_{s,P}) I_P^l + K_{a,P} I_{b,P} + \sigma_{s,P} \bar{I}_P^l\right] \omega^l V_P \tag{3}$$

where Q_f^l is the radiant energy within ω^l that crosses the surface panel f, I_P^l is the intensity within ω^l at node P, while $I_{b,P}$ and $\bar{I}_P^l$ are respectively the nodal blackbody intensity and the inscattering term. Defining I_{if}^l as the intensity at integration point if within ω^l

$$Q_f^l \approx I_{if}^l A_f \int_{\omega^l} (\vec{s} \cdot \vec{n}_f) d\omega = I_{if}^l A_f D_f^l \tag{4}$$

where $\vec{s}$ is a unit vector in the direction of radiation and the integral D_f^l is evaluated analytically. Using a Taylor series expansion about integration point if, Raithby and Chui [9] introduced the closure relation

$$I_{if}^l = I_{uf}^l e^{-\kappa_{if} S} + R_{if}^l \left(1 - e^{-\kappa_{if} S}\right) - \frac{1}{\kappa_{if}} \left(\frac{\partial R^l}{\partial s}\right)_{if} \left[1 - e^{-\kappa_{if} S}(1 + \kappa_{if} S)\right] \tag{5}$$

where I_{uf}^l is the intensity at point uf (see Fig. 1B) that lies distance S upstream from point if. $\kappa = K_a + \sigma_s$ is the extinction coefficient and variable R^l, defined in Eq. (6), embodies the emitting and scattering characteristics of the medium. The first term on the right side of Eq. (5) represents the remnant of intensity I_{uf}^l reaching if, while the last two terms incorporate the net gain of intensity due to emission and

inscattering from uf to if. The last two terms are crucial for the FVM to capture the optically thick limit.

The introduction of Eq. (5) generates three new unknowns: R^l_{if}, $\left(\frac{\partial R^l}{\partial s}\right)_{if}$ and I^l_{uf}. These must be related to nodal values before Eq. (3) can be solved. Attention is next turned to this matter.

Calculation of R^l_{if} and $\left(\frac{\partial R^l}{\partial s}\right)_{if}$

The variable R^l, is defined as

$$R^l = \frac{K_a I_b + \sigma_s \bar{I}^l}{\kappa} \tag{6}$$

where $I_b = (\sigma T^4)/\pi)$ is the blackbody intensity and $\bar{I}^l$ is the inscattering term evaluated by integrating Eq. (2) over ω^l, i.e.

$$\bar{I}^l = \frac{1}{4\pi} \sum_{l'}^{4\pi} I^{l'} \bar{\Phi} \tag{7}$$

where

$$\bar{\Phi} = \frac{\int_{\omega^l} \int_{\omega^{l'}} \Phi(l', l) d\omega^{l'} d\omega^l}{\omega^l} \tag{8}$$

The value of $\bar{\Phi}$ is obtained by exact or very accurate numerical integration of phase function Φ. This formulation was discussed and tested by Chui et. al. [10].

Since R^l is specified at nodal locations (like nodes 1 to 4 in Fig. 2), R^l_{if} at integration points can be obtained by bi-linear interpolation of nodal values; using the β, γ coordinate system shown in Fig. 2,

$$R^l_{if} = R^l_1 \frac{(1-\beta_{if})(1-\gamma_{if})}{4} + R^l_2 \frac{(1+\beta_{if})(1-\gamma_{if})}{4} +$$
$$R^l_3 \frac{(1+\beta_{if})(1+\gamma_{if})}{4} + R^l_4 \frac{(1-\beta_{if})(1+\gamma_{if})}{4}$$

or

$$R^l_{if} = \sum_{i=1}^{4} R^l_i w_i(\beta_{if}, \gamma_{if}) \tag{9}$$

where w_i is the bi-linear interpolation weight on node i for the integration point if specified by the local coordinates $(\beta_{if}, \gamma_{if})$.

Differentiating Eq. (9) with respect to distance in direction $\vec{s}$ yields

$$\left(\frac{\partial R^l}{\partial s}\right)_{if} = \sum_{i=1}^{4} R_i^l \left(\frac{\partial w_i}{\partial x}\frac{\partial x}{\partial s} + \frac{\partial w_i}{\partial y}\frac{\partial y}{\partial s}\right)_{x_{if},y_{if}} \tag{10}$$

where $\frac{\partial x}{\partial s}$ and $\frac{\partial y}{\partial s}$ are direction cosines in direction $\vec{s}$ in the global x, y coordinate system.

For a given grid, w_i, $\frac{\partial w_i}{\partial x}$ and $\frac{\partial w_i}{\partial y}$ are calculated analytically once and stored. Eqs. (9) and (10) are then used to determine R^l_{if}, $\left(\frac{\partial R^l}{\partial s}\right)_{if}$ at all integration points. when needed

Calculation of I^l_{uf}

I^l_{uf} is the intensity at point uf upstream of integration point if. For example points $u1$ and $u2$ associated with integration points $if = i1$ and $i2$ respectively are shown in Fig. 2A. To find uf, the ray in the centre of ω^l at point if is traced backwards until it intersects with the surface of the element. I^l_{uf} can then be obtained by linear interpolation (eg. I^l_{u1} can be obtained in terms of I^l_1 and I^l_4 in Fig. 2A). This practice leads to an equation for I^l_P that involves nodes downstream from node P; this complicates the solution of the equation, may lead to "wiggles" in the intensity, and reflects a physically incorrect influence. By slightly sacrificing accuracy, this downstream dependence can be avoided. For example, for quadrant $Q1$ in Fig. 2A and for the l-direction shown, the following approximation is used: $I^l_{u1} = I^l_{u2} = I^l_1$. For $Q2$ in Fig. 2B, I^l_{u2} would be linearly interpolated from I^l_1 and I^l_2, as would I^l_{u4} from I^l_1 and I^l_4.

Algebraic Equation for I^l_P

With R^l_{if}, $\left(\frac{\partial R^l}{\partial s}\right)_{if}$ and I^l_{uf} defined, Eqs. (4) and (5) can be substituted into (3) to obtain an algebraic equation relating I^l_P to the intensities at neighbouring nodes:

$$a^l_P I^l_P = \sum_{nb} a^l_{nb} I^l_{nb} + b^l_P \tag{11}$$

where the summation of nb is over the 'upstream' neighbours. For the l-direction shown in Fig. 1B, Eq. (11) takes the form

$$a^l_P I^l_P = a^l_W I^l_W + a^l_S I^l_S + a^l_{SW} I^l_{SW} + b^l_P \tag{12}$$

Equation (11) for each node together with boundary conditions provide the equation set for the nodal intensities in direction l. Similar equations are formed for other directions; the nodes that lie upstream of course change with l.

SOLUTION PROCEDURE

Overview

Provided scattering is not present, I_P^l in Eq. (11) is independent of downstream intensities. If the solver visits the nodes in the correct order, all terms on the right side of the equation will be known so I_P^l at each node can be found by direct substitution. This allows the solution to be obtained by moving from node to node in the optimal 'marching order'. For a Cartesian mesh it is immediately clear what the marching order must be, but for the irregular grid in Fig. 1A the order is no longer obvious.

To find a solution on irregular grids, there are two options. The equations could be solved by repeatedly sweeping across the grid until convergence is achieved, without regard to the optimal order. Alternatively a 'marching-order map' could be created which gives the optimal order in which the nodes should be visited. Once the angular discretization is fixed, a marching-order map can be constructed for each intensity direction, and this map can be stored for repeated use. Because the map is easy to generate, because it only needs to be revised when the spatial grid or angular discretization is changed, and because it reduces solution costs, the creation of the map is the preferred alternative.

To obtain a preview of how a marching-order map might appear, the reader is referred to Fig. 4B. For the U-shaped region, the optimal order, in which the nodes should be visited to solve for the intensity in the particular direction $\vec{s}$, is V1, V2, ..., V15.

To create the map, the boundary elements are swept first to find the starting location. Once this is found, the entire marching sequence is derived by repeated application of a simple algorithm. Details are now provided.

Marching-Order Within an Element

The element shown in Fig. 2 contains four quadrants. The quadrant Q1 is part of the control volume for node 1, that requires the intensities I_{i1}^l and I_{i2}^l, which in turn require I_{u1}^l and I_{u2}^l. These and values of I_{u3}^l and I_{u4}^l are similarly required for the

other control volumes associated with quadrants Q2, Q3 and Q4. According to the discretization scheme already described, $I^l_{u1} = I^l_{u2} = I^l_1$, so the equation for I^l_1 is independent of I^l_4, I^l_2 and I^l_3. Clearly node 1 is furthest "upstream".

Similarly the equation for I^l_4 depends on I^l_1 but not on I^l_2 or I^l_3, and I^l_2 depends on I^l_1 but not on I^l_4 or I^l_3. Therefore, nodes 2 or 4 are equally upstream, but not so far as node 1. Node 3 is least upstream.

The order in which the nodes in Fig. 2 should be visited are therefore 1-2or4-3, where 2or4 means the order may be 2-4 or 4-2. For a different direction $\vec{s}$, the order may be different.

The general algorithm for node ordering within an element is shown in Fig. 3. Four sectors, denoted by φ_1 to φ_4, are defined by the quadrant boundaries. Once the sector, in which the intensity direction $\vec{s}$ falls, is determined, the table in Fig. 3 specifies the marching order. The special cases that arise for boundary elements are also shown. The stars denote locations where the intensity is known from boundary conditions.

Generation of the Marching-Order Map

The elements that make up the grid for a U-shaped region are shown in Fig. 4A. The node numbering is converted from the local numbering in Fig. 2 to a global numbering in Fig. 4 that uses (i, j), where i numbers the node along one set of grid lines and j along the other.

To find the starting location, the boundary elements are visited in any order until an interior node is found for which the only nodes further upstream are boundary nodes that have known intensities from boundary conditions (eg. in Fig. 4A, the intensities at nodes (1,1), (2,1), (3,1), etc are known from boundary conditions). Applying the element algorithm in Fig. 3 to element $e1$ in Fig. 4A shows that node (3,2) is furthest upstream among the unknown intensities in that element. But from element $e2$, node (2,2) is further upstream than (3,2), and from $e3$, there is no unknown intensity that lies still further upstream. The node (2,2) is therefore a suitable starting location. This is denoted in Fig. 4B as V1.

With the furthest upstream node known, the map is generated by systematically finding which nodes are next furthest upstream. Applying the element algorithm to the elements that share the starting node (2,2) shows that either (2,3) or (3,2) are next. These are therefore denoted by V2 and V3 in Fig. 4B. Repeated application of the algorithm to the elements that share these nodes reveals V4 and V5 in Fig. 4 are

next, and so on until all interior nodes are numbered.

In special cases, where the grid is strongly kinked, the algorithm yields a conflict. To illustrate this conflict, the node (4,2) in Fig. 4A is shown enlarged in Fig. 5, where the neighbouring elements are labelled $e1$ to $e4$. For $e1$, the marching order is (3,2)-(3,3)or(4,2)-(4,3) while for $e2$, it is (4,3)-(4,2)or(5,3)-(5,2). The order (4,2)-(4,3) for $e1$ is in conflict with (4,3)-(4,2) for $e2$. The conflict can be addressed by simultaneously solving the equations for all nodes that are in conflict. Alternativelly an order can be arbitrarily chosen, accepting the consequence that the marched solution will not be exactly correct from this point downstream. In practice, few conflicts arise, and iterations from the conflict point downstream yield rapid convergence.

BOUNDARY CONDITIONS

In this analysis, all boundaries are assumed diffuse-gray and the boundary nodes (see Fig. 1C) are representative only of the bounding surface. For a surface at temperature T_B, the boundary condition for radiant intensity going into the medium at the surface nodes can be conveniently set as

$$I_B = \left[(1 - \epsilon_B) \sum_{l_{in}} Q_B^{l_{in}} + \epsilon_B A_B \sigma T_B^4 \right] \frac{1}{\pi A_B} \tag{13}$$

The first term on the right side of Eq. (13) represents the reflected component where the summation of radiant flux Q (defined in Eq. (4)) is over all incoming l_{in} directions. The second term refers to the emissive component, which is proportional to the emissive power, σT_g^4, surface emissivity, ϵ_B, and area, A_B.

Special Considerations at the Boundary

For simple geometries, it is possible to subdivide directions such that the edge of a discrete solid angle (or "bundle") always lies tangent to the boundary. For complex geometries, the situation shown in Fig. 6 cannot be avoided; some rays in a bundle impinge on the surface from above (the "incoming" rays), while other rays in the same bundle originate from the surface (the "outgoing" rays). The incoming intensity will usually be very different from the outgoing intensity and the approximation used in the model, that the intensity is uniform over each bundle, is unacceptable. New approximations are introduced for the bundles on the boundary where this situation is encountered.

The intensity associated with a discrete solid angle is assumed to be at the centre of its bundle. For the case shown in Fig. 6A, therefore, the intensity over the incoming portion of the bundle is approximated by I^m; the intensity over the outgoing portion is approximated by I^{m+1}, the value of its immediate neighbour. For the bundle in Fig. 6B that straddles the boundary, the outgoing intensity is calculated from the boundary condition, while the incoming intensity is approximated by its immediate neighbour I^{m-1}. For the situation where I^m lies exactly along the surface, its value is not calculated at all, and both the incoming and outgoing intensities are approximated by their respective neighbour values.

These new approximations introduce new couplings between intensities of different directions at the bounding surface, but they can be readily ~~corrected~~ solved by iteration.

TEST RESULTS

The FVM just described is applicable to many 2D radiation problems in very complex geometries. To convincingly demonstrate the method, however, it seems best to restrict attention to benchmark problems, and to problems where expected features of the solution can be checked.

Preliminary Tests

The non-orthogonal method was applied to calculate the radiant exchange in a square cavity with the temperature-specified walls, and with an absorbing and isotropically scattering medium. The solution was compared to the earlier solution using a Cartesian code (Raithby and Chui [9]), and the results were found to be virtually the same. The increased generality of the non-orthogonal code increased the CPU time by a factor of 4.5 relative to the Cartesian code.

Infinite Concentric Cylinders

The second case is the prediction of radiative heat transfer in a long cylindrical annulus (see Fig. 7) containing a homogeneous, absorbing-emitting medium. The inner and outer radii of the annulus are 0.5 $[m]$ and 1.0 $[m]$ respectively. The cylinder walls are assumed black and cold ($T_w = 0$), and the enclosed medium is held at a constant temperature of $T_g = 100K$. The objective is to determine the heat flux in the radial direction.

A benchmark solution to the problem has been obtained by Dua and Cheng [15]. The dimensionless radial heat flux, q_r^*, is plotted in Fig. 7A for three different absorption coefficients: $K_a = 0.1, 1.0$ and 5.0 $[1/m]$. Errors of up to $\pm 5\%$ in these "exact" results are expected because they were obtained by digitizing published plots. Negative q_r^* indicates that the net radiative heat transfer is in the negative radial direction, towards the inner cylinder. Larger values of K_a result in larger q_r^* because emission is higher.

The elements that make up a coarse spatial grid are shown in Fig. 7B. The nodes are evenly spaced in the azimuthal direction and radial directions, except adjacent to the boundaries where the spacing is halved. As the azimuthal grid is refined, the polygon more closely approaches a circle.

One component of intensity was computed on the grid (see Fig. 7B) using the present non-orthogonal FVM; by the mapping procedure of Chui et al [10], the spatial distribution of this component provides the complete axisymmetric intensity distribution. The resulting q_r^* values computed on the coarse grid shown in Fig. 7B ($N_x = 7, N_y = 4, N_\theta = 2$, where θ is the polar angle) are plotted in Fig. 7A.

The maximum discrepancy with the "exact" results was 15%, for the $K_a = 1.0$ case. As the grid was refined, the errors in the computed solution rapidly diminished. ~~to within the digitizing error~~. To obtain these solutions, iterations were required to account for the special considerations at the boundary stated earlier. The convergence criterion was that the q_r^* values should change less than 0.01% between iterations.

To obtain convergence on the coarse (7x4x2) mesh, 8[s] of CPU time on a VAX 11-785 were needed. For the finest grid (25x16x4) used in this problem, 110 [s] were required. Preprocessing activity, including the calculation of geometric quantities and the marching-order map, took an additional 5 to 11 [s].

Non-Rectangular Enclosure

The last benchmark problem is to compute the net radiant flux, q_n, that falls on the north boundary of the non-rectangular enclosure shown in Fig. 8. The wall temperature was set to zero, and the medium temperature was set at $T_g = 100K$. The medium was assumed to be non-scattering, and solutions were sought for absorption coefficients of $K_a = 0.1, 1.0$ and 10.0 $[1/m]$.

The exact solution to the Radiative Transfer Equation at point (x, y) is

$$I(x, y, \theta, \phi) = I_b(1 - e^{-K_a S}) \tag{14}$$

where S is the distance from the point upstream to the enclosure wall along the ray defined by (θ, ϕ), and $I_b = \sigma T_g^4/\pi$. By computing the incident radiant intensities on the north wall of the enclosure, the "exact" local heat fluxes plotted in Fig. 8 were obtained. For $K_a = 10.0$, $q_n^* \rightarrow 1.0$ along most of the wall, indicating that the transmission of radiation from the other enclosure walls has little effect except near the corners. Weak emission by the medium ($K_a = 0.1$) results in much lower heat transfer.

A non-orthogonal computational mesh was generated by locating an equal number of nodes on each boundary, uniformly spaced on each surface. The grid lines were generated by joining corresponding nodes on opposite sides of the enclosure by straight lines. The results from a $(N_x \times N_y) \times (N_\theta \times N_\phi) = (16 \times 16) \times (4 \times 16)$ grid are also plotted in Fig. 8; the maximum error was less than 1%. Results for other grids for $K_a = 0.1$ indicate that a fine discretization in the azimuthal direction (high N_ϕ) is needed to predict q_n^*, which is reasonable because the intensity distribution is non-uniform in this direction. For $K_a = 10.0$, good accuracy is obtained with a coarse directional mesh because the radiation falling on the surface has nearly uniform intensity; in this case, spatial refinement is of greater importance.

The numerical results in Fig. 8 required 200 CPU [s] on a VAX 11-785 for the finest grid, and an additional 30 [s] of pre- processing time. The coarse grid solution required about 24 [s]. Similar times were needed for non-zero wall temperatures, as reported in detail by Chui [16].

J-Shaped Enclosure

This test applies the FVM to a J-shaped domain (see Fig. 9), containing an absorbing, emitting, and anisotropically scattering medium. A uniform, diffuse radiant flux was prescribed on the west wall, while the other walls were black and cold ($T_w = 0K$). Radiative equilibrium was assumed. The absorption coefficient was $K_a = 0.01$, and the scattering coefficient was taken as $\sigma_s = 1$ except in the base case where $\sigma_s = 0$ was used. The scattering phase function was approximated by the delta-Eddington approximation (Joseph and Wiscombe [17]),

$$\Phi(\psi) = 2f\delta(1 - cos\psi) + (1 - f)(1 + 3gcos\psi) \qquad (15)$$

where ψ is the scattering angle. The f parameter governs the amount of forward scattering, while g is the asymmetry factor. The objective of this test is to predict

the net radiant flux to the north and the south walls, defined in Fig. 9B.

Since an exact benchmark solution is not available for this problem, physical arguments will be used to check the reasonableness of the predictions. A relatively coarse grid (N_x x N_y) x (N_θ x N_ϕ) = (11 x 4) x (2 x 8), is selected for this problem (see Fig. 9B). The net non-dimensional radiant flux distribution along the south wall of the channel, $q_s^* = q_s/q_{in}$, is plotted in Fig. 9A for four different scattering conditions. The base case, shown as squares in Fig. 9A, has no scattering at all ($\sigma_s = 0$).

Generally, q_s^* decreases with X_s because radiation is attenuated by absorption and scattering. When scattering is absent, the radiant flux impinging on the wall is very sensitive to its orientation with respect to the source. Thus, q_s^* of the base case (shown as squares) increases from point A on as the south wall lies in a more direct line of sight from the source. This increase levels off when it is balanced by the loss due to absorption. Beyond point C, q_s^* drops because the south wall becomes increasingly sheltered from the source, and at point D, the source is completely hidden and q_s^* is correctly predicted to approach zero.

The presence of scattering makes the dependence on wall orientation to the source less crucial. This is especially the case when scattering is isotropic. As a result, q_s^* in this case (shown as filled-in circles in Fig. 9A) diminishes monotonically from $X_s = 0$ to point D without any sudden increase at point A.

However, when scattering is strongly forward ($f \rightarrow 1$), the q_s^* distribution (plotted as '+' in Fig. 9A) closely resembles the base case. This result is intuitively correct because if inscattering and outscattering can only occur in the forward direction, they exactly cancel each other.

For the case with $f = 0.6, g = 0.2$ (shown as triangles in Fig. 9A), scattering occurs with a moderate preference in the forward direction. The q_s^* distribution is expected to lie between the case with almost total forward scattering ($f = 0.999$) and the isotropic scattering case. This expectation is also confirmed in Fig. 9A.

Similar observations can be made regarding the net dimensionless radiant flux distributions along the north wall, $q_n^* = q_n/q_{in}$ (not shown here, see Chui [16]).The prediction correctly shows that q_n^* in the non-scattering case approaches zero beyond point F because the north wall is not directly visible to the source. But when scattering is admitted, the prediction indicates that q_n^* beyond F is non-zero, which is reasonable because scattering spreads some of the radiation to regions beyond point F.

The above test problem requires an iterative process to obtain a converged solu-

tion. Typically, 12 cycles of updates are needed to attain a radiant flux value that varies less than 0.01% between cycles. The CPU expense is about 60[s] in a VAX 11-785 machine.

SUMMARY

The present paper shows how the Finite Volume Method can be applied on a mesh that consists of non-orthogonal quadrilateral elements. This application encountered only minor obstacles. One obstacle was that, in a general geometry, the boundaries of the discrete solid angles can no longer be chosen to fall along physical boundaries. A simple solution to this problem was proposed. The other obstacle was that, although the equations can still be solved most efficiently by sweeping from node to node in a specified order, this order is not obvious for a non-orthogonal mesh. The solution was to develop an algorithm that generates, as part of pre-processing activities, a map of the optimal order.

The method was then applied to three benchmark problems, and one more complex problem where the main check was intuitively correct behaviour. Rapid and accurate predictions were found to the benchmark problems, and entirely reasonable behaviour was found for the complex problem. It seems that the Finite Volume Method can now be confidently applied on the same grids that are used to simulate other processes.

ACKNOWLEGMENTS

This work was supported by a contract from the Combustion and Carbonization Research Laboratory, CANMET, of the Energy Mines and Resources Department of the Canadian Federal Government, under the scientific authority of Mr. P. Hughes. The authors are also grateful for the additional financial assistance received from the Natural Science and Engineering Research Council of Canada.

REFERENCES

1. J. R. Howell, Thermal Radiation in Participating Media: The Past, the Present, and Some Possible Futures, *ASME Journal of Heat Transfer*, vol. 110, pp. 1220 -1226, 1988.

2. R. Viskanta and M. P. Mengüç, Radiation Heat Transfer in Combustion Systems, *Progress in Energy and Combustion Science*, vol. 13, no. 2, pp. 97-160, 1987.

3. M. P. Mengüç and R. Viskanta, Radiative Transfer in Three- Dimensional Rectangular Enclosures containing Inhomogeneous, Anisotropically Scattering Media,*J. Quant. Spectrosc. Radiat. Transfer*, vol. 33, no. 6, pp. 533-549, 1985.

4. M. P. Mengüç and R. Viskanta, Radiative Transfer in Axisymmetric, Finite Cylindrical Enclosures, *ASME Journal of Heat Transfer*, vol. 108, pp. 271-276, 1986.

5. W. A. Fiveland, Three-Dimensional Radiative Heat Transfer Solutions by the Discrete-Ordinates Method, *AIAA J. Thermophysics*, vol. 2, no. 4, pp. 309 - 316, 1988.

6. M. E. Larsen and J. R. Howell, The Exchange Factor Method: An Alternative Basis for Zonal Analysis of Radiating Enclosures, *ASME Journal of Heat Transfer*, vol. 107, pp. 936-942, 1985.

7. R. G. Siddall and N. Selçuk, Evaluation of a New Six-Flux Model for Radiative Transfer in Rectangular Enclosures, *Trans. Inst. Chem. Engrs.*, vol. 57, pp. 163-168, 1979.

8. F. C. Lockwood and N. G. Shah, A New Radiation Solution Method for Incorporation in General Combustion Prediction Procedures, *18th Symp. (Int.) on Combustion*, The Combustion Institute, pp. 1405-1414, 1981.

9. G. D. Raithby and E. H. Chui, A Finite-Volume Method for Predicting Radiant Heat Transfer in Enclosures with Participating Media, *ASME Journal of Heat Transfer*, vol. 112, pp. 415-423, 1990.

10. E. H. Chui, G. D. Raithby and P. M. J. Hughes, Prediction of Radiative Transfer in Cylindrical Enclosures by the Finite Volume Method, *AIAA J. Thermophysics*, (in press), 1991.

11. E. H. Chui and G. D. Raithby, An improved Solution Scheme to improve Convergence Rate in Radiative Transfer Problems, submitted to *Numerical Heat Transfer*, 1991.

12. R. Siegel and J. R. Howell, *Thermal Radiation Heat Transfer*, 2nd. ed., McGraw Hill, New York, London, p. 453, 1981.

13. B. R. Baliga and ??

14. G. E. Schneider and M. J. Raw, Control Volume Finite-Element Method for Heat Transfer and Fluid Flow using Colocated Variables. 1. Computational Procedure, *Numerical Heat Transfer*, vol. 11, pp. 363-390, 1987.

15. S. S. Dua and P. Cheng, Multi-Dimensional Radiative Transfer in Non-isothermal Cylindrical Media with Non-isothermal Bounding Walls, *Int. J. Heat Mass Transfer*, vol. 18, pp. 245 - 259, 1975.

16. E. H. Chui, Modelling of Radiative Heat Transfer in Participating Media by the Finite Volume Method, Ph.D. thesis, Department of Mechanical Engineering, University of Waterloo, Waterloo, Ontario, Canada, 1990.

17. J. H. Joseph and W. J. Wiscombe, The Delta-Eddington Approximation for Radiative Heat Transfer, *Journal of Atmospheric Sciences*, vol. 33, pp. 2452 - 2459, 1976.

Figure 1: (A) Sample computational mesh, (B) an interior control volume formed from assembly of four quadrants, and (C) a control volume adjacent to the boundary.

Figure 2: Determination of integration point intensities on edges of quadrants Q1 to Q4.

Figure 3: Variation of marching or r with the sector φ in which a given intensity direction $\vec{s}$ lies. Superscript * denotes boundary intensities that are known.

Figure 4: (A) Determination of the starting location for a U-shaped domain in direction $\vec{s}$, and (B) the map for the optimal marching-order for the solver: V1, V2,..., V15.

Figure 5: Elements surrounding node (4,2) in Fig.4, where the marching-order algorithm encounters a conflict due to sharp grid turning.

Figure 6: Cases in which one discrete solid angle, or bundle, contains both incoming and outgoing radiation.

Figure 7: (A) 'Exact' results (see text) for the dimensionless radial heat flux and predictions on the coarse grid. (B) A coarse grid for a concentric annulus.

Figure 8: Nondimensional radiant heat transfer on the north wall of the non-rectangular enclosure with an emitting gas at constant temperature T_g for absorption coefficients of $K_a = 0.1,\ 1.0,\ 10.0\ [1/m]$.

Figure 9: (A) Nondimensional radiant heat transfer on the south wall of the J-shaped enclosure with a diffuse radiant flux q_{in} incident on the west wall for a medium with $K_a = 0.01\ [1/m]$ and various scattering conditions. f and g refer to non-isotropic scattering parameters (see Eq. (15)). Part (B) shows the control volumes defined by the spatial grid.

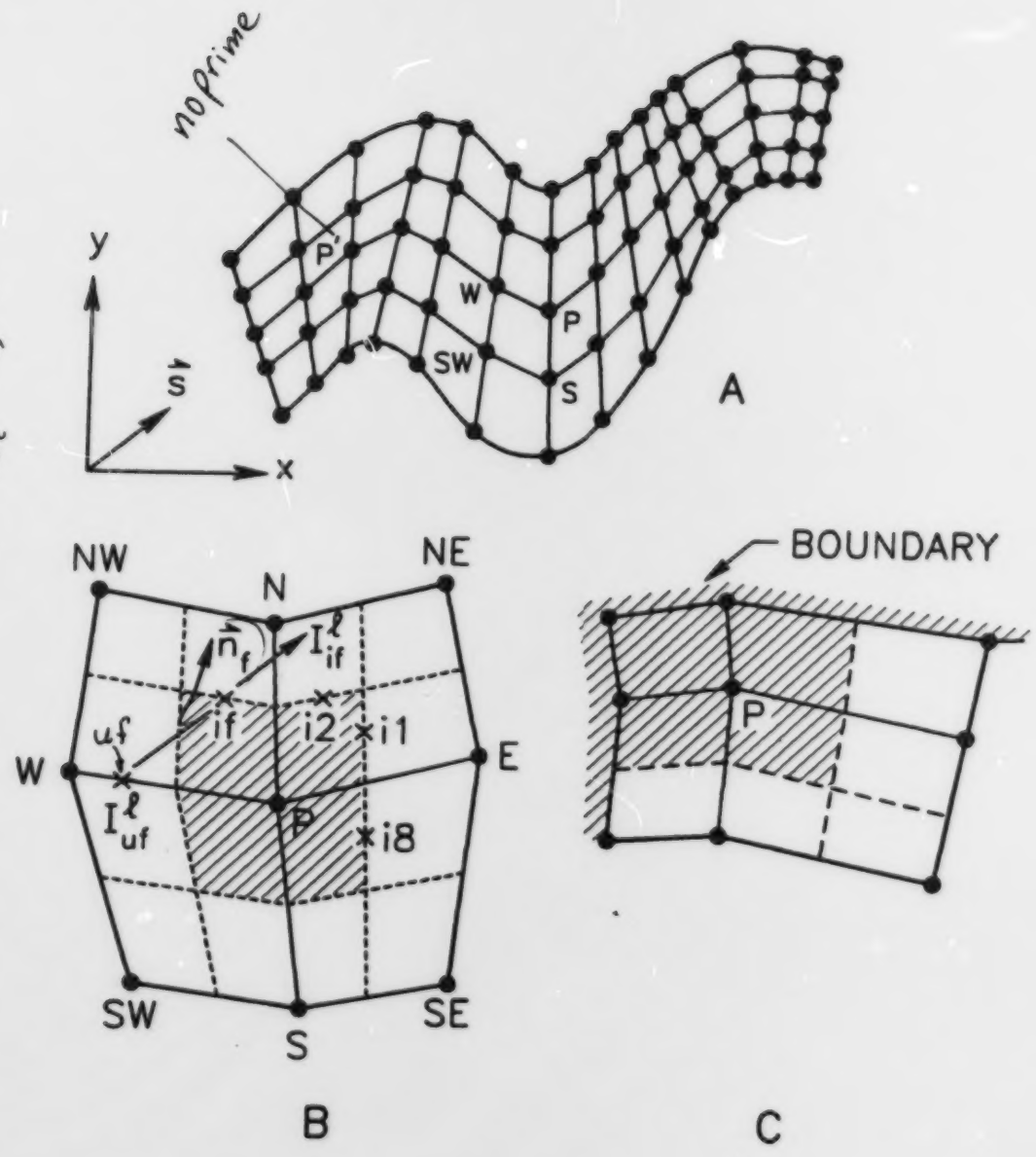

Figure 1: (A) Sample computational mesh, (B) an interior control volume formed from assembly of four quadrants, and (C) a control volume adjacent to the boundary.

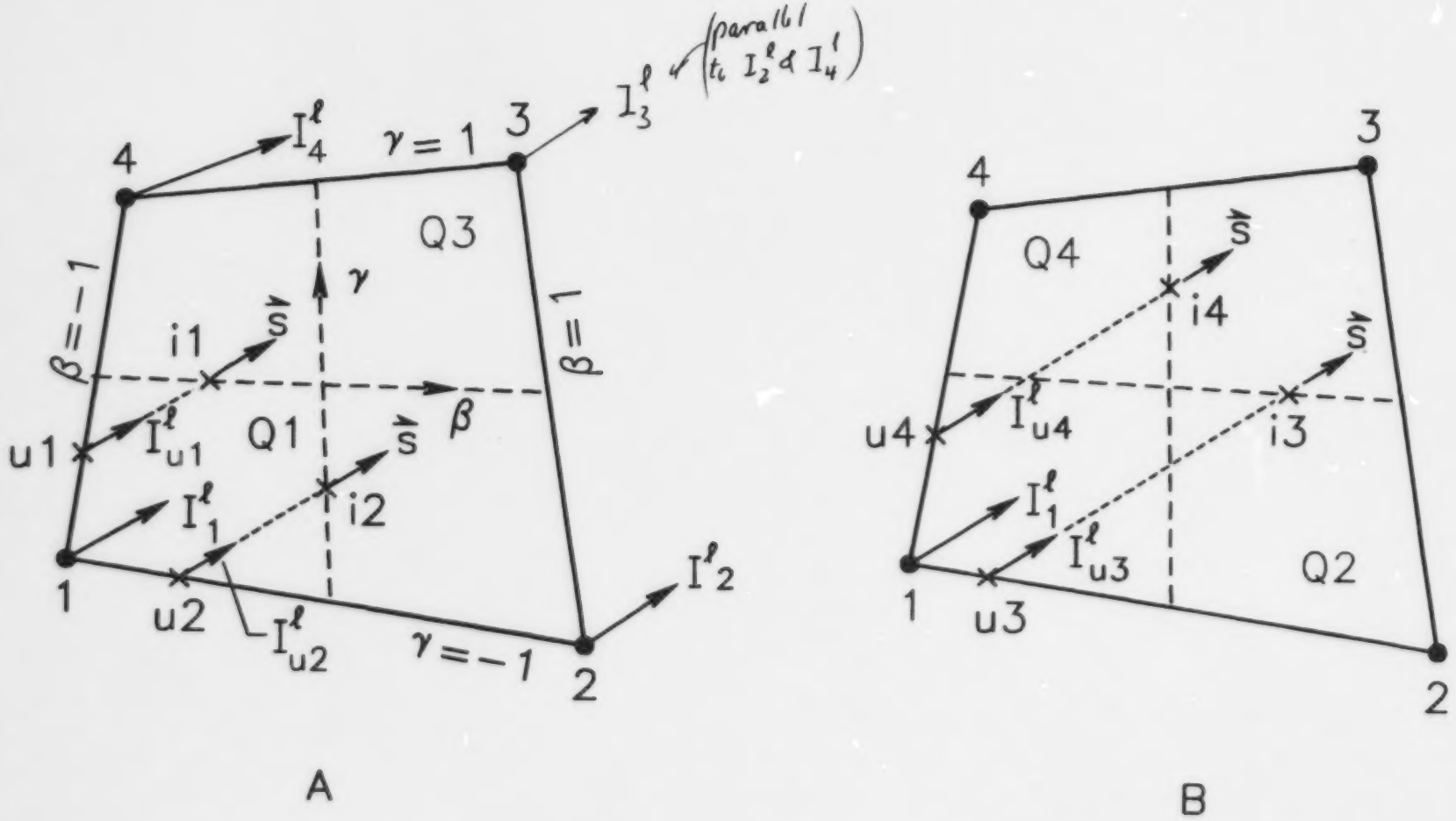

Figure 2: Determination of integration point intensities on edges of quadrants Q1 to Q4.

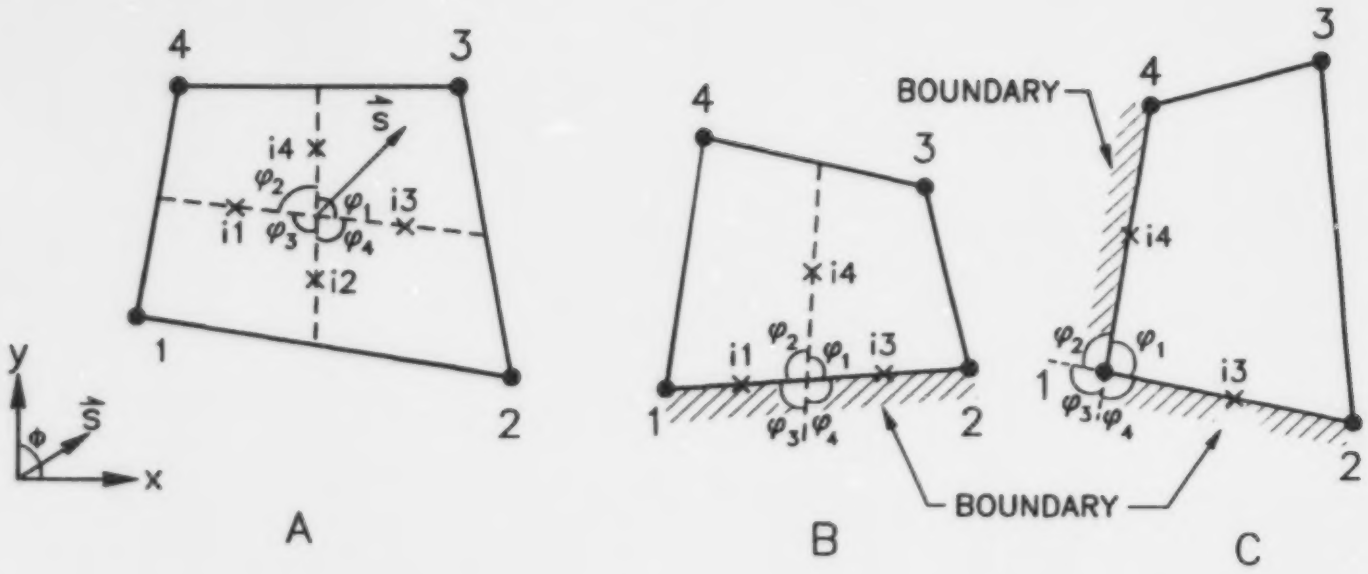

φ_1	1−2 OR 4−3	1*,2*−4−3	2*,4*−3
φ_2	2−1 OR 3−4	2*,1*−3−4	2*,1*−3−4
φ_3	3−2 OR 4−1	3−2−4−1	3−2 OR 4
φ_4	4−1 OR 3−2	4−1−3−2	4*,1*−3−2

Figure 3: Variation of marching order with the sector φ in which a given intensity direction $\vec{s}$ lies. Superscript * denotes boundary intensities that are known.

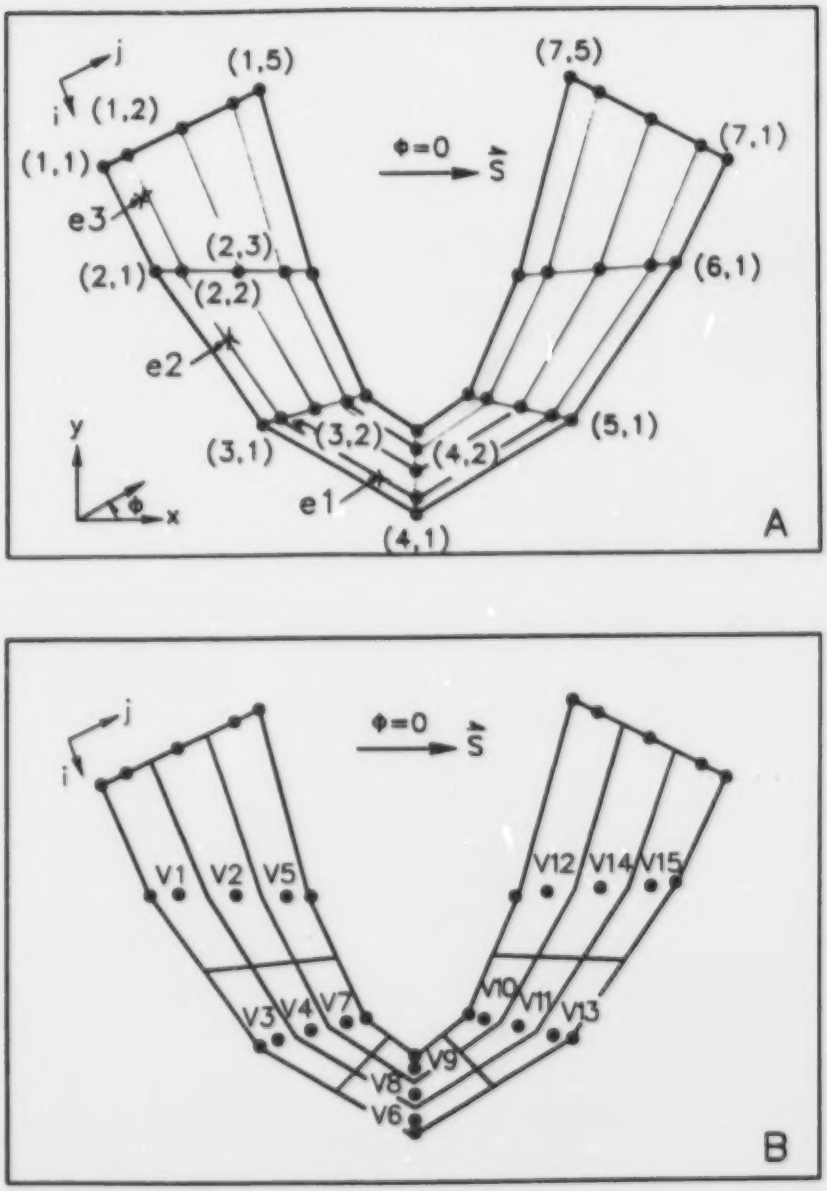

Figure 4: (A) Determination of the starting location for a U-shaped domain in direction $\vec{s}$, and (B) the map for the optimal marching-order for the solver: V1, V2,..., V15.

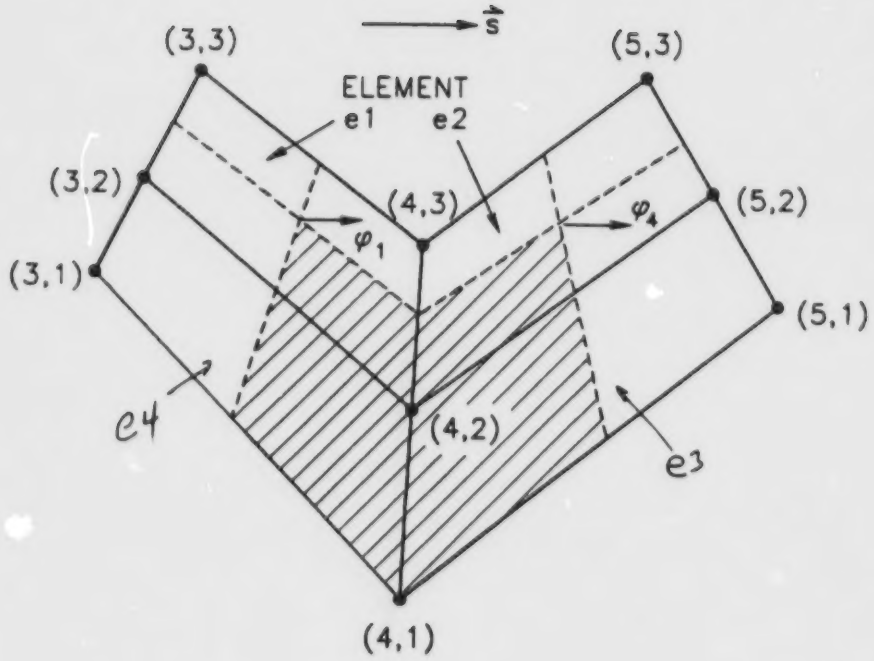

Figure 5: Elements surrounding node (4,2) in Fig.4, where the marching-order algorithm encounters a conflict due to sharp grid turning.

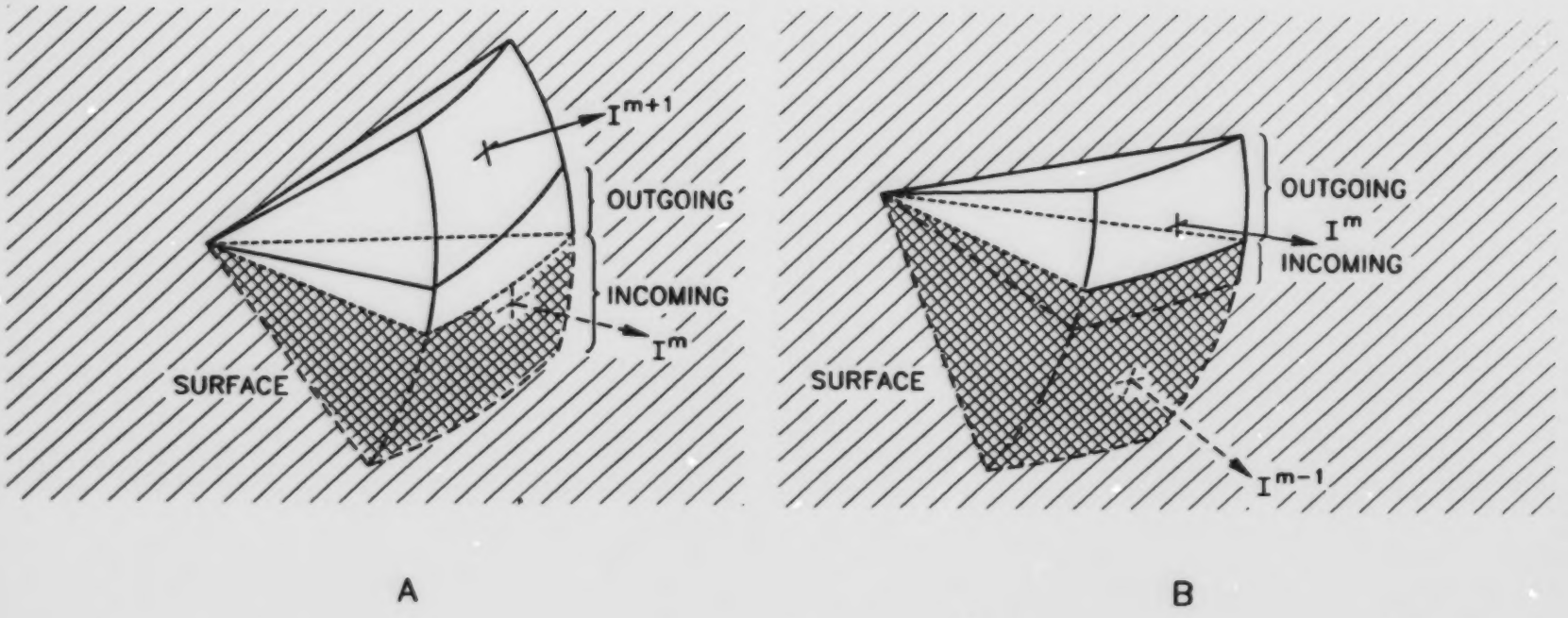

Figure 6: Cases in which one discrete solid angle, or bundle, contains both incoming and outgoing radiation.

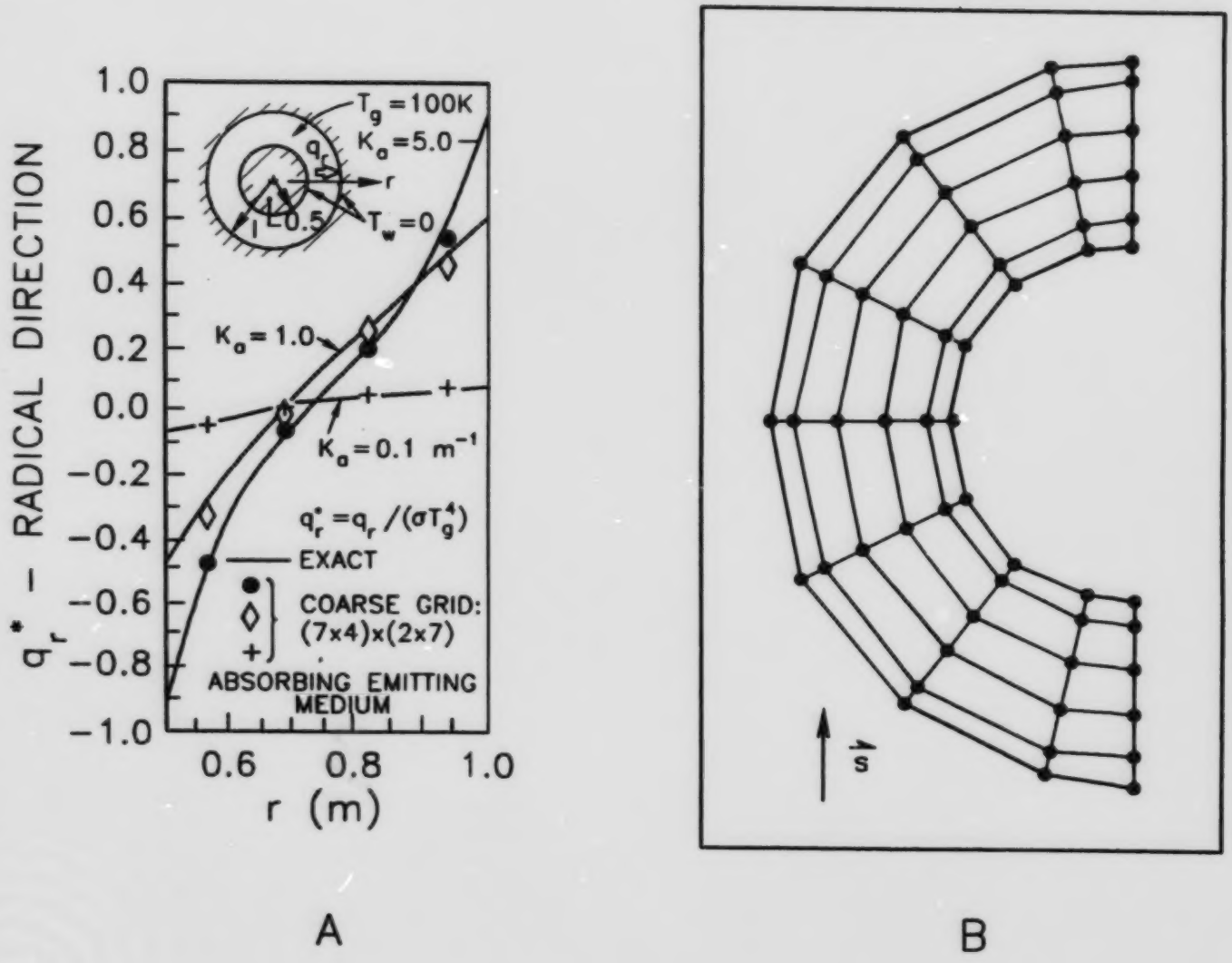

Figure 7: (A) 'Exact' results (see text) for the dimensionless radial heat flux and predictions on the coarse grid. (B) A coarse grid for a concentric annulus.

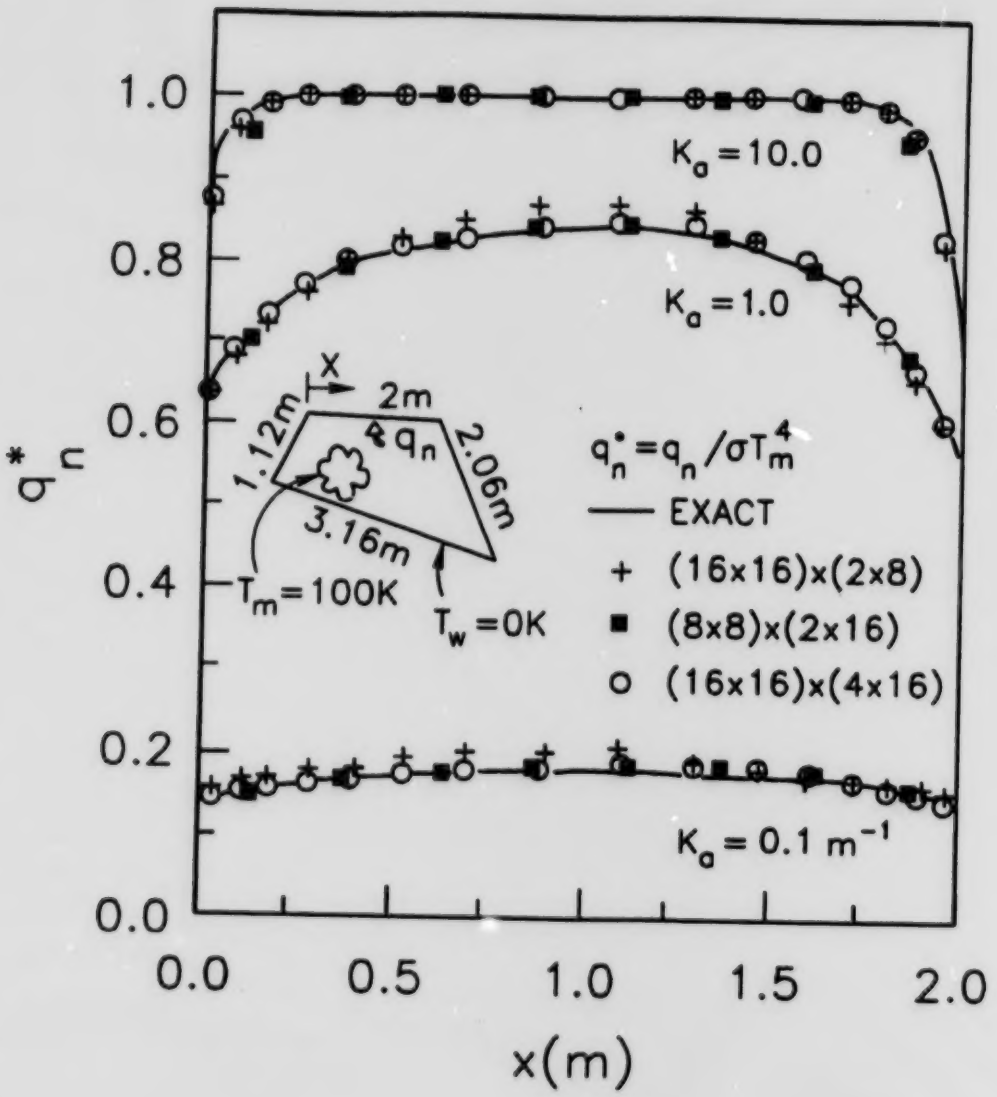

Figure 8: Nondimensional radiant heat transfer on the north wall of the non-rectangular enclosure with an emitting gas at constant temperature T_g for absorption coefficients of $K_a = 0.1,\ 1.0,\ 10.0\ [1/m]$.

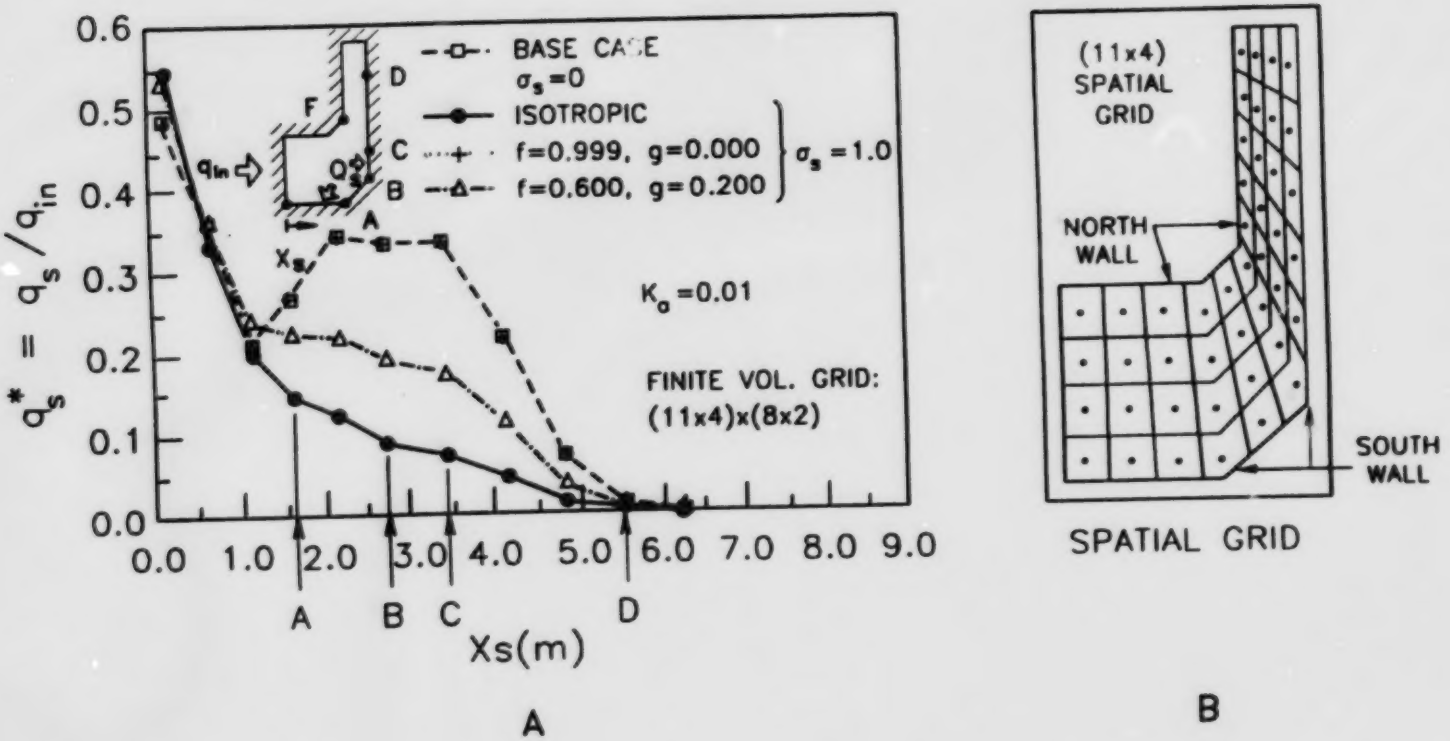

Figure 9: (A) Nondimensional radiant heat transfer on the south wall of the J-shaped enclosure with a diffuse radiant flux q_{in} incident on the west wall for a medium with $K_a = 0.01$ [$1/m$] and various scattering conditions. f and g refer to non-isotropic scattering parameters (see Eq. (15)). Part (B) shows the control volumes defined by the spatial grid.

sum of Q_f, $f = 1, 2, \ldots N_f$. The simplest approximation for Q_f is

$$Q_f = A_{s,f} \int_{\omega_f} I_f(\mathbf{s}\cdot\mathbf{n}_f)d\omega \tag{6}$$

where the intensity and unit normal to the surface have been approximated by their values at the integration point "f," located "centrally" on the panel.

The simplest Level 1 approximation of (3) is therefore

$$\sum_{f=1}^{N_f} Q_f = \sum_{f=1}^{N_f} A_{s,f} \int_{\omega_f} I_f(\mathbf{s}\cdot\mathbf{n}_f)d\omega$$

$$= [-(K_p + \sigma_p^s)I_p + K_p I_{b,p} + \sigma_p^s I_p] \nabla_p \omega^l \tag{7}$$

Discrete Equation, Level 2 Approximation. To close the set of equations, relations are needed between the panel integration-point values I_f and nodal point values I_P, I_E, etc. Since several different closure relations, all starting from equation (7), are possible, these are defined as the Level 2 approximations.

In the present study, I_f was found by tracing back along the path taken by the ray in reaching f (i.e., along the -s direction) until a location was reached at which the intensity can be reasonably found by interpolation between nodes. The location of the interpolation point will be specified later when the grids are generated. For now, it is sufficient to denote its location by uf as shown in Fig. 2 and the intensity (known by the interpolation) by I_{uf}. To estimate the value of I_f from I_{uf} for the given s direction, rewrite equation (1) as

$$\frac{dI}{ds} + \kappa I = \kappa R \tag{8A}$$

where

$$\kappa = K + \sigma^s \text{ and } R = (KI_b + \sigma^s \bar{I})/\kappa \tag{8B}$$

Let R be approximated by the first two terms of a Taylor series expansion about point f, and treat κ as constant at κ_f. Carrying out the integration of equation (8A) over distance S from uf to f, shown in Fig. 2(B), the intensity in direction s at integration point f is

$$I_f = I_{uf} e^{-\kappa_f S} + R_f(1 - e^{-\kappa_f S}) - \frac{(\partial R/\partial s)_f}{\kappa_f}(1 - e^{-\kappa_f S}(1 + \kappa_f S)) \tag{9}$$

$(\partial R/\partial s)_f$, the directional derivative in the s direction, is related to the gradient of R, ∇R, by

$$\left(\frac{\partial R}{\partial s}\right)_f = (\nabla R)_f \cdot \mathbf{s}$$

Introducing equation (9) into equation (6), and carrying out the integration over ω_f, gives the following estimate of the radiant heat transfer within ω^l that crosses surface panel f:

$$Q_f^l = A_{s,f} I_{uf}^l e^{-\kappa_f S} N_f^l + A_{s,f} R_f^l (1 - e^{-\kappa_f S}) N_f^l$$

$$- \frac{A_{s,f}}{\kappa_f}(1 - e^{-\kappa_f S}(1 + \kappa_f \bar{S})) \sum_{j=1}^{3} \left(\frac{\partial R^l}{\partial x_j}\right)_f D_{jf}^l \tag{10}$$

where R^l is the value of R for the bundle ω^l, where the gradient of R has been arbitrarily written in Cartesian coordinates x_j, defined by the unit vectors $\mathbf{e}_j$, as

$$\nabla R^l = \sum_{j=1}^{3} \left(\frac{\partial R^l}{\partial x_j}\right)\mathbf{e}_j$$

and where N_f^l and D_{jf}^l are integrals that depend only on the panel orientation for a given ω^l

$$N_f^l = \int_{\omega^l} (\mathbf{s}\cdot\mathbf{n}_f)d\omega \qquad D_{jf}^l = \int_{\omega^l} (\mathbf{e}_j\cdot\mathbf{s})(\mathbf{s}\cdot\mathbf{n}_f)d\omega \tag{11}$$

In the integration over ω^l in equation (6) that led to equation (10), I_{uf} was treated as constant, and S was held constant at $\bar{S}$. Their values are evaluated along the ray $\mathbf{s}^l$ that lies in the center of the solid angle ω^l. To include the effect of varying S and I_{uf} over ω^l would dramatically increase complexity. Furthermore, the practice of using constant values is consistent with the other approximations embodied in the discrete equation representation of the continuous equations.

Before continuing, it is of interest to demonstrate that the approximations of the heat flux given by equation (10) is reasonable. For concreteness, consider the case where the surface panel lies in a z plane, with surface normal $\mathbf{e}_3$. For the optically thin limit ($\kappa_f \to 0$), the radiant flux becomes

$$Q_f^l = A_{s,f} I_{uf}^l \int_{\omega^l} (\mathbf{s}\cdot\mathbf{e}_3)d\omega$$

The intensity in this limit is propagated correctly (i.e., without

Nomenclature (cont.)

s = distance along a beam in the s direction, m
$\mathbf{s}$ = unit vector in the direction for which I is to be calculated
$\mathbf{s}^l$ = unit vector in the center of discrete solid angle ω^l
S = distance from the interpolation point to the integration point (see Fig. 2(B))
$\bar{S}$ = average value of S over the solid angle ω^l
T = temperature, K
$\mathcal{V}$ = volume, m^3
x, y, z = Cartesian coordinates, m
x_1, x_2, x_3 = Cartesian coordinates; $x_1 = x$, $x_2 = y$, $x_3 = z$, m
x^* = $(\kappa + K)D$, used for one-dimensional problem
ϵ = surface emissivity
θ = polar angle, measured from the z axis
κ = extinction coefficient = $K + \sigma^s$, m^{-1}
ρ = surface reflectivity
σ = Stefan–Boltzmann constant = 5.729×10^{-8} W/m^{2}K^4
σ^s = scattering coefficient, m^{-1}
ϕ = azimuthal angle in the x-y plane, measured from x axis (Fig. 6)
Φ = phase function for scattering from direction $\mathbf{s}'$ to direction $\mathbf{s}$
ω = solid angle
ω^l = solid angle of the discrete bundle centered at $\mathbf{s}^l$

Subscripts

B = bottom surface
P, N, E, S, W = labels for nodes within control volumes
f = at the integration point f
uf = at the interpolation point (Fig. 2(A))
T = top surface
j = coordinate index = 1, 2, 3

Superscripts

l = in the solid angle ω^l
$*$ = nondimensional

4 The 'Explicit' Solution Procedure

If the medium temperature is known and scattering is ignored ($\sigma_s = 0$), the value of b_P^l in Eq. (9) is known at each node P. If the grid is swept in the direction of the intensity, the intensity terms on the right side of equations like (10) are all known, so values of I_P^l can be found by direct substitution. If the boundaries are black, the values of I_P^l so obtained represent the required discrete solution; if the boundaries are gray, iteration is required because the intensities leaving the surface (specified through the boundary condition) depend on all the intensities incident on the surface.

If the temperature is to be determined as part of the calculation, an energy equation must be solved. For the special case of radiative equilibrium (Siegel and Howell [4]), the emission and absorption is in balance so

$$I_{b,P} = \left[I_{a,P} \equiv \frac{1}{4\pi} \int_{4\pi} I_P d\omega \approx \frac{1}{4\pi} \sum_{l}^{4\pi} I_P^l \omega^l \right] \tag{11}$$

where $I_{b,P} = \sigma T_P^4 / \pi$. Hence, the intensity field defines the temperature field.

The "explicit" solution procedure for solving for the radiation intensity distribution requires the following steps (for a black-wall enclosure).

1. A temperature distribution and an intensity field are guessed for the solution domain to define I_b and $\bar{I}^l$ at each node.

2. Based on the newly defined I_b and $\bar{I}^l$, R^l is evaluated using Eq. (6), which in turn is used to determine b_P^l.

3. The intensity equation (Eq. (9)) is solved at each node based on the b_P^l obtained from step 2.

4. As the intensity in each direction, I_P^l, is obtained from step 3, $\bar{I}^l$ is updated using Eq. (7). The updated $\bar{I}^l$ is used to re-calculate R^l and hence b_P^l for the solution of the intensity for the next l direction (Gauss Seidel update). Alternatively $\bar{I}^l$ could be updated after new intensities in all directions have been found (Jacobi update).

5. Once the intensities in all directions have been obtained, the blackbody intensity, I_b, is updated by Eq. (11) (Jacobi update).

6. Steps 2, 3, 4, and 5 are repeated until a pre-set convergence criterion is satisfied.

If the walls are partially reflecting, the starting (boundary) intensities for each direction l are calculated from the boundary emission and reflection into the ω^l direction, where the reflection is based on the most recently available incident intensities (i.e., Gauss-Seidel update). Reflective boundaries generally do not cause convergence difficulties so from this point on black boundaries are assumed.

4.1 Slow Convergence to Explicit Method

When the extinction coefficient vanishes ($\kappa \rightarrow 0$), term $T2$ in Eq. (5) and b_p^l in Eq. (9) vanish, and the explicit method provides correct interior intensities without iteration. The only important process in this limit is the transmission of radiant energy. As the extinction coefficient increases, the importance of b_p^l in the equation for I_p^l increases relative to the transmission terms. Because b_p^l contains 'lagged' information, the number of iterations required to find the interior intensities increases. For large κ, transmission of radiation (term $T1$ in Eq. (5)) becomes unimportant so the right side of Eq. (9) is totally dominated by b_p^l. Since b_p^l contains terms that are lagged, it is not surprising that the convergence of the explicit method becomes slow. For large enough κ the explicit method converges too slowly to be useful. The number of cycles required for convergence of the explicit method for problems involving both absorption and scattering will be presented in a later section, but the reader may get a preview by referring to Figs. 5 - 7.

5 A New Implicit Solution Scheme

The new scheme proposed in this study is a refinement of the implicit scheme suggested by Raithby and Chui [1]. It involves the formulation of a new equation that can be solved to provide an implicit update of the R^l values. This information will be described in a step-by-step manner in this section, and its deviation from the previous scheme will be noted. The dramatic reduction in the number of cycles to achieve convergence using the implicit update of R^l can again be previewed by reference to Figs. 5 - 7, but a detailed presentation of these test results is reserved for the next section.

5.1 Formation of the Radiant Energy Equation

The new equation is formulated based on the conservation of total radiant energy over each control volume. Since Eq. (9) ensures conservation of radiant energy balance over control volume P within the discrete solid angle ω^l, summing it all 4π solid angles will yield the equation that ensures *total* energy conservation over all directions:

$$\sum_{l}^{M} a_P^l I_P^l = \sum_{l}^{M} \sum_{nb} a_{nb}^l I_{nb}^l + \sum_{l}^{M} b_P^l \tag{12}$$

where M is the total number of solid angles so that $\sum_l^M \omega^l = 4\pi$. For a given direction l some of the coefficients a_{nb}^l will be zero but, after the summation, intensities from all eight neighbour nodes of P will appear.

After all terms involving R^l have been written in terms of nodal values, Eq. (6) is used to split each nodal value of R^l into its I_b and $\bar{I}^l$ components. For example, for node P,

$$R_P^l = \left[\frac{K_a}{\kappa}\right]_P I_{b,P} + \left[\frac{\sigma_s}{\kappa_a}\right]_P \bar{I}_P^l \tag{13}$$

Assembling all terms, and moving to the right side of the equation the terms that arose from the volume integration (i.e., the terms on the right side of Eq. (4), an equation of the following form is obtained:

$$\overbrace{\sum_{l}^{M} \hat{a}_P^l I_P^l}^{B} = \overbrace{\sum_{l}^{M} \sum_{nb} a_{nb}^l I_{nb}^l - \sum_{l}^{M} \hat{A}_P^l I_{b,P} + \sum_{l}^{M} \sum_{nb} \hat{A}_{nb}^l I_{b,nb}}^{C \quad D}$$

$$\underbrace{-\sum_{l}^{M} \bar{A}_P^l \bar{I}_P^l + \sum_{l}^{M} \sum_{nb} \bar{A}_{nb}^l \bar{I}_{nb}^l}_{E} \underbrace{-4\pi K_a V_P (I_{a,P} - I_{b,P})}_{F}$$

$$\underbrace{+\sigma_s V_P \sum_{l}^{M} I_P^l \omega^l - \sigma_s V_P \sum_{l}^{M} \bar{I}_P^l \omega^l}_{G=0} \tag{14}$$

In this equation terms B and C can be viewed as the source of radiant energy due to direct transmission from the neighbouring volumes, terms D and E incorporate the contributions of emission and scattering from the neighbours, and term F is the divergence of radiant flux within the control volume P. When the RTE (Eq. (1)) is integrated over all angles, the two terms involving scattering on the right side of

the equation cancel exactly. Provided $\bar{\Phi}$ in Eq. (7) is precisely evaluated, as already discussed, it can be shown that a similar cancellation occurs in the algebraic equation (i.e.,$G = 0$).

5.1.1 The Basic Issue

There is one total radiant energy balance given by Eq. (14) for each volume, but this equation contains intensities in M directions. To be useful, the equation must be reduced to an equation for a single unknown.

In the scheme proposed by Raithby and Chui [1], Eq. (14) was rewritten with scattering terms split into directionally independent and directionally dependent terms, and all directionally dependent terms (I^l and $\bar{I}^l$) in the equation were grouped into a source term that was explicitly updated. While this scheme was shown to greatly enhance convergence for isotropic scattering, the new implicit scheme presented here provides a significant additional improvement, especially for cases with strongly anisotropic scattering.

The present scheme introduces the concept of phase-weights to reduce Eq. (14) to an equation for a single variable.

5.1.2 The Concept of 'Phase Weights'

At a given location P, the intensity distribution is a three dimensional surface, where the distance from P to the surface in a given direction is the numerical value of intensity in that direction. The two important properties of intensity are its average value and its angular distribution. These two properties can be isolated by writing intensity at point P as

$$I_P(\theta, \phi) = \alpha_P(\theta, \phi) I_{a,P} \tag{15}$$

where α_P is the normalized intensity or 'phase weight'.

The finite volume method treats intensity as constant over each solid angle ω^l so the corresponding discrete form of Eq. (15) is

$$I_P^l = \alpha_P^l I_{a,P} \tag{16}$$

where, by the definition average intensity (Eq. (11)),

$$\sum_{l}^{4\pi} \alpha_p^l \omega^l = 4\pi \tag{17}$$

The decomposition represented by Eq. (16) provides exactly the form of equation needed to convert Eq. (14) into an equation for $I_{a,P}$.

5.1.3 Final equation for I_a

Inserting Eq. (16) into Eq. (7), the inscattering term $\bar{I}_P^l$ becomes

$$\bar{I}_P^l = \frac{1}{4\pi} I_{a,P} \sum_{l'}^{M} \alpha_P^{l'} \bar{\Phi} \tag{18}$$

Substituting this equation for $\bar{I}_P^l$, and Eq. (16) for I_P^l into Eq. (14), and rearranging the equation, results in

$$A_P^a I_{a,P} = \sum_{nb} A_{nb}^a I_{a,nb} - A_P^b I_{b,P} + \sum_{nb} A_{nb}^b I_{b,nb} + B_P \tag{19}$$

where all the phase weights have been included in the coefficients, and none of the directionally dependent terms (I^l or $\bar{I}^l$) is left in the source term B_P to be lagged (hence, $B_P = 0$ except at the boundary). This departure from the scheme suggested by Raithby and Chui [1] is the basis for the improvement convergence. When the detailed expressions for the coefficients are worked out it will be found that neglecting the derivative of R^l along the control volume surfaces causes the corner coefficients of I_b to be zero (i.e., $A_{NE}^b = A_{NN}^b = A_{SW}^b = A_{SE}^b = 0$). The solution of Eq. (19) provides the correct average intensity for each control volume, for a given set of phase weights and for a given medium temperature.

For a control volume that is adjacent to the boundary, like the one shown in Fig. 2b, the intensities originating from the boundary nodes (nodes SE, SW, and S in this case) are known from the boundary conditions. Hence, these intensities need not be written as a function of I_a and α^l; their contributions to the radiant energy balance are directly grouped into B_P, and the A^a coefficients are appropriately modified.

5.2 Solution of the Implicit Equation

5.2.1 Radiative Equilibrium

In general, Eq. (19) will have to be solved in conjunction with the thermal energy equation in order to establish the temperature (or $I_b = \sigma T^4/\pi$) and the average

intensity field (I_a) of the medium.

For the special case of radiative equilibrium (i.e., $I_{a,P} = I_{b,P}$) assumed in this work, Eq. (19) can be further simplified to

$$A_P^{ab} I_{b,P} = \sum_{nb} A_{nb}^{ab} I_{b,nb} + B_P^{ab} \tag{20}$$

where $A^{ab} = A^a + A^b$, and where $B_P^{ab} = 0$ except at the boundary.

Equation (20) is the implicit equation for I_b, relating $I_{b,P}$ to its neighbouring nodal values. Solution was obtained in this study by application of a line Gauss-Seidel solver. The specific steps in using the solution of this equation to update the R^l values will be addresed in the next section.

5.2.2 The Solution Procedure

Essentially, the solution procedure of the implicit scheme consists of two parts: the solution of intensity equation (i.e., (9)) to update the direction-dependent intensities (i.e., the phase weights α^l) and the solution of the implicit equation (i.e., (20)) to update I_b, I_a and hence, R^l. The completion of these two parts is regarded as one cycle (or one iteration). The actual steps in implementing this scheme are organized as follows:

1. A temperature distribution and an intensity field are prescribed at each node, and I_b and $\bar{I}^l$ are calculated.

2. Based on the newly defined I_b and $\bar{I}^l$, R^l is evaluated using Eq. (6), which in turn is used to determine b_P^l, the source term of Eq. (9).

3. Equation (9) is solved for I_P^l for each $l, l = 1, 2, ..., M$.

4. Based on the new intensity field, the average intensity $I_{a,P}$ is calculated and the distribution of phase weights at every node $P, \alpha_P^l = I_P^l / I_{a,P}$ is evaluated. In the event that $I_{a,P} = 0$ the phase weights are set to unity.

5. Using the newly evaluated phase weights, the coefficients of the implicit equation (i.e., (20)) are calculated and the implicit equation is solved to update the I_b field.

6. Because of radiative equilibrium ($I_{a,P} = I_{b,P}$), the updated I_b field represents the new estimate of $I_{a,P}$. Using the updated $I_{a,P}$ field and the phase weights obtained from step 4, the inscattering term $\bar{I}_P^l$ is updated with Eq. (18).

7. R_P^l is updated by the newly evaluated $I_{b,P}$ and $\bar{I}_P^l$ using Eq. (6), and b_P^l in Eq. (9) is calculated.

8. Steps 3 to 7 are repeated until a pre-set convergence criterion is achieved.

5.3 Evolution of Phase Weights

It is instructive to plot the phase-weight distribution to gain an understanding of the solution algorithm. To illustrate this, the simple problem shown in Fig. 3 is chosen: the cavity is square, its walls are black, the bottom wall is held at 100 K, the top and sidewalls are kept at $0K$, and the medium in the cavity is gray with absorption and emission ($K_a L = 3.0$) but no scattering ($\sigma_s = 0$). The cavity was subdivided into 3×3 control volumes using a uniform grid spacing, and a uniform angular distribution of $(N_\theta \times N_\phi) = (1 \times 12)$ was used. The initial temperature was set to $0K$ in the cavity.

The projection of the phase weights on to the $x - y$ phase at the center of the cavity is shown in Fig. 3. The dotted circle is the reference condition for isotropic intensity. At the end of the first solution cycle, the intensity is entirely upward, but after the update of the medium temperature the intensity distribution (on cycle 2) overshoots its converged distribution. The phase weight distribution does not change significantly beyond the third cycle.

6 Discussion of Test Results

The newly formulated implicit solution scheme was applied to a number of two dimensional Cartesian test cases that involved absorbing, emitting, and isotropically scattering media. In all cases, the implicit solution was found to have the same high degree of accuracy as reported by Raithby and Chui [1] using the explicit solution because the converged solution is independent of the solution method used. It is therefore appropriate in this section to focus mainly on results relating to convergence rate (i.e., how many cycles are required to achieve convergence) and computational effort (e.g., CPU time).

6.1 Comparison with $1D$ solution

In this case, the two dimensional implicit solution scheme is applied to the one dimensional radiant heat transfer in a plane medium (see Fig. 4). The medium is

anisotropically scattering with a constant scattering coefficient, but neither absorbs nor emits ($K_a = 0$). The medium is enclosed by two flat isothermal black plates at temperatures $T_T = 0$ and $T_B = 100K$. Radiative equilibrium is assumed. The objective is to determine the reflectance to the bottom wall caused by the scattering medium.

Analytical solutions to this problem have been obtained by Busbridge and Orchard [6] over the range of optical thicknesses ($\sigma_s L : 1 \rightarrow 10$) for the phase function

$$\Phi(\psi) = 1 + a\cos\psi \tag{21}$$

where ψ is the angle between $\vec{s}$ and $\vec{s'}$ in Eq. (2).

In the two dimensional code, this problem was approximated as a long rectangular box with aspect ratio 1 : 2000. A coarse spatial grid ($N_x \times N_y$) = (4×4) and a relatively fine angular grid ($N_\theta \times N_\phi$) = (8×16) were used.

If q_R is the radiant heat flux reflected back to the bottom wall, a nondimensional flux is defined by $q_R^* = q_R/\sigma(T_B^4 - T_T^4)$. Figure 4 shows the exact and predicted valued of q_R^* as a function of the optical thickness $\sigma_s L$ over the range 1.0 to 10, and for asymmetry factors a in Eq. (21) of 0.5 and 1.0.

It is remarkable that with such a coarse spatial grid (4×4) the maximum deviation of the q_R^* prediction from the exact solutions (shown as solid lines) is only 0.8%, occurring at the lowest optical thickness. But of more direct interest to the present paper, very few cycles (maximum 13) were required in the solution procedure to obtain a q_R^* that changes less than 0.01% between cycles. In contrast, the explicit scheme needs 40 cycles for $\sigma_s L = 5$, and the number of cycles increases sharply with increasing $\sigma_s L$.

6.2 Tests in a $2D$ Enclosure

The previous test case demonstrates the capability of the implicit scheme applied to a two dimensional enclosure with asymtotically high aspect ratio. Now only a simple square enclosure will be used to study the convergence behavior of the scheme over a wider range of optical thicknesses.

The walls of the square enclosure (see Fig. 5) are assumed black and isothermal with temperature set at T_c on the top and the two side walls, whereas the bottom wall has a higher temperature T_h. Radiative equilibrium is assumed, and in all cases the medium temperature must be found as part of the solution. Both the explicit

and implicit schemes were applied to obtain the net dimensionless radiant heat flux leaving the hot wall, $q_h^* = q_h/\sigma(T_h^4 - T_c^4)$. One set of spatial and angular grids $(N_x \times N_y) \times (N_\theta \times N_\phi) = (4 \times 4) \times (2 \times 8)$ was used throughout these runs. The convergence criterion was always fixed at: (change in q_h^* between cycles) $\leq 0.01\%$, and the convergence rate is measured as the number of R^l updates required to meet this criterion.

6.2.1 Case 1: Absorbing-emitting medium

In this case, the enclosed medium is assumed to be absorbing, emitting, and non-scattering($\sigma_s = 0$). Therefore, the R^l values are equivalent to the I_b values (see Eq. (6)). The number of cycles (or I_b updates) required to attain convergence, is plotted as a function of optical thickness ($K_a L$) in Fig. 5 for both the explicit and implicit schemes.

The explicit scheme is seen to converge quickly for $K_a L \to 0$, but the number of cycles required rises sharply for $K_a L > 1$, with the result that the practical usefulness of the scheme becomes questionable for $K_a L > 10$.

The dashed line in Fig. 5 shows that the implicit scheme satisfies the convergence criterion in two or three cycles for both small and large values of $K_a L$. When $K_a L$ is small, b_p^l in Eq. (9) is small so that the first solution of this equation yields very close to the correct intensities; a second cycle is required only to apply the convergence criterion. For $K_a L \to \infty$, the first solution of Eq. (20) yields the correct value of $I_{b,p}$ so that correct values of R_p^l and therefore b_p^l yield converged intensities on the second solution of Eq. (9). For intermediate $K_a L$, a maximum of seven iterations is required to account for the coupling. It is concluded that the implicit method greatly accelerates convergence. Indeed, for strongly participating media, $K_a L > 10$, the implicit method is required for practical solution of the intensity equations.

6.2.2 Case 2: Isotropically scattering medium

The convergence rate of the isotropically scattering case is shown in Fig. 6 for the same range of optical thicknesses, $\sigma_s L : 0.01 \to 2000$. The result is almost identical to the previous plot. The difference is in the R^l values, which in this case contain only the inscattering term $\bar{I}^l$. According to section 4, the explicit update of $\bar{I}^l$ is done in a Gauss-Seidel manner, which in theory is slightly more efficient than the explicit Jacobi update of I_b used in previous case. For example, the number of cycles required at optical thickness of 10 is 65 in this case as opposed to 108 in the absorbing-emitting

case (see Fig. 6). However, the overall convergence rate of the explicit method remains unsatisfactory when $\sigma_s L$ is large.

For the same reason explained in Case 1, the implicit scheme attains convergence much more quickly over the tested range of optical thicknesses. The maximum number of updates required is only 8, occurring at $\sigma_s L = 3$ to 5.

6.2.3 Case 3: Absorbing-emitting-isotropically scattering medium

Although the implicit scheme requires fewer iterations than the explicit scheme, as shown in case 1 and 2, each cycle may appear to be more costly because of the additional computational effort needed to solve the implicit equation for I_b. This case focuses on determining if there is an actual saving in computational cost in using the implicit scheme.

The medium is assumed to be absorbing, emitting and isotropically scattering. Both the absorption and scattering coefficients are allowed to vary but the scattering albedo, $\omega_s = \sigma_s/(\sigma_s + K_a)$, is always maintained at 0.5, keeping the two coefficients in equal strength.

The comparison between the convergence rates of the explicit and implicit schemes is shown in Table 1. The range of optical thickness, $\kappa^* = (\sigma_s + K_a)L$, covered in the test is 1 to 30. Within this range, the saving in CPU expense by the implicit scheme increases from about 1.4 to 22 times. Even with the additional computational effort in solving the implicit equation, the implicit scheme is still substantially cheaper. If κ^* is increased beyond 30, larger savings in CPU cost are expected because the convergence rate of the explicit scheme will quickly worsen, but the implicit scheme will achieve convergence even more quickly for larger κ^*.

6.2.4 Case 4: Anisotropically scattering medium

In this case, a non-isotropically scattering medium is introduced to the enclosure. The scattering phase function is represented by the delta-Eddington approximation (see Joseph and Wiscombe, 1976),

$$\Phi(\psi) = 2f\delta(1 - cos\psi) + (1 - f)(1 + 3gcos\psi) \qquad (22)$$

where ψ is the scattering angle. The forward scattering factor 'f' is assumed to be 0.5 and the asymmetry factor 'g', 0.3.

Optical Thickness $(K_a + \sigma_s)L$	Number of R^l-Updates		Gain in CPU CPU(explicit)/ CPU(implicit)
	Explicit Scheme	Implicit Scheme	
1.0	8	7	1.4
5.0	25	10	4.1
10.0	51	10	8.6
15.0	83	11	12.2
20.0	118	11	16.6
30.0	192	12	21.7

Table 1: Comparison of CPU expenses between the implicit and explicit schemes applied to a square enclosure with an absorbing, emitting, and isotropically scattering medium.

The convergence rates for both the explicit and implicit schemes are illustrated in Fig. 7. The curve for the explicit case, shown as a solid line, exhibits the same characteristics as discussed before. The convergence rate for the implicit scheme, plotted as a dashed line, is again much improved from the explicit method, but unlike the previous case, the improvement in the convergence rate at large $\sigma_s L$ was not as significant.

To understand why convergence does not improve with increasing $\sigma_s L$ for anisotropic scattering, consider the case where $\sigma_s L = K_a L \rightarrow \infty$. In this limit, the intensity at any particular point is determined mainly by emission and inscattering since transmission of radiation from upstream is eliminated by absorption and outscattering. For isotropic scattering the scattering term is, by definition, independent of direction so that (in this $\sigma_s L \rightarrow \infty$ limit) there are no terms in Eq. (20) that are directionlly dependent. As seen in cases 1 and 2, Eq. (20) immediately yields correct values of I_b (and therefore R^l). If the scattering is anisotropic, term E in Equation (14), containing $\bar{I}^l$, retains a strong directional dependence that must be determined from the solution of Eq. (9) for I^l. For strongly anisotropic scattering, a strong coupling between the intensity and radiant energy equations is retained for large $\sigma_s L$. Even though anisotropic scattering adversely affects its performance, the implicit method is essential to obtaining solutions at all for large $\sigma_s L$ problems.

7 Summary of Discussion

The convergence rate of discrete methods used to solve the radiation transport equations becomes slow when the medium becomes strongly participating. Using the Finite Volume formulation, this paper shows that it is possible to greatly accelerate convergence and achieve practical solutions for any strength of absorption and/or scattering. In fact, for strongly absorbing and/or strongly isotropically scattering media, the implicit method advanced in this paper results in greatly accelerated convergence. If scattering is strong and strongly anisotropic, the convergence rate is slowed but economical solutions are still achievable.

The performance of the proposed implicit scheme has been demonstrated for geometrically simple problems in which radiative equilibrium prevails. If radiative equilibrium does not exist, a thermal energy equation must be solved to obtain the medium temperature. For such cases, and for geometrically more complex problems, the implicit formulation is believed to be equally crucial if economical solutions are to be achieved.

The principles underlying the implicit method presented here are believed to apply equally well to other discrete methods of solving the radiation transport equations.

Acknowledgements

This work was supported by a contract from the Combustion and Carbonization Research Laboratory, CANMET, of the Energy Mines and Resources Department of the Canadian Federal Government, under the scientific authority of P. Hughes. The authors are also grateful for the additional financial assistance received from the Natural Sciences and Engineering Research Council of Canada.

References

[1] Raithby, G.D. and Chui, E.H. (1990) 'A Finite-Volume Method for Predicting Radiant Heat Transfer in Enclosures with Participating Media,' *Journal of Heat Transfer*, Vol. 112, pp. 415-423.

[2] Viskanta, R. and Mengüç, M.P. (1987) 'Radiation Heat Transfer in Combustion Systems,' *Progress in Energy and Combustion Science*, Vol. 13, No. 2, pp. 97-160.

[3] Lewis, E.E. and Miller, Jr., W.F. (1984) *Computational Methods of Neutron Transport*, John Wiley and Son Inc., New York.

[4] Siegel, R. and Howell, J.R. (1981) *Thermal Radiation Heat Transfer*, Second Edition, McGraw Hill, New York, London, pp. 453-460.

[5] Chui, E.H., Raithby, G.D. and Hughes, P.M.J. (1991) 'Prediction of Radiative Transfer in Cylindrical Enclosures by the Finite Volume Method,' to be submitted to *J. Thermophysics*,

[6] Busbridge, I.W. and Orchard, S.E. (1967) 'Reflection and Transmission of Light by a thick Atmosphere according to a Phase Function: $1 + x\cos\theta$,' *The Astrophysical Journal*, Vol. 149, pp. 655-664.

[7] Joseph, J.H. and Wiscombe, W.J. (1976) 'The Delta-Eddington Approximation for Radiative Heat Transfer,' *Journal of Atmospheric Sciences*, Vol. 33, pp. 2452 - 2459.

Nomenclature

A_f	area of surface panel f, m^2
I	radiant intensity, $W/(m^2\ sr)$
$\bar{I}^l$	in-scattering intensity, Eqs. (2) and (7)
I_a	average intensity, Eq. (11)
I_b	blackbody intensity, $\sigma T^4/\pi$
I^l_f	intensity at integration point f within ω^l
I^l_P	intensity at node P within ω^l
I^l_{uf}	upstream intensity for integration point f within ω^l
K_a	absorption coefficient, m^{-1}
L	representative dimension of a given geometry, m
M	total number of discrete solid angles
N_x, N_y	number of control volumes in the x and y directions
N_θ, N_ϕ	number of discrete angles in polar (θ) and azimuthal (ϕ) directions
$\vec{n}$	unit outward normal to surface panel f
q	radiant heat flux, W/m^2
Q^l_f	radiant energy with ω^l crossing surface panel f, W
$\vec{r}$	position vector
R^l	the intensity source function within ω^l, Eq. (6)
s	distance in direction of $\vec{s}, m$
$\vec{s}$	unit direction vector
S	path length, m
T	temperature, K
V	volume, m^3

Greek Symbols

α^l	phase weight, Eq. (18)
δ	Kronecker delta function, Eq. (22)
θ	polar angle, Fig. 1a

κ	extinction coefficient, $K_a + \sigma_s, m^{-1}$
σ	Stefan-Boltzmann's constant
σ_s	scattering coefficient, m^{-1}
ϕ	azimuthal angle, Fig. 1a
Φ	scattering phase function, Eq. (2)
$\bar{\Phi}$	new variable for phase function, Eq. (8)
ψ	scattering angle, between $\vec{s}$ and $\vec{s'}$ in Eq. (2)
ω_s	scattering albedo, $\sigma_s/(\sigma_s + K_a)$
ω	solid angle, sr

Superscripts and Subscripts

b	refers to blackbody
f	refers to panel f on the surface of a control volume
l	associated with solid angle ω^l
nb	refers to neighbour nodes
N, S, E, W	refer to north, south, east, west
NW, NE, SW, SE	refer to northwest, northeast, southwest, southeast
P	refers to nodal point P
s	refers to a control volume surface
u	refers to an upstream position
w	refers to the boundary
x, y, z	refers to the x, y and z directions

Figure 1: Angular discretization (a), and spatial discretization in to control volumes (b)

Figure 2: The control volume centered at P, with the control volume surface divided into two panels and with integration points $f = 1, 2, ..., 8$ centered in each panel (a). Part (b) shows node labelling fera control volume adjacent to the lower boundary.

Figure 3: Evolution of the phase weight (α^l) at node P in the middle of the cavity with iteration cycle.

Figure 4: Nondimensional reflectance on the hot bottom wall for optical thickness $\sigma_s L = 1.0$ to 10.0 with two different scattering phase functions.

Figure 5: The number of R^l-update cycles required to obtain a wall heat transfer that changed less than 0.01% between cycles for an absorbing-emitting medium. $(N_x \times N_y) \times (N_\theta \times N_\phi) = (4 \times 4) \times (2 \times 8)$

Figure 6: The number of R^l-update cycles required to obtain a wall heat transfer that changed less than 0.01% between cycles for an isotropically scattering medium. $(N_x \times N_y) \times (N_\theta \times N_\phi) = (4 \times 4) \times (2 \times 8)$

Figure 7: The number of R^l-update cycles required to obtain a wall heat transfer that changed less than 0.01% between cycles for an anisotropically scattering medium. $(N_x \times N_y) \times (N_\theta \times N_\phi) = (4 \times 4) \times (2 \times 8)$

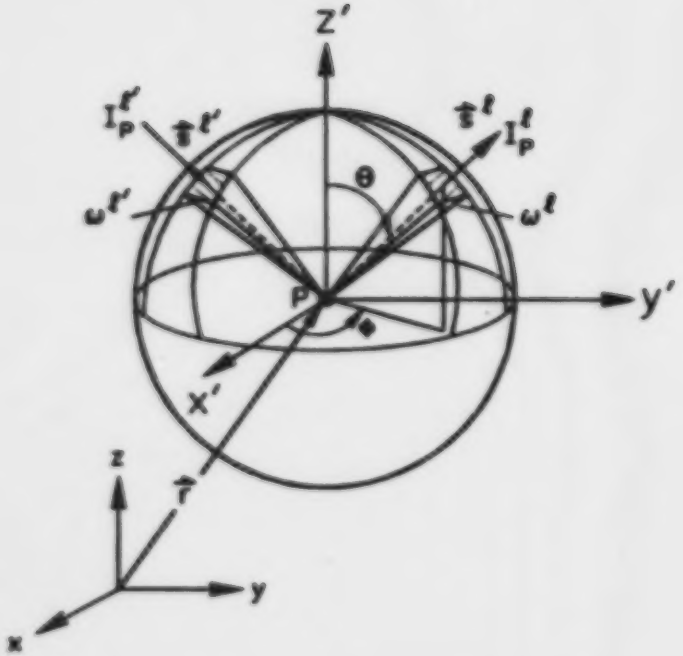

ANGULAR DISCRETIZATION

(a)

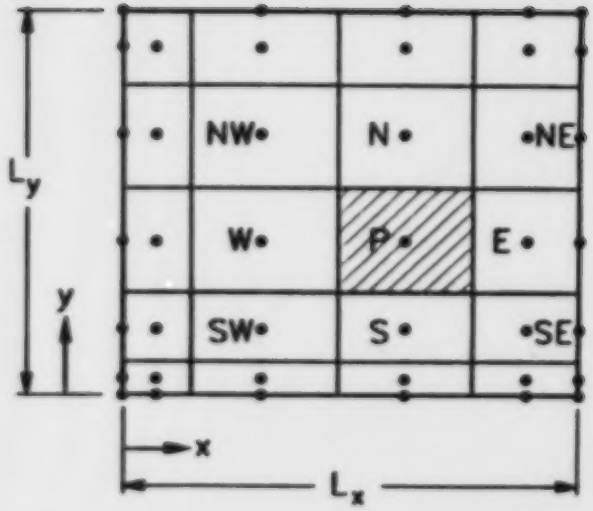

SPATIAL DISCRETIZATION

(b)

Figure 1: Angular discretisation (a), and spatial discretization in to control volumes (b)

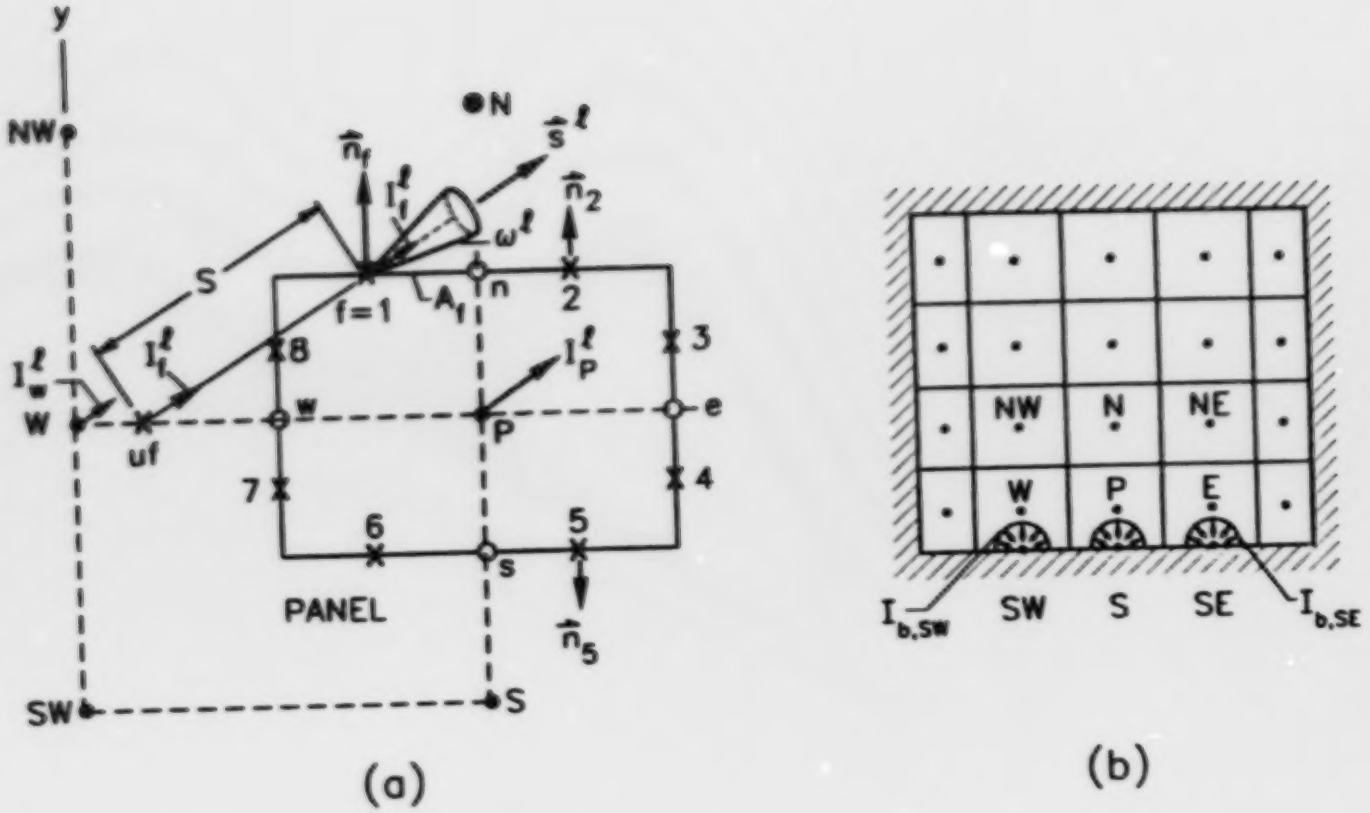

Figure 2: The control volume centered at P, with the control volume surface divided into two panels and with integration points $f = 1, 2, ..., 8$ centered in each panel (a). Part (b) shows node labelling fera control volume adjacent to the lower boundary.

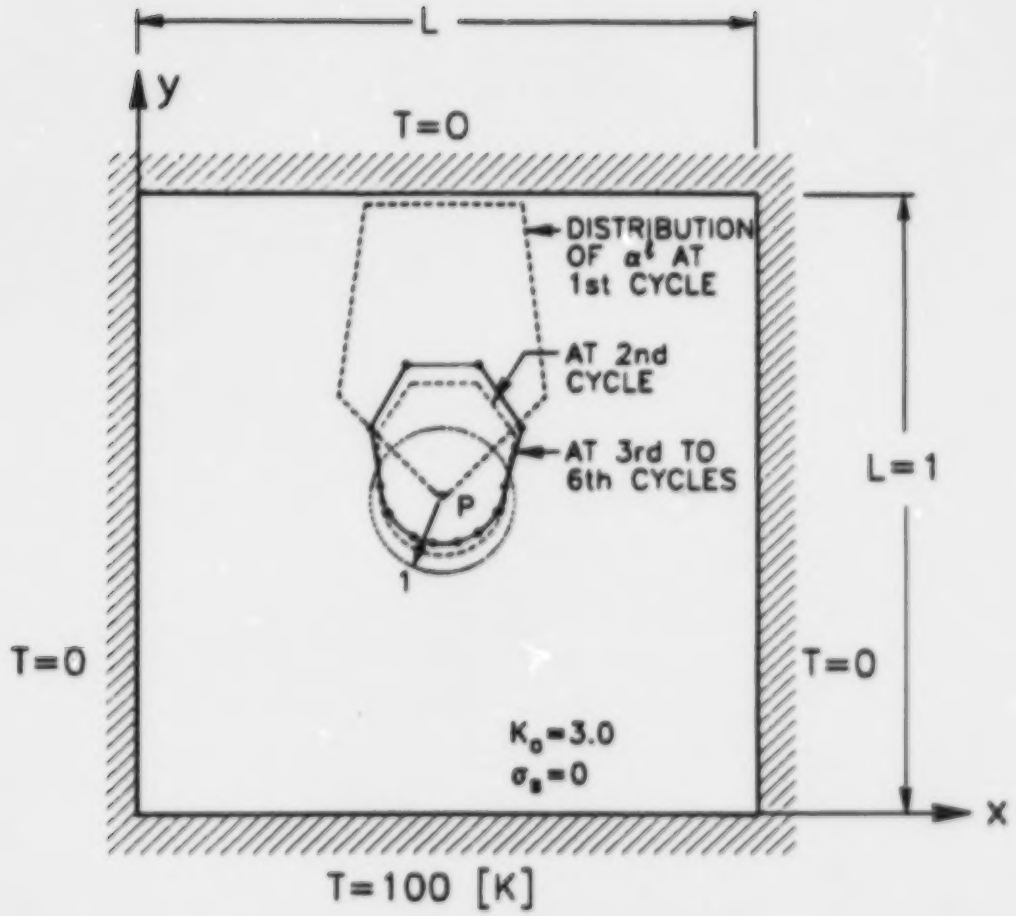

Figure 3: Evolution of the phase weight (α^l) at node P in the middle of the cavity with iteration cycle.

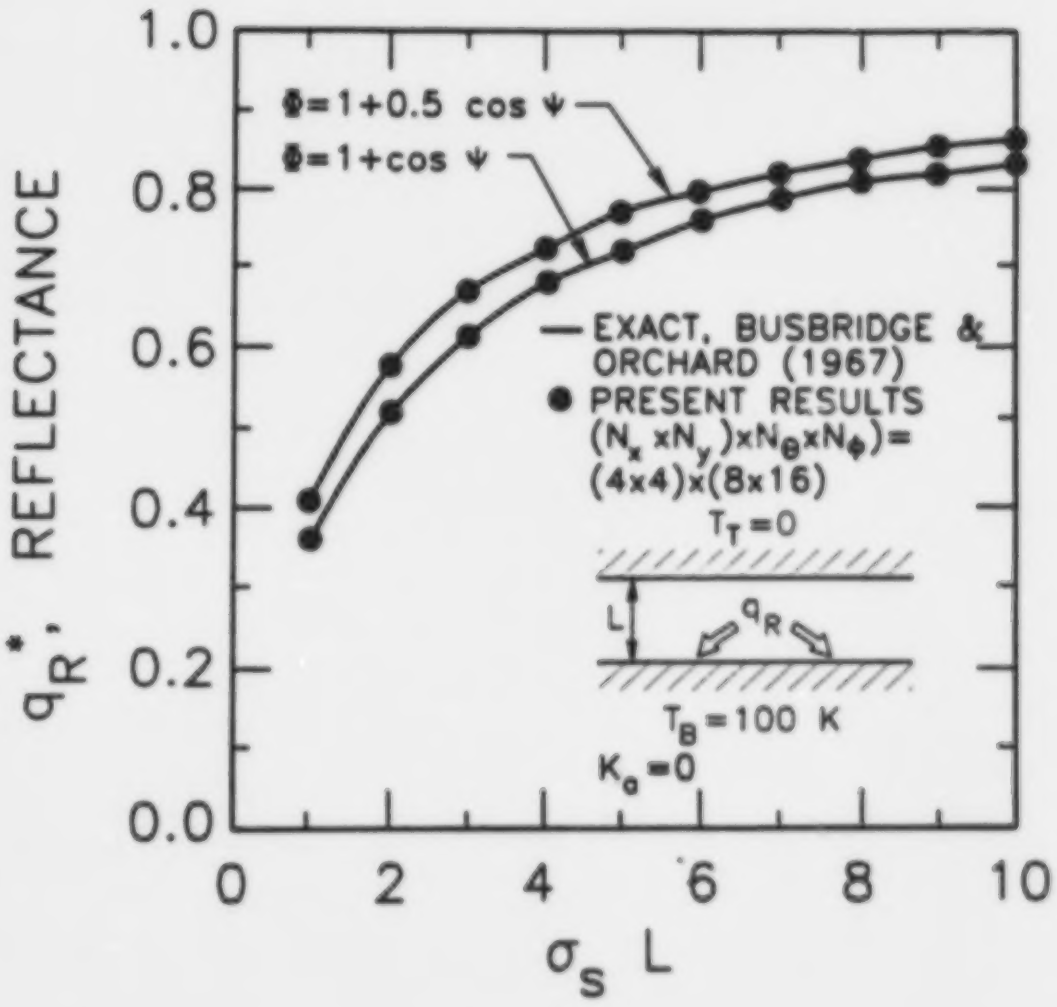

Figure 4: Nondimensional reflectance on the hot bottom wall for optical thickness $\sigma_s L = 1.0$ to 10.0 with two different scattering phase functions.

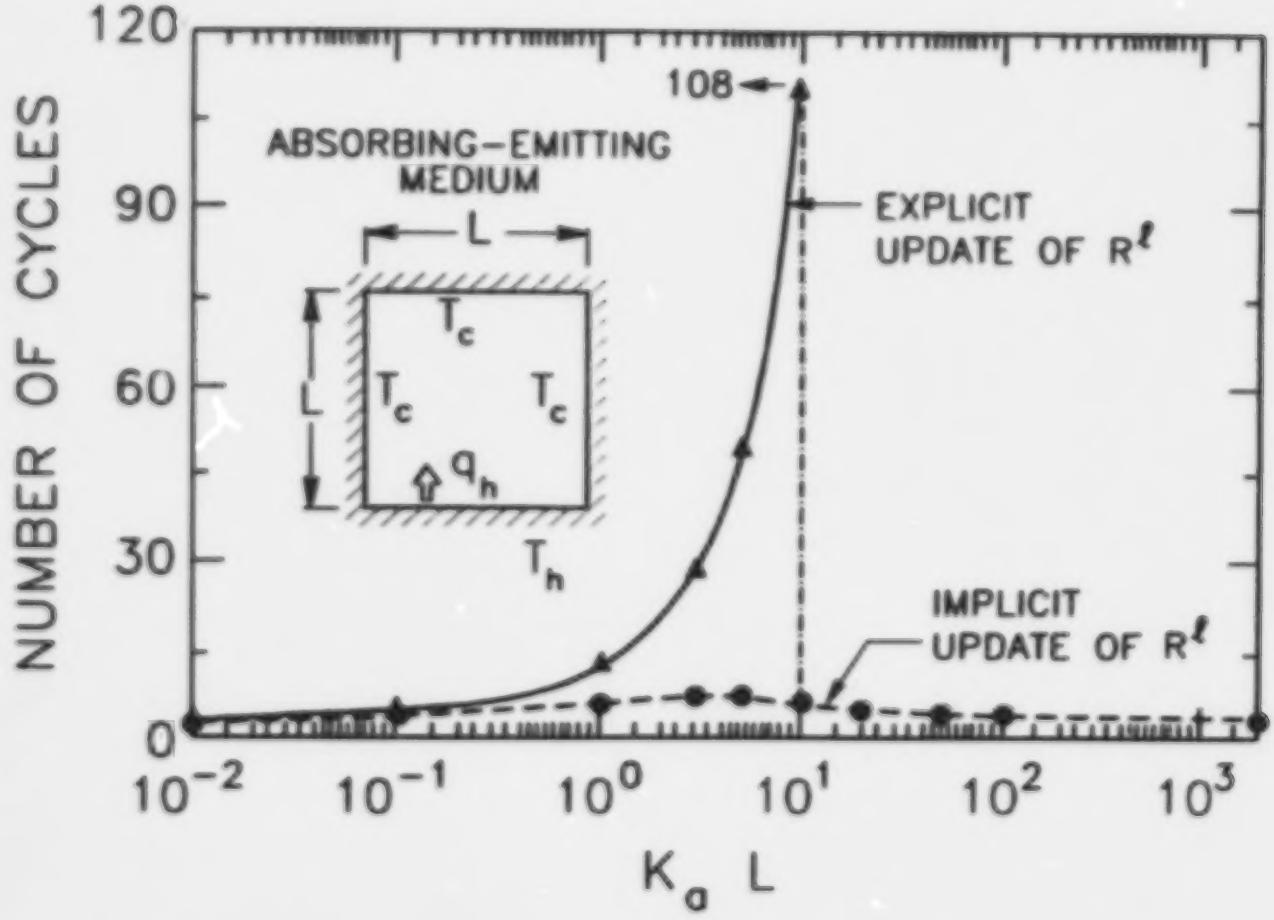

Figure 5: The number of R^l-update cycles required to obtain a wall heat transfer that changed less than 0.01% between cycles for an absorbing-emitting medium. $(N_\phi \times N_\eta) \times (N_\theta \times N_\psi) = (4 \times 4) \times (2 \times 8)$

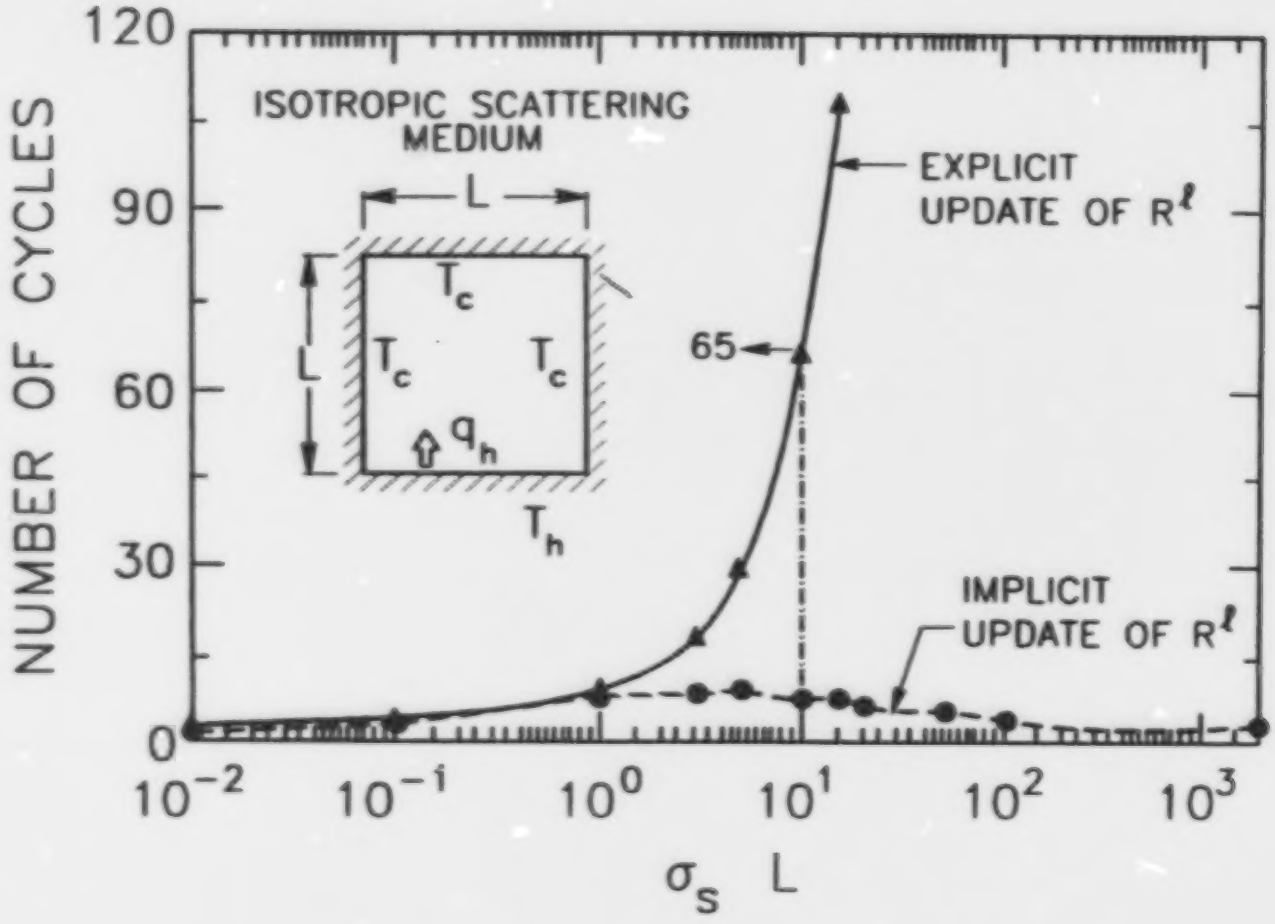

Figure 6: The number of R^l-update cycles required to obtain a wall heat transfer that changed less than 0.01% between cycles for an isotropically scattering medium. $(N_\mu \times N_\nu)$ $(N_\theta \times N_\phi) = (4 \times 4) \times (2 \times 8)$

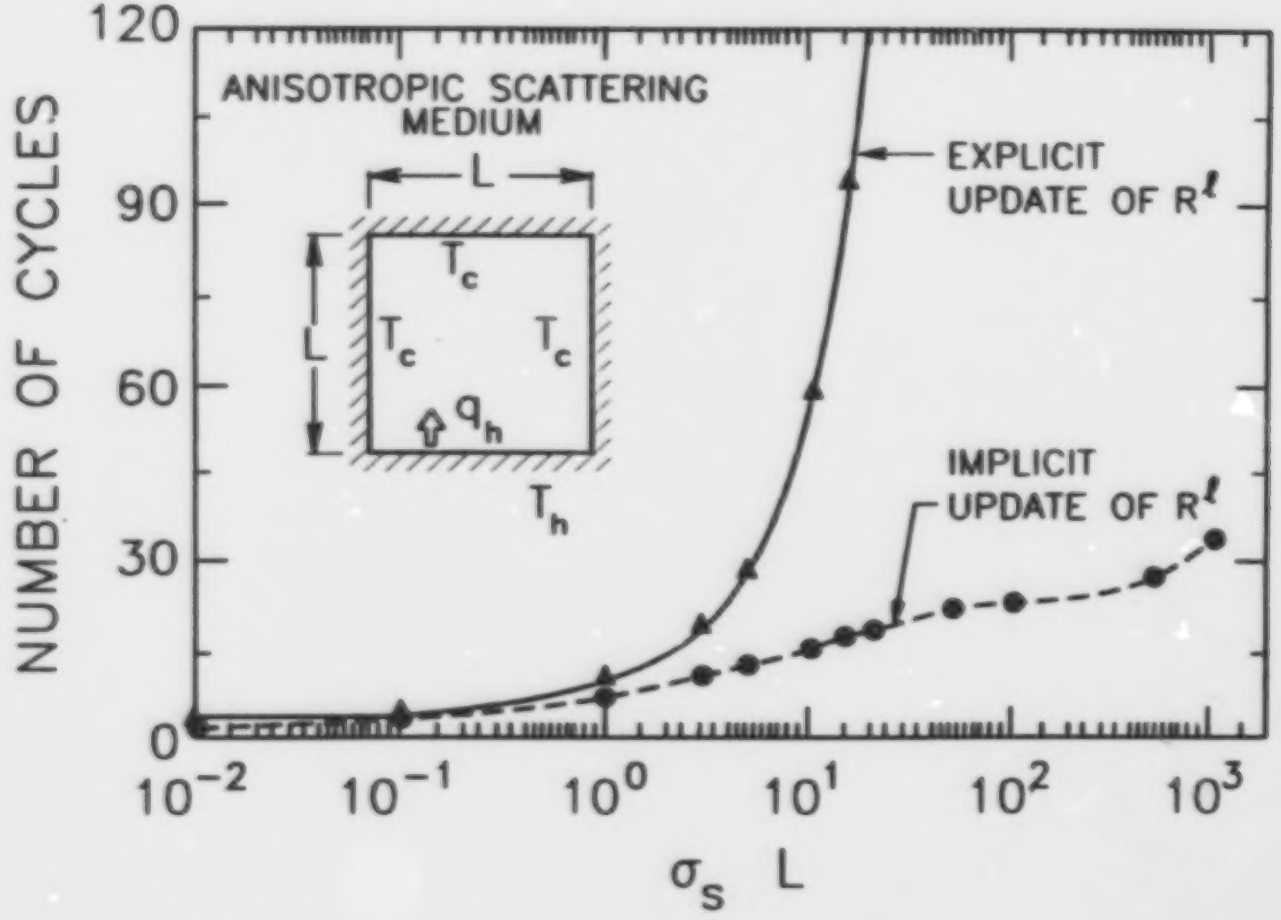

Figure 7: The number of R^l-update cycles required to obtain a wall heat transfer that changed less than 0.01% between cycles for an anisotropically scattering medium. $(N_\mu \times N_\eta) \times (N_\theta \times N_\phi) = (4 \times 4) \times (2 \times 8)$

13 Appendix E - Application of the Finite-Volume Method to Non-Orthogonal Computational Meshes

s^l (see Fig.3a) were known, the RTE could be integrated to relate I_f^l to I_{uf}^l. The actual value of I_f^l would depend on the processes affecting the radiation as it passes from uf to f. Representing these processes by a two-term Taylor series expansion about point f, Raithby and Chui[13] showed that

$$I_f^l = I_{uf}^l e^{-\kappa_f s} + R_f^l (1 - e^{-\kappa_f s}) - \frac{1}{\kappa_f} \left(\frac{\partial R^l}{\partial s^l} \right)_f \left[1 - e^{-\kappa_f s} (1 + \kappa_f s) \right] \qquad (5)$$

where the extinction coefficient κ and variable R^l are defined as

$$\kappa = K_a + \sigma_s \qquad R^l = \frac{K_a I_b + \sigma_s \bar{I}^l}{\kappa} \qquad (6)$$

Retention of the ~~third~~ last term in Eq.(5) is crucial if the FVM is to reduce exactly to the diffusion model of radiation for large κ.

In providing an equation for I_f^l, Eq. (5) introduces the new unknowns I_{uf}^l, R_f^l and the directional derivative $\left(\frac{\partial R^l}{\partial s^l} \right)_f$. A method of evaluating I_{uf}^l is now introduced.

The control volume in Fig. 3a is a perspective view of the control volume centred at P in Fig. 2, for which five of the twenty-seven neighbour nodes are A, B, C, D and E. The location of the integration point f = 1 in Figs. 2b and 3a, as well as several nodes, are shown in Fig. 3b. It is important to note that the surface A-B-C-P in Fig. 3b is not a control-volume

surface, but is rather a surface of constant z that passes through the nodes. The point f = 1 lies on the control volume surface. The dashed line that passes through the point f = 1 in Fig. 3b lies in the direction of $\vec{s}^l$, and intersects the surface A-B-C-P at point u1. The value of I^l_{u1} is approximated from the surrounding nodal point values of I^l (*i.e.* I^l_P, I^l_A, I^l_B, I^l_C) using bilinear interpolation[17], which requires use of a local β,γ co-ordinate system where $\gamma = \pm 1$ and $\beta = \pm 1$ on the boundaries shown in Fig. 3b.

For some directions, for example $(\vec{s}^l)^*$ in Fig. 3b, the upstream intersection u1* falls on the extension of the plane A-B-G-F, so the above prescription must be modified if the computational molecule is to be kept simple. For this case, $I^l_{u1^*}$ is replaced by $I^l_{u1^{**}}$, where u1** is the projection along the z axis, onto the A-B-C-P plane, and where its value is found by linear interpolation.

A similar strategy is followed for other solid angles ω^l and for other integration points (f = 2, 3,..., 6). The general rule for locating I^l_f for any control volume P is that no interpolation should be done using nodes that lie "downstream" of P. This practice yields an algebraic equation for I^l_P that (except for boundary conditions and inscattering) involves only nodes upstream of P, so the solution for I^l_P can be marched from the upstream boundary to the downstream boundary of the computational domain. The price paid for the simplicity and convenience of such a scheme is loss of accuracy. For points like u1 in Fig. 3b that lie on an

upstream plane, the bilinear interpolation for I^l_{nl} is second order accurate with spatial grid refinement, while approximating I^l_{nl*} by I^l_{nl**} results in a first order accurate estimate. Since the resulting radiant energy transfer (summed over all l) involves some first and some second order approximations, the discretization error in the heat transfer prediction is expected to reduce with refinement of the spatial grid at a rate between first and second order.

Final Form of Governing Equation

Replacing each I^l_f values in Eq. (4) by Eq. (5), in which I^l_{nf} is found by the method just described and where both R^l_f and $(\partial R^l_f/\partial x)_f$ are assumed known (see following section), the following equation for I^l_P results:

$$a^l_P I^l_P = a^l_A I^l_A + a^l_B I^l_B + a^l_C I^l_C + a^l_D I^l_D + a^l_E I^l_E + a^l_F I^l_F + a^l_G I^l_G + b^l_P \qquad (7)$$

This equation is valid for those S^l directions (shown in Fig. 3b) where the nodes included all lie upstream of P, and where all other terms have been lumped into b^l_P.

Evaluation of R^l_f and $(\partial R^l/\partial x^k)_f$

Completion of the model requires evaluation of R^l_f and its directional derivative, along S^l, for each integration point, f. R^l_f values within the medium and on the boundary were simply

found by interpolation and extrapolation respectively using values of R^l stored at nodes. The directional derivative at each f has three components, one along each co-ordinate direction. In the present implementation of the FVM, only the component normal to the surface was retained. This was done to simplify the algebra and in recognition that neither the formal accuracy of the method nor its ability to capture the diffuse limit is affected. The directional derivative term was therefore estimated from the nodal point values straddling the face from a central difference approximation. The values of R_f^l and its directional derivative are therefore easily expressed in terms of nodal values like R_p^l.

To calculate the nodal values of R_p^l by Eq. (6) requires that $I_{b,p}$ and $\bar{I}_p^l$ be known. $I_{b,p}$ follows immediately from the temperature at P. To evaluate $\bar{I}_p^l$, from Eq. (2) requires accounting for inscattering from all directions $\bar{s}'$ towards $\bar{s}$. Because ω^l is the solid angle centered on $\bar{s}^l$ and $I(\bar{s})$ is taken as constant over ω^r (no prime) and equal to I^r (no prime), so too is ω^r centered on $\bar{s}^r$ and $I(\bar{s}')$ is constant over ω^r and equal to I^r. Carrying out the 4π integration indicated in Eq. (2) to obtain $\bar{I}(\bar{s})$, then carrying out the integration of this $\bar{I}(\bar{s})$ over ω^l to obtain $\bar{I}^l$, $\bar{I}_p^l$ is given by

$$\bar{I}_p^l = \frac{1}{4\pi} \sum_r I_p^r \, \bar{\Phi} \, (\omega^r, \omega^l) \tag{8A}$$

where the summation includes all solid angles and where

$$\bar{\Phi} \, (\omega^r, \omega^l) = \frac{1}{\omega^l} \int_{\omega^l} \int_{\omega^r} \Phi \, (\bar{s}', \bar{s}) \, d\omega' d\omega \tag{8B}$$

The phase function $\Phi \, (\bar{s}', \bar{s})$ is given by some model, so $\bar{\Phi} \, (\omega^r, \omega^l)$ is obtained by analytical or numerical integration. For precise conservation of scattered energy, it is important that this integration be accurately performed.

Usually scattering calculations assume that the phase function depends only on the angle ψ between $\bar{s}'$ and $\bar{s}$, and not on the absolute incident ($\bar{s}'$) and scattering ($\bar{s}$) directions. Through Eq.(8B), the present FVM easily accommodates Φ's that depend on absolute directions, and this permits relatively easy radiant calculations in matrices, such as insulation or foamed ceramics.

Boundary Conditions

In this analysis, all boundaries are assumed diffuse-gray. For a surface at temperature T_s, the boundary condition for the surface intensity, I_s, radiating into the medium, is

$$I_s = \left[(1 - \epsilon_s) \sum_{\zeta_s} Q_s^{\zeta_s} + \epsilon_s A_s \, \sigma T_s^4 \right] \frac{1}{\pi A_s} \tag{9}$$

The first term on the right side of Eq. (9) is the reflected component, where the summation is over all incoming radiation. The second term arises from surface emission.

Explicit Solution Procedure

The simplest solution procedure is to start with a guessed intensity field (for each location and direction) evaluate R^I, form and solve an equation such as (7) for each direction, and for each node, and use this updated intensity field as the starting point of a new iteration. This procedure converges quickly when the medium is weakly participating. Details are provided after the model is specialized to apply to axisymmetric problems.

AXISYMMETRIC RADIATION

Attention is now turned to reducing the general 3D model just presented to axisymmetric problems. This is not a simple task until a mapping is understood. This section first describes the mapping, and then presents the details of how the 3D model is applied.

Governing Equation

In circular cylinder co-ordinates (Fig. 1), the radiation intensity I depends on position $\vec{R}(r, \varphi_o, z)$ and direction $\vec{s}(\theta, \phi)$. The RTE, Eq.(1). in these co-ordinates becomes (see Pomraning[15])

$$\left(\mu\frac{\partial}{\partial r} + \frac{\eta}{r}\frac{\partial}{\partial \varphi_o} + \xi\frac{\partial}{\partial z} - \frac{\eta}{r}\frac{\partial}{\partial \phi}\right) I\,(r, \varphi_o, z, \theta, \phi) = -\,(K_a + \sigma_s)\,I(r, \varphi_o, z, \theta, \phi) + K_a\, I_b\,(r, \varphi_o, z) + \frac{\sigma_s}{4\pi}\int_{4\pi} I\,(r, \varphi_o, z, \theta', \phi')\,\Phi\,(\theta', \phi', \theta, \phi)\,d\omega' \qquad (10)$$

where μ, η and ξ are direction cosines defined as:

$$\mu = \sin\theta\cos\phi, \quad \eta = \sin\theta\sin\phi, \quad \xi = \cos\theta \tag{11}$$

If axisymmetry exists, the intensity distribution becomes, by definition, invariant with φ_o so that the RTE for the axisymmetry intensity $I(r, z, \theta, \phi)$ reduces to

$$\left(\mu\frac{\partial}{\partial r} + \xi\frac{\partial}{\partial z} - \frac{\eta}{r}\frac{\partial}{\partial\phi}\right) I(r, z, \theta, \phi) = -(K_a + \sigma_s)\, I(r, z, \theta, \phi) + K_a I_b(r, z) + \sigma_s \bar{I}(r, z, \theta, \phi) \tag{12}$$

where

$$\sigma_s \bar{I}(r, z, \theta, \phi) = \frac{\sigma_s}{4\pi}\int_{4\pi} I(r, z, \theta', \phi')\, \Phi(\theta, \phi, \theta', \phi')\, d\omega' \tag{13}$$

Mapping for Solution of Axisymmetric Problems

Axisymmetric radiant heat transfer occurs when the intensity is independent of φ_o and is therefore completely specified by r, z, θ and ϕ, as just discussed. The intensities shown in Fig. 4a all have the same values of r, z and θ. The angle $\Delta\varphi_o$ between all numbered points is $\pi/4$. The points 1, 2, 3, ... are located at $\varphi_o = 7\pi/8, 5\pi/8, 3\pi/8$ ... respectively, and the angle φ_r is zero for each intensity. The angles $\phi = \varphi_r - \varphi_o$ for the intensities I_1^1, I_2^1, I_3^1,... are therefore $-7\pi/8, -5\pi/8, -3\pi/8$,... .

In Fig. 2b, the intensities all have the same values of r, z and θ as in Fig. 2a, but are now all located at $\varphi_o = 7\pi/8$, with $\varphi_r = 0, \pi/4, \pi/2$, ... for the intensities I_1^1, I_1^2, I_1^3, ... The

$\phi = \varphi_r - \varphi_e$ angles are therefore $-7\pi/8$, $-5\pi/8$, $-3\pi/8$, ... respectively. It follows that the values of r, z, θ, and ϕ are the same for I_j^1 in Fig. 4a and I_1^j in Fig. 4b, j = 1, 2, 3, ... 8, and (since r, z, θ and ϕ completely specify the intensity when axisymmetry prevails) therefore $I_j^1 = I_1^j$. A simple mapping therefore exists between the intensities in Figs. 4a and 4b; in calculating intensities, it will often be easier to compute the intensities depicted in Fig. 4a.

For the integral equations for the intensities in Figs. 4a and 4b to be exactly the same, the $\Delta\varphi_e$ spacing between nodes in Fig. 4a should be uniform and equal to the $\Delta\varphi_r$ spacing between the intensity directions in Fig. 4b, and the discrete solid angle ω^l used when the FVM is applied to Fig. 4a should extend from $-\Delta\varphi_r/2$ to $+\Delta\varphi_r/2$ (see Fig. 2c). Carlson and Lathrop[19] introduced an artifice into their Discrete Ordinates Method in order to avoid difficulties (lack of conservation and unphysical directional coupling) that arose from the third term on the left side of Eq. (12); when the FVM is applied to obtain the intensities in Fig. 4a, these problems are totally avoided.

It will be immediately recognized that the mapping just presented can be used for any number of intensity components. Furthermore, the intensity distribution will usually be symmetric as well (in Fig. 4a $I(r, \varphi_e, z, \theta, \varphi_r = 0) = I(r, -\varphi_e, z, \theta, \varphi_r = 0)$) so only the intensities for $y \geq 0$ need be calculated.

Solution Procedure

To solve an axisymmetric radiation problem in the cylinder in Fig. 2, the last section

showed that it is sufficient to solve for the intensity component $I(r, \varphi_\sigma, z, \theta, \varphi_r = 0)$. The spatial control volume P is bounded by r_{p-}, r_{p+}, $\varphi_{\sigma p-}$, $\varphi_{\sigma p+}$, z_{p-}, z_{p+}. The discrete solid angle covers the range shown in Fig. 2c (θ^{j-} to θ^{j+} and $-\Delta\varphi_r/2$ to $+\Delta\varphi_r/2$, where $\Delta\varphi_r = \Delta\varphi_\sigma = \varphi_{\sigma p+} - \varphi_{\sigma p-}$). Following the discretization procedure outlined earlier, an algebraic equation is written for the intensity in each direction I at each node. Each nodal intensity depends only on upstream nodal intensities.

For $\theta < \frac{\pi}{2}$, the solution is marched from the outer wall to the centre of segment 1 in Fig. 2a for each z level beginning at the bottom and ending at the top (maximum z). The boundary condition along the symmetry surface (y = 0 in Fig. 2a) is $Q^I = 0$ because the computed intensities transport no heat across this surface. The solution in the adjacent segment is likewise found, and the process is repeated for all segments in the Quadrant I ($\frac{\pi}{2} \le \varphi_\sigma \le \pi$).

The solution in Quadrant II is similar except the sweep is from the centre towards the outer wall in order to keep the marching direction the same as S^I. When all nodal values have been updated, a new solution for intensity has been created for one angle θ^j. The process is repeated for each θ^j, being careful to reverse the sweep direction in the z-direction for $\theta > \pi/2$.

The nodal intensities just obtained constitute the desired solution if the enclosure walls are black, the medium temperature is known, and there is no scattering. Otherwise these

intensities are used to update the radiant flux leaving the wall, the medium temperature and the scattering. The solution for updated intensities is embedded in an outer iteration loop that is repeated until the solution converges.

Methods of updating these variables are described by Raithby and Chui[13]. In the present study the medium temperature is assumed known. The grey-wall boundary conditions and the intensities used in the inscattering calculation were updated at the end of each outer loop.

RESULTS

To evaluate the performance of the FVM, it is desirable to compare its predictions to exact results and the predictions of earlier models. Most of the results presented here are therefore for "clean", benchmark-type, problems.

Comparisons with Exact Solutions

Enclosure with an absorbing-emitting medium: The first test case involves a cylindrical enclosure (see Fig. 5) containing an absorbing-emitting but non-scattering medium at constant temperature (T_M = 100K). It has a height of z_o = 2m and radius, r_o = 1m. The walls are assumed cold (T_w = 0) and black (ε_w = 1). The objective is to compare the FVM prediction of the total radiant heat transfer on the radial wall, q_r with an exact solution obtained as follows.

In the absence of scattering, the intensity at any location within the cylinder is, from the following solution to Eq. (1),

$$I\,(r, z, \theta, \phi), = I_b\,(1 - e^{-\kappa s}) \qquad (14)$$

where s is the distance upstream to the vessel wall along the ray defined by (θ, ϕ), and

$I_b = (\sigma T_w^4)/\pi$ is the blackbody intensity of the homogeneous medium. To obtain the "exact" radiant flux, q_r, emitted from the gas and falling on the radial wall, the heat flux at each point on the wall was obtained by numerically integrating $I(\vec{s} \cdot \vec{n})$ over all incident solid angles. The dimensionless radiant flux, $q_r^* = q_r/\sigma T_w^4$, from the middle of the cylinder side to the end, is shown in Fig. 5 as solid lines for three optical thicknesses ($\kappa^* = K_a r_c = 0.1, 1.0, 5.0$).

The finite volume solution to this problem at discrete locations along the cylinder side is also plotted in Fig. 5. The prediction was based on a moderately fine grid: 16 control volumes in the r direction ($N_r = 16$), 30 in the z direction ($N_z = 30$), 12 polar angles ($N_\theta = 12$) and 16 azimuthal angles ($N_\phi = 16$); an error of less than 0.2% was obtained for all three optical thicknesses. This accuracy of the FVM is somewhat better than that of the Spherical Harmonic (P_3) Method by Mengüç and Viskanta[6], also shown in Fig. 5 (as dashed lines); their prediction is based on a grid $N_r \times N_z = 21 \times 41$.

The same test problem was used to study the reduction in the discretization error with grid refinement for the present method. Figure 6 displays the error curves for the prediction of the dimensionless total radiant flux $Q_r^* = \left(\int_{z=0}^{1} q_r^* \, dz \right)$ for $\kappa^* = 5$. These curves are generated by varying the components of the spatial and angular grids (i.e. N_r, N_z, N_θ, N_ϕ) one at a time from the mesh $N_r = 16$, $N_z = 30$, $N_\theta = 12$, $N_\phi = 16$ that gives the almost exact total heat flux (error ~ 0.003%). The discretization error is seen to decrease quadratically with the angular refinement (i.e. increased N_θ and N_ϕ). The error reduction with the refinement of the spatial grid is

somewhere between linear and quadratic, as previously anticipated. Typically, the fine grid solutions (error < 0.01%) required a CPU time of 450s on a VAX 11-785 machine, while coarser grid solutions (error ~ 1%), required about 80s.

Enclosures with absorbing-isotropically scattering media: The second benchmark case involves a finite cylindrical enclosure with cold black walls subject to a diffuse radiant emission in from the top circular wall. The enclosed medium is assumed to be homogeneous, absorbing, isotropically scattering, but non-emitting. The analytical formulation for this problem was presented by Crosbie and Farrell[20] and exact solutions at six specific test conditions have been made available by Crosbie[21]. The six test conditions included enclosures of three different sizes with various magnitudes of scattering and absorption coefficients. The accuracy of the FVM has been checked by making comparisons to these solutions for the case $\sigma_s = K_a$ and with $(\sigma_s + K_a)r_c = 1$ and 5.

Space limitations do not permit a graphical presentation of comparisons (see Chui[22]). For a cavity radius to height ratio of 5, the heat fluxes on all surfaces were predicted to within 5% for a coarse mesh ($N_r = 6$, $N_z = 4$, $N_\theta = 8$, $N_\phi = 4$); the CPU time was about 10s on a VAX 11-785. Doubling the grid size sharply reduced the error, and increased CPU time by a factor of 15.

Similar results were found for other cavity aspect ratios. For a tall thin cylinder (radius to height of 0.1) the finite volume reusits on a coarse mesh ($N_r = 4$, $N_z = 12$, $N_\theta = 6$, $N_\phi = 4$) were distinctly better than for the P_3 method[6].

Anisotropic Scattering

The FVM was again applied to a cylindrical geometry, see Fig. 7, but anisotropic scattering was included. The cylinder has height z_o = 1m, radius r_o = 0.4m, and emits diffuse radiation from the top surface at a uniform rate q_w. The walls are cold and black, the medium is cold (non-emitting), and (in all but the baseline case) absorbs K_a = 0.5 m^{-1} and scatters σ_s = 5 m^{-1} anisotropically in accordance with the delta-Eddington phase function (Joseph and Wiscombe[33], Crosbie and Davidson[34]):

$$\Phi(\psi) = 2f\delta(1 - \cos\psi) + (1 - f)(1 + 3g\cos\psi) \qquad (15)$$

where ψ is the angle between the incident and scattered directions. The first term on the right side contains the delta function; f governs the amount of forward scattering, g governs the degree of asymmetry about $\psi = \pm\pi/2$, and there is symmetry about $\psi = 0$. The computational grid used was (N_r x N_z) = (6 x 12) and (N_θ x N_ϕ) = (16 x 12). Predictions of the non-dimensional heat flux distribution on the side wall (Fig. 7a) ~~and on the bottom surface (Fig. 7b)~~ are shown for 5 different scattering conditions. The baseline case of no scattering (square symbols), σ_s = 0, K_a = 0.5 m^{-1} results in ~~high heat flux on the bottom wall (Fig. 7b), and~~ a high heat load, for z ≥ 0.1m, on the radial surface. The other limiting case is isotropic scattering, σ_s = 5 m^{-1}, K_a = 0.5 m^{-1} which results in minimum net heat transfer ~~on the bottom wall, and~~ on the radial surface for z ≥ 0.1m. As f is increased from 0.1 to 0.999, the amount of forward scattering increases, increasing the amount of radiation that reaches the lower regions of the cavity. For f = 0.999, g = 0.0, nearly all scattering is forward so the no-scattering baseline case

should be recovered; the FVM captures the expected behaviour extremely closely on the side wall (Fig. 7) and top wall (not shown), and bottom wall, and with a slight discrepancy on the base wall (Fig. 7b) due to discretization error. For $f = 0.1$ and low asymmetry ($g = 0.25$) the predictions lie, as they should, close to the isotropic limit.

It can be concluded that the model predictions in this test follow correct trends.

Comparison With Measured Furnace Data

The last test involves the application of the method to predict the radiative heat transfer in an International Flame Research Foundation test furnace (see Fig. 8). Experimental radiant flux data along the lateral side of the cylindrical furnace and the temperature of the medium have been obtained by Wu and Fricker[20]. The objective is to predict the net radiant heat transfer in the radial direction, q_r, on the furnace side wall, given the measured temperature data.

The Spherical Harmonic (P_3) method has been applied to this problem by Mengüç and Viskanta[6] and the Discrete Ordinate Method by Fiveland[4], both using $K_a = 0.3m^{-1}$ and $\sigma_s = 0$, and their results are also shown in Fig. 8. Using the same temperature data, similar grid $(N_r x N_z) x (N_\theta x N_\phi) = (3x17)x(8x12)$, and identical K_a and σ_s, the FVM yielded the results shown for comparison on this figure. It is tempting to claim that the present results are slightly better than those from the other models, but the accuracy of the prediction depends on the values of K_a and σ_s used, and their correct values are not known (nor are they constant). Suffice it to claim that the FVM is able to reproduce a physically reasonable radiant flux distribution that follows the trend of the measured data, peaking between z = 1 to 1.5m.

SUMMARY

Application of the finite volume method has been described for problems in which radiant intensity varies over three space dimensions and two angles. In this application, consideration has been restricted to cases with circular-cylinder computational meshes. A special discretization was used that slightly sacrificed accuracy to gain simplicity and economy in solving the radiation transfer equation. The proposed formulation can potentially incorporate any scattering phase function.

It has also been shown that, when the radiation problem is axisymmetric, a special mapping can be used to transform the dependence of intensity on two space coordinates and two angles, to three space coordinates and one angle. In this analysis, the general finite volume method has been specialized to apply to such problems.

Predictions for several axisymmetric benchmark problems, and one furnace problem, show that the present method is quite accurate for coarse grids, that the error decreases rapidly as the grid is refined, and that the solutions are inexpensively obtained.

ACKNOWLEDGEMENTS

This work was supported by a contract from the Combustion and Carbonization Research Laboratory, CANMET, of the Energy Mines and Resources Department of the Canadian Federal Government. Special thanks are extended to Professor K. G. T. Hollands of the Mechanical Engineering Department at the University of Waterloo for his instructive comments and useful suggestions. We also wish to acknowledge the assistance of Professor Crosbie, who supplied publications as well as unpublished results.

REFERENCES

[1]Perlmutter, M. and Howell, J.R. 'Radiant Transfer through a Grey Gas between Concentric Cylinders using Monte Carlo', *Journal of Heat Transfer*, Vol. 86, 1964, pp. 165-179.

[2]Lowes, T.M., Bartelds, H. and Heamp, M.P., Michelfelder, S. and Pai, B.E. 'Prediction of Radiant Heat Flux Distribution', *Heat Transfer in Flames*, N.H. Afgan and J.M. Beer (Eds), Washington DC: Scripta Book Co. 1974, pp. 179-190.

[3]Steward, F.R. and Tennankore, K.N. 'Towards a Finite Difference Solution coupled with the Zone Method for Radiative Transfer for a Cylindrical Combustion Chamber', *Journal of the Institute of Energy*, 1979, pp. 107-114.

[4]Fiveland, W.A. 'A Discrete Ordinates Method for Predicting Radiative Heat Transfer in Axisymmetric Enclosure', *ASME* Paper No. 82-HT-20, 1982.

[5]Fernandes, R. and Francis, J. 'Combined Conductive and Radiative Heat Transfer in an Absorbing, Emitting, and Scattering Cylindrical Medium', *Journal of Heat Transfer*, Vol. 104, 1982, pp. 594-601.

[6]Mengüç, M.P. and Viskanta, R. 'Radiative Transfer in Axisymmetric, Finite Cylindrical Enclosures', *ASME Journal of Heat Transfer*, Vol. 108, 1986, pp. 271-276.

[7]Jamaluddin, A.S. and Smith, P.J. 'Predicting Radiative Transfer in Axisymmetric Cylindrical Enclosures using the Discrete Ordinates Method', *Combust. Sci. and Tech.*, Vol. 62, 1988, pp. 173-186.

[8]Yucel, A. and Williams, M.L. 'Interaction of Conduction and Radiation in Cylindrical Geometry with Azimuthal Symmetry', ASME, HTD-Vol. 96, pp. 281-289, Proc. of 1988 National Heat Transfer Conference, Houston, Texas.

[9]Carvalho, M.G., Farias, T., and Fontes, P. 'Predicting Radiative Heat Transfer in Absorbing, Emitting, and Scattering Media using the Discrete Transfer Method, ASME, HTD-Vol. 160, pp. 17-26, Proc. of 1991 National Heat Transfer Conference, Minneapolis.

[10]Howell, J.R. 'Thermal Radiation in Participating Media: The Past, the Present, and Some Possible Futures', *Journal of Heat Transfer*, Vol. 110, 1988, pp. 1220-1226.

[11]Viskanta, R. and Mengüç, M.P. 'Radiation Heat Transfer in Combustion Systems', *Progress in Energy and Combustion Science*, Vol. 13, No. 2, 1987, pp. 97-160.

[12]Carlson, B.G. and Lathrop, K.D. 'Transport Theory - the Method of Discrete Ordinates', *Computing Methods in Reactor Physics*, edited by Greenspan *et al.*, Gordon and Breach, New York, 1968, pp.171.

[13]Raithby, G.D. and Chui, E.H. 'A Finite-Volume Method for Predicting Radiant Heat Transfer in Enclosures with Participating Media', *Journal of Heat Transfer*, Vol. 112, 1990, pp.415-423.

[14]Fiveland, W. 'Three-Dimensional Radiative Heat Transfer Solutions by the Discrete-Ordinate Method', AIAA J. Thermophysics, Vol. 2, No. 4, 1988, pp. 309-316.

[15]Lathrop, K.D., 'Remedies for Ray Effects', *Nuclear Science and Engineering*, Vol. 45, 1971, pp. 255-268.

[16]Siegel, R. and Howell, J.R. 'Thermal Radiation Heat Transfer', Second Edition, McGraw Hill, New York, London, 1981, pp. 437-438.

[17]Huebner, K.H. 'The Finite Element Method for Engineers', John Wiley & Sons, Inc., 1975.

[18]Pomraning, G.C. 'The Equations of Radiation Hydrodynamics', Pergamon, Oxford, 1973, pp. 84.

[19]Carlson, B.G., and Lathrop, K.D. 'Transport Theory - The Method of Discrete Ordinates', *Computing Methods in Reactor Physics*, edited by Greenspan et al., Gordon and Breach, New York, 1968, pp. 183-184.

[20]Crosbie, A.L. and Farrell, J.B. 'Exact Formulation of Multiple Scattering in a Three-Dimensional Cylindrical Geometry', *J. Quant. Spectrosc. Radiat. Transfer*, Vol. 31, No.5, 1984, pp. 397-416.

*[21]Crosbie, A.L. Department of Mechanical and Aerospace Engineering, University of Missouri-Rolla, Rolla, Missouri, U.S.A., private communication, 1989.

[22]Chui, E.H. 'Modelling of Radiative Heat Transfer in Participating Media by the Finite Volume Method', Ph.D. thesis, Department of Mechanical Engineering, University of Waterloo, Waterloo, Ontario, Canada, 1990.

[23]Joseph, J.H. and Wiscombe, W.J. 'The Delta-Eddington Approximation for Radiative Heat Transfer', *Journal of Atmospheric Sciences*, Vol. 33, 1976, pp. 2452-2459.

[24]Crosbie, A.L. and Davidson, G.W. 'Dirac-Delta Function Approximations to the Scattering Phase Function', *J. Quant. Spectrosc. Radiat. Transfer*, Vol. 33, No. 4, 1985, pp. 391-409.

[25]Wu, H.L. and Fricker, N. "The Characteristics of Swirl-Stabilized Natural Gas Flames. Part 2: The Behaviour of Swirling Jet Flames in a Narrow Cylindrical Furnace', *Journal of the Institute of Fuel*, 1976, pp. 144-151.

LIST OF FIGURES

Figure 1: Cylindrical coordinates for the equation of radiative transfer.

Figure 2: Schematic of a cylindrical enclosure with a 3D computational grid. Part (a) shows the top view, and part (b) the side view.

Figure 3: A typical control volume in a cylindrical enclosure with P located at the centre. Part (a) shows area A_f and intensity I_f^l on one discrete surface panel and integration points f = 1,2,3. Part (b) shows molecule of nodal points adjacent to node P.

Figure 4: Part (a) shows the intensities in direction $\phi_l = 0$ at 8 locations equidistant from the axis of the cylinder. The angular distribution of the intensity field at location 1 appears in part (b).

Figure 5: Nondimensional radiant heat transfer on the side wall of a cylindrical enclosure containing an absorbing emitting, but non-scattering, gas at uniform temperature T_m with zero wall temperature for 3 optical thickness $\kappa^* = K_a l_o = 0.1, 1.0, 5.0$.

Figure 6: Reduction in the error of total radiant heat transfer to the side of the cylindrical enclosure with spatial refinement (left side) and angle refinement (right side).

Figure 7: Nondimensional radiant heat transfer on the radial walls of a cylindrical enclosure with a diffuse radiant flux q_{in} on the top wall for a scattering medium. The base case 1 has no scattering $\sigma_s = 0$, $K_a = 0.5m^{-1}$. Cases 2 to 5 incorporate 4 different scattering phase functions, all with $\sigma_s = 5m^{-1}$ and $K_a = 0.5m^{-1}$.

Figure 8: Comparison of local radiant fluxes at the side wall of a cylindrical furnace obtained from the Finite Volume Method, P_1 approximation (Mengüç et al[9]) and S_4 method (Fiveland[6]) with experimental data (Wu et al[10]).

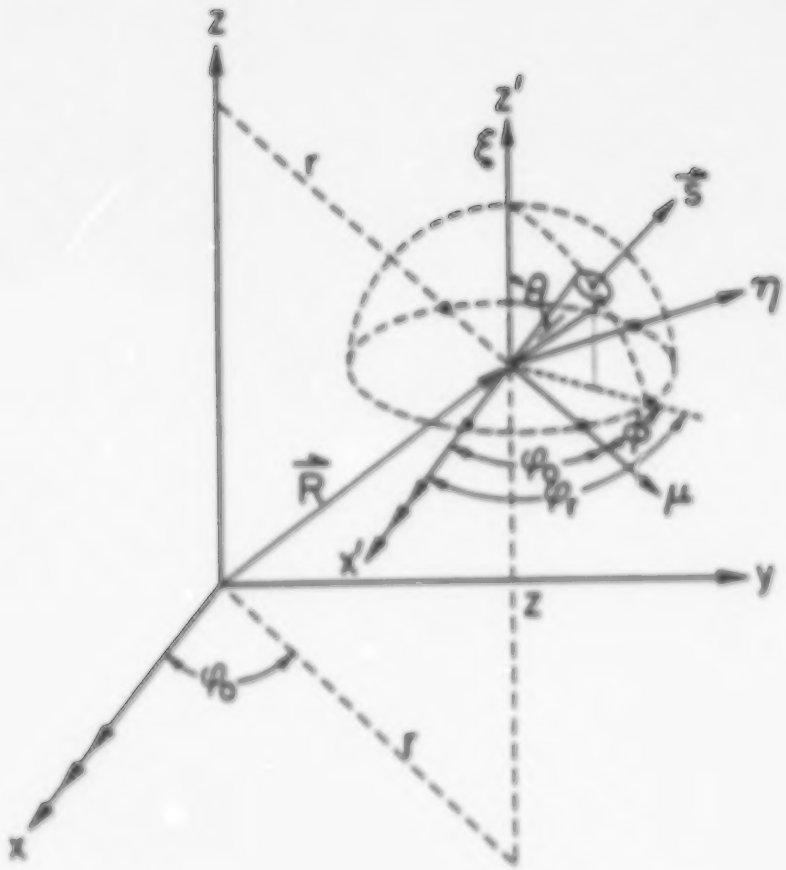

Figure 1: Cylindrical coordinates for the equation of radiative transfer.

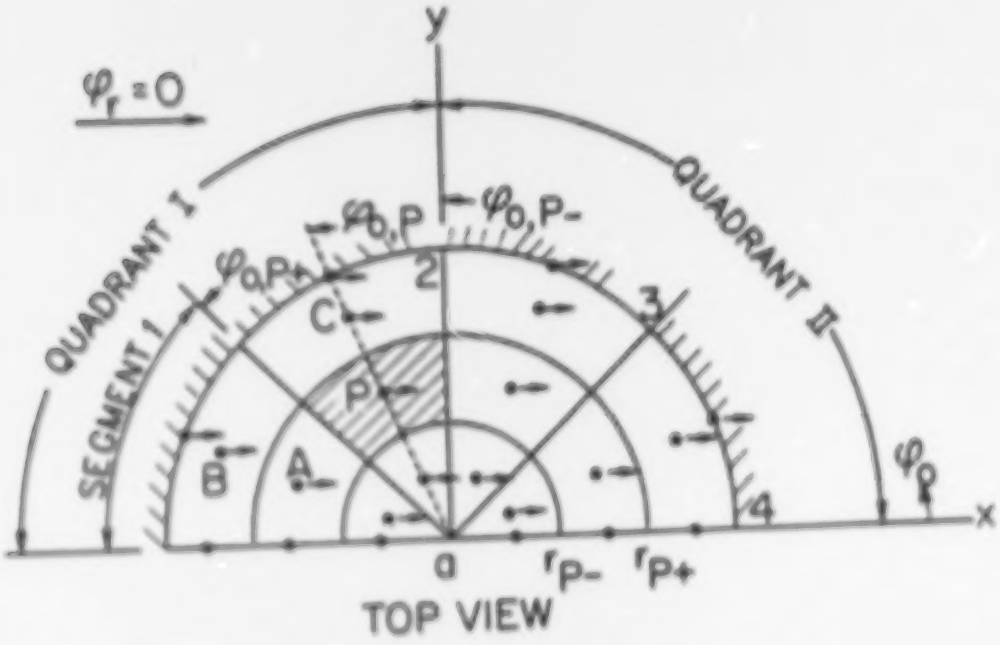

(a)

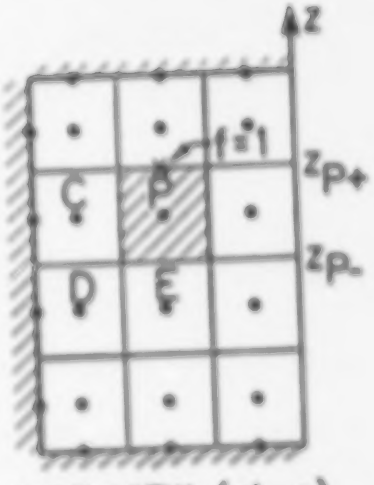

(b)

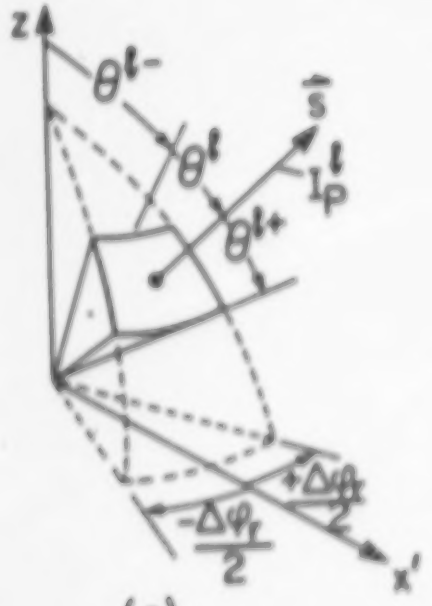

(c)

Figure 2: Schematic of a cylindrical enclosure with a 3D computational grid. Part (a) shows the top view, and part (b) the side view.

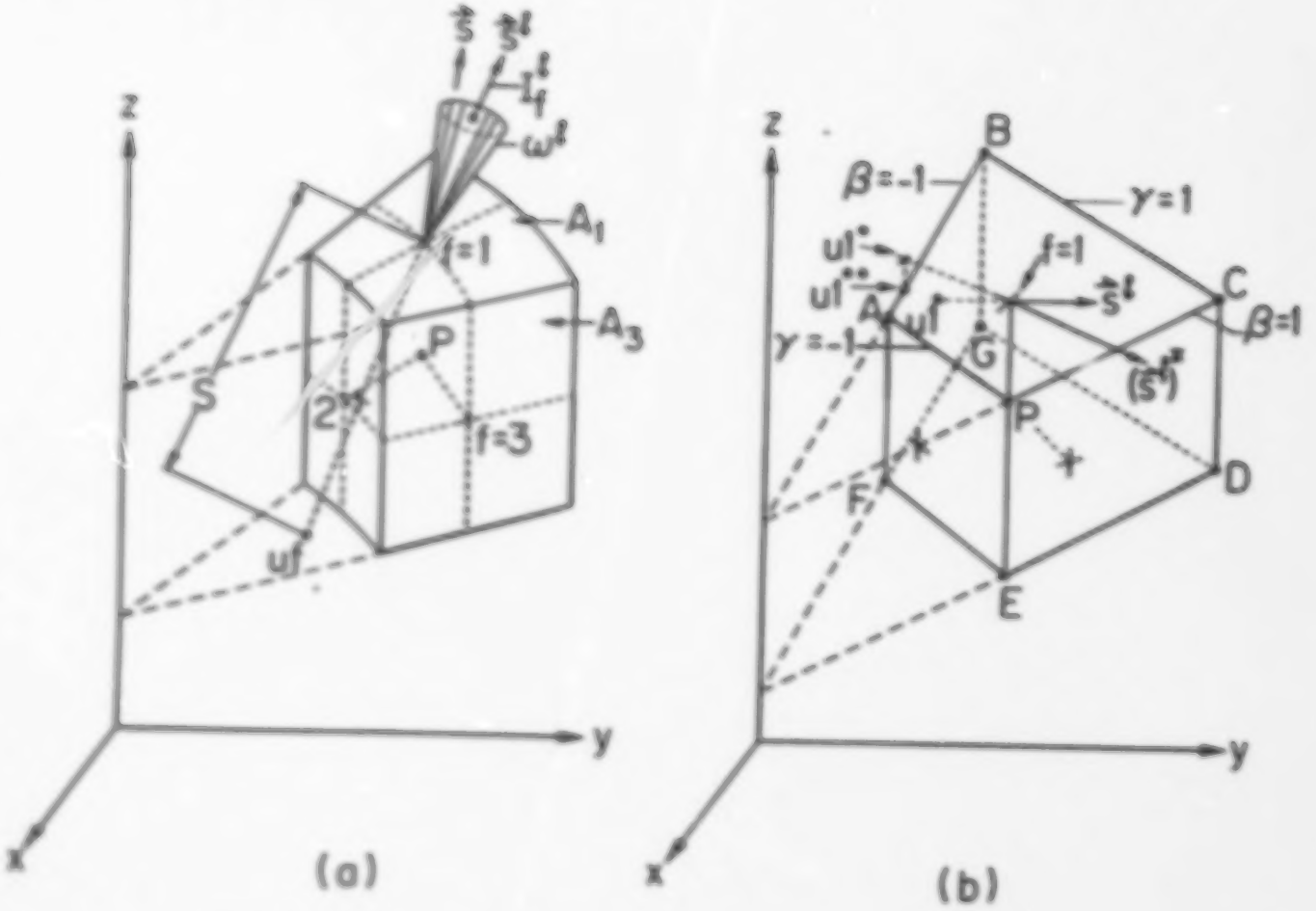

Figure 3: A typical control volume in a cylindrical enclosure with P located at the centre. Part (a) shows area A_f and intensity I_f^l on one discrete surface panel and integration points $f = 1,2,3$. Part (b) shows molecule of nodal points adjacent to node P.

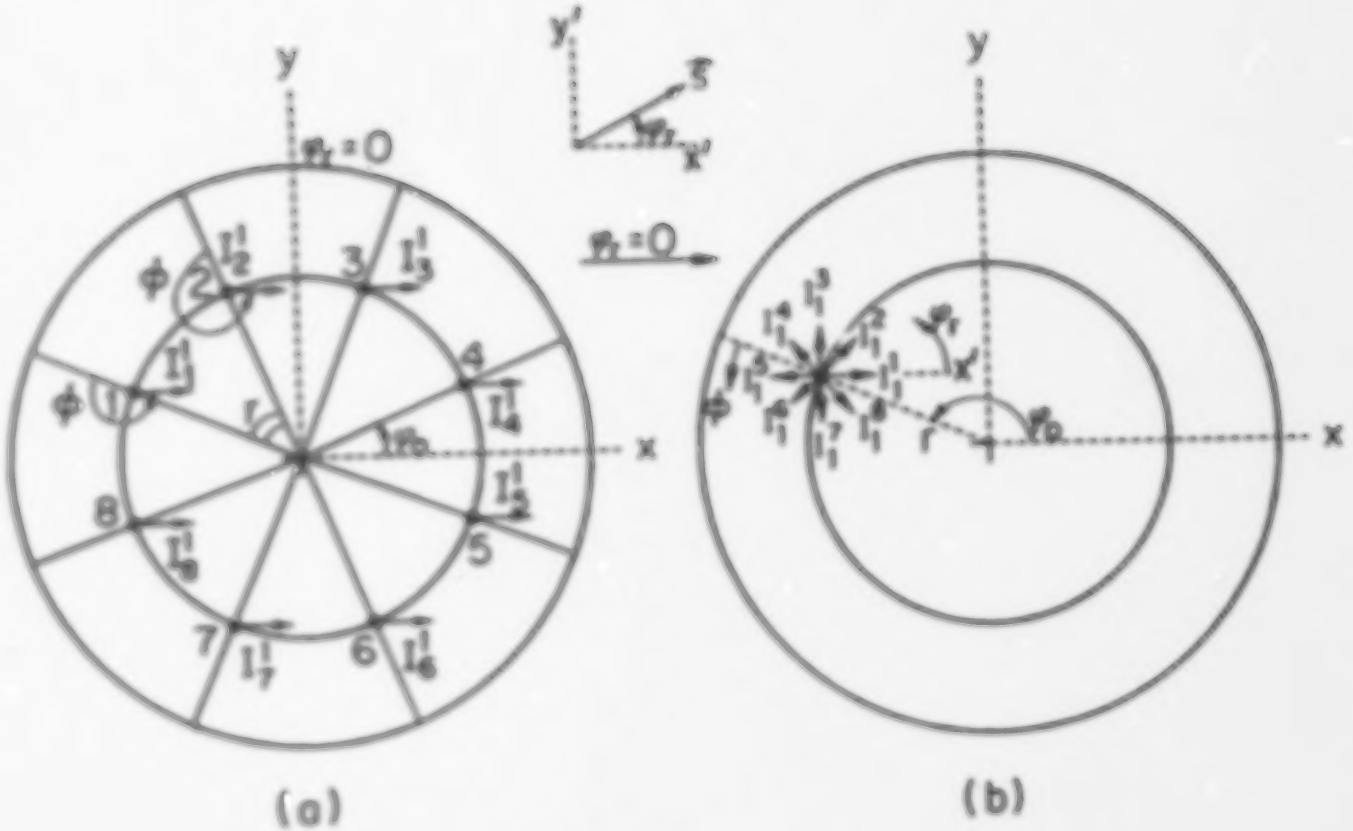

Figure 4: Part (a) shows the intensities in direction $\varphi_1 = 0$ at 8 locations equidistant from the axis of the cylinder. The angular distribution of the intensity field at location 1 appears in part (b).

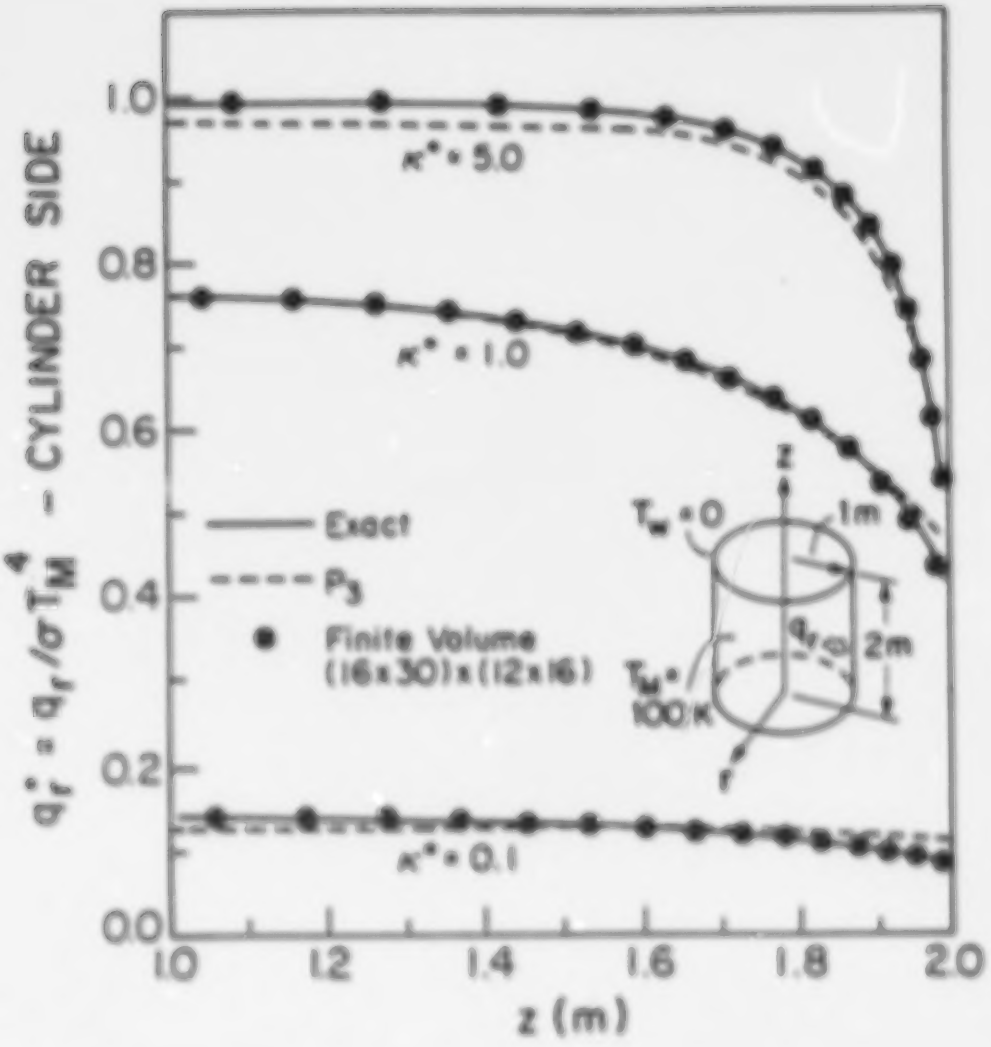

Figure 1: Nondimensional radiant heat transfer on the side wall of a cylindrical enclosure containing an absorbing emitting, but non-scattering, gas at uniform temperature T_M with zero wall temperature for 3 optical thickness $\kappa^* = K_a r_0 = 0.1, 1.0, 5.0$.

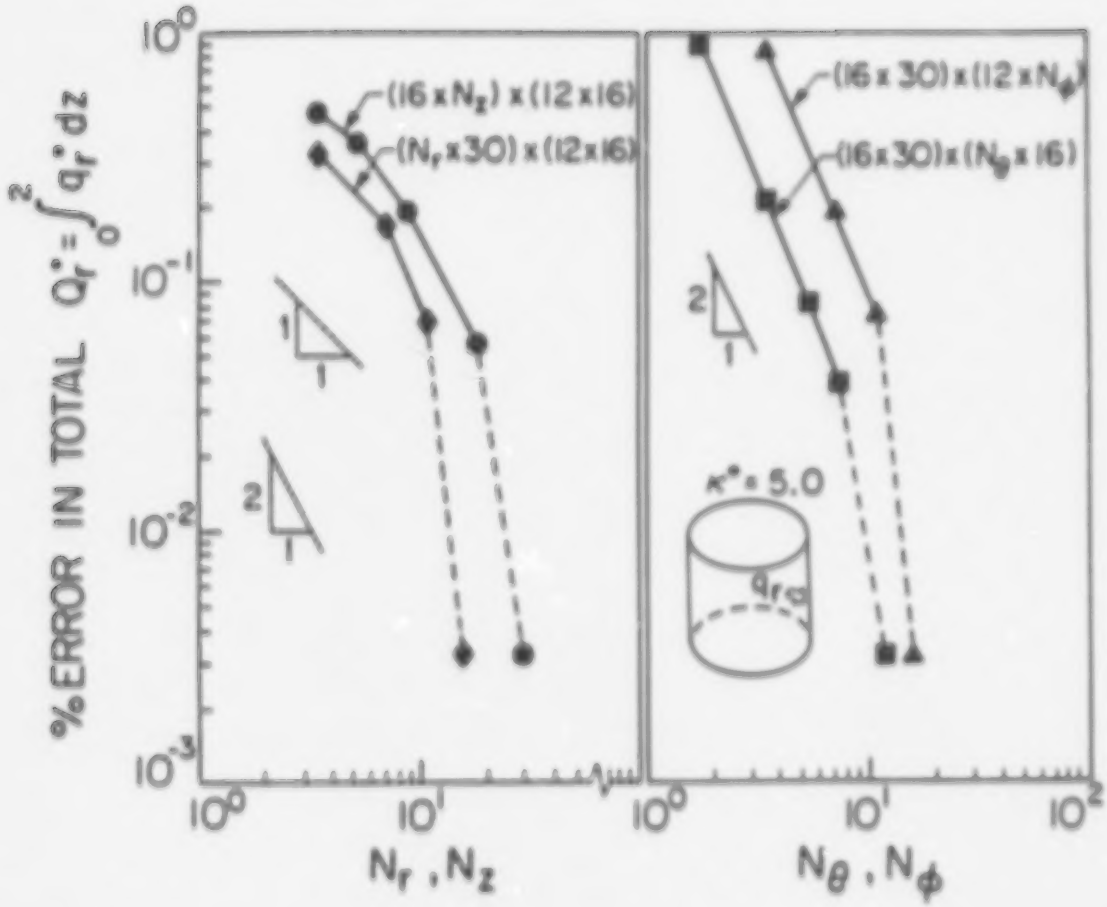

Figure 6: Reduction in the error of total radiant heat transfer to the side of the cylindrical enclosure with spatial refinement (left side) and angle refinement (right side).

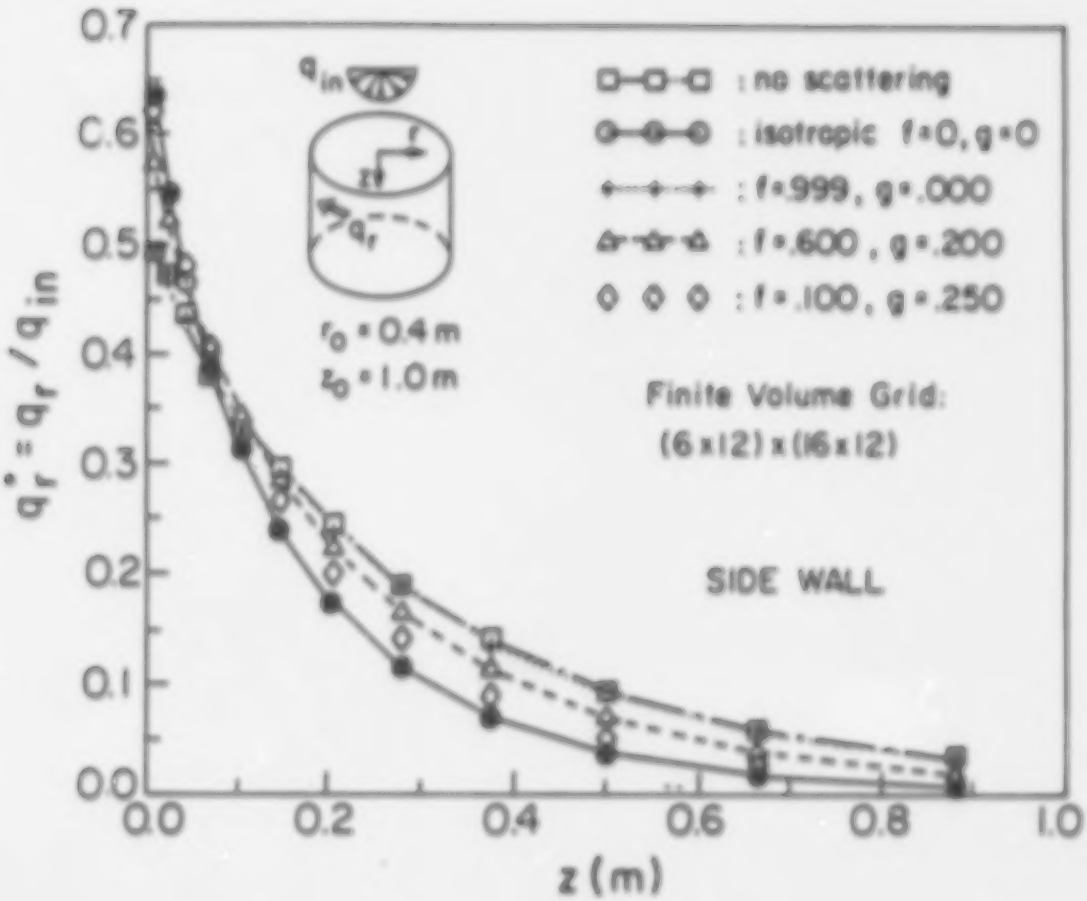

Figure 7: Nondimensional radiant heat transfer on the wall of a cylindrical enclosure with a diffuse radiant flux q_{in} on the top wall for a scattering medium. The base case has no scattering $\sigma_s = 0$, $K_a = 0.5m^{-1}$. Cases 2 to 5 incorporate 4 different scattering phase functions, all with $\sigma_s = 5m^{-1}$ and $K_a = 0.5m^{-1}$.

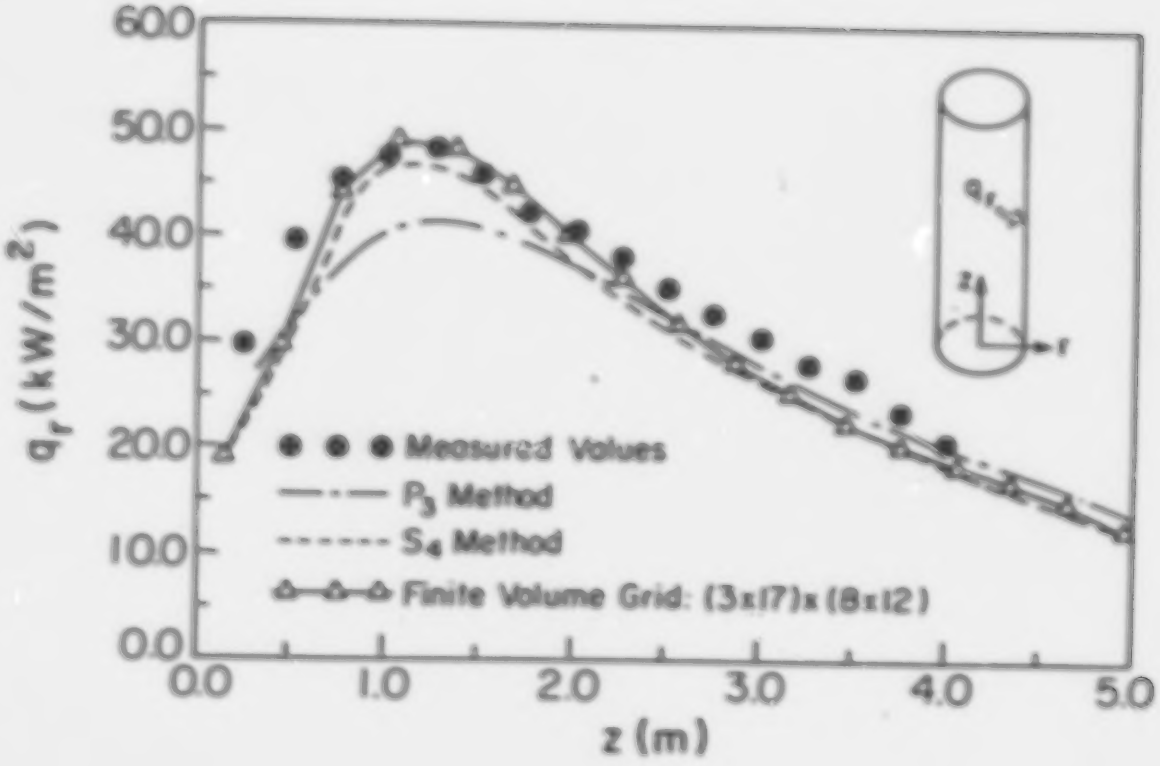

Figure 8: Comparison of local radiant fluxes at the side wall of a cylindrical furnace obtained from the Finite Volume Method, P_3 approximation (Menguç et al[6]) and S_4 method (Fiveland[5]) with experimental data (Wu et al[10]).

12 Appendix D - Implicit Solution Method to Improve Convergence Rate in Radiative Heat Transfer Problems

Paper in press
J. Numerical Heat Transfer

An Implicit Solution Scheme to Improve Convergence Rate in Radiative Transfer Problems

by

E.H. Chui and G.D. Raithby

Department of Mechanical Engineering
University of Waterloo, Waterloo, Ont., Canada N2L 3G1

1 Introduction

Radiative heat transfer within a participating medium is governed by the absorptive, emissive and scattering characteristics of the medium. Since emission depends on the medium temperature and inscattering is a function of the radiant intensities from all incoming directions, the equation for radiant intensity in a given direction depends on both the temperature and complete radiation fields. In many engineering systems (like furnaces and boilers), the temperature field within the solution domain is unknown so that a simultaneous solution of the Radiative Transfer Equation (RTE) and the thermal energy equation is required.

The RTE is usually solved, to obtain radiant intensities, by estimating the emission and inscattering terms respectively from a previously obtained temperature and intensity field. The new intensities are then used to update the temperature and inscattering terms, and the cycle is repeated until convergence is achieved. Such an iterative solution method is referred to here as "explicit". Raithby and Chui [1] observed that convergence of this explicit method was very fast for small optical thickness but, as scattering and absorption became important, the number of iterations rose sharply. Viskanta and Mengü, [2] reported similar slow convergence of the Discrete Ordinates Method for large optical thickness for explicit solutions, and it seems likely that other methods are subject to the same limitation. Lewis et al [3] presented acceleration methods for the Discrete Ordinates Method, but the issue has not been generally resolved.

The aim of this paper is to identify the factors that lead to poor convergence behaviour with the explicit solution procedure, and to introduce a new "implicit" solution that ensures satisfactory convergence behaviour.

The new implicit method will be demonstrated using the Finite Volume Method (FVM) of Raithby and Chui [1], applied to two-dimensional (2D) radiation problems in rectangular enclosures. The theory and algorithms on which the new method is based are, however, believed to be applicable to other solution methods and to geometrically more challenging problems.

2 Governing Equation

The basis for quantitative studies of radiative heat transfer is the radiative transfer equation. Assuming a gray medium, the RTE has the form (see Siegel and Howell, [4]):

$$\frac{dI(\vec{r},\vec{s})}{ds} = -(K_a + \sigma_s)I(\vec{r},\vec{s}) + K_a I_b(\vec{r}) + \sigma_s \bar{I}(\vec{r},\vec{s}) \tag{1}$$

This equation describes the increase in radiant intensity $I(\vec{r},\vec{s})$ at spatial location $\vec{r}$ over the path length ds in the direction of unit vector $\vec{s}$, as shown in Fig. 1a. The terms on the right-hand-side represent respectively the decrease in intensity due to absorption and outscattering, and the increase through emission and inscattering, where K_a and σ_s are the absorption and scattering coefficients respectively. The inscattering term is defined by

$$\sigma_s \bar{I}(\vec{r},\vec{s}) = \frac{\sigma_s}{4\pi} \int_{4\pi} I(\vec{r},\vec{s}')\Phi(\vec{s},\vec{s}')d\omega' \tag{2}$$

where the fraction of the intensity $I(\vec{r},\vec{s}')$ in direction $\vec{s}'$ (see Fig. 1a) that is scattered into direction $\vec{s}$ is defined by the phase function $\Phi(\vec{s},\vec{s}')$.

3 Finite Volume Solution of the RTE

3.1 Review of Finite Volume Method

Equation (1) expresses the conservation of radiant energy in direction $\vec{s}$ over an infinitesimal control volume. The FVM yields an approximate (discrete) solution to this equation which converges to the solution of Eq. (1) as the computational grid is refined.

To implement the method, the space within the computational domain is subdivided into volumes, such as those shown in Fig. 1b, and direction is subdivided into discrete solid angles, like ω^l in Fig. 1a. The intensity within the volume centered at P and within ω^l is represented by a single value, I_P^l. The equation for I_P^l is the RTE integrated over the volume V_P and over ω^l.

The control volumes in Fig. 1b have unit depth in the z direction, the interior nodes lie at the geometric center of their control volumes, each control volume surface is divided into 2 panels (Fig. 2a), and integration points $f = 1, 2, \ldots 8$ lie at the center of each panel. The radiant energy Q_f^l that lies within ω^l and that crosses the surface panel f of area A_f is approximated by

$$Q_f^l = I_f^l A_f \int_{\omega^l} \vec{s} \cdot \vec{a}_f d\omega \quad = I_f^l A_f D_f^l \tag{3}$$

where $\vec{n}$ is the outward unit surface normal, and where I_f^l and $\vec{n}_f$ at point f have been used to approximate their values over A_f. The D_f^l integral is analytically evaluated.

The integral of the RTE over volume P and over ω^l simply asserts that the net radiant energy within ω^l that leaves through the control volume surfaces must equal the emission and inscattering minus the absorption and outscatting for this ω^l within the volume:

$$\sum_{f=1}^{6} Q_f^l = \sum_{f=1}^{6} I_f^l A_f D_f^l = [-(K_{a,P} + \sigma_{s,P}) I_P^l + K_{a,P} I_{b,P} + \sigma_{s,P} \bar{I}_P^l] \omega^l V_P \qquad (4)$$

where intensities and properties within V_P have been approximated by their values at node P.

Equation 4 can not be solved for I_P^l until the integration point intensities I_f^l are related to the nodal intensities. As the first step in providing the closure, I_f^l is approximated (see Raithby and Chui [1]) by:

$$I_f^l = \underbrace{I_{uf}^l e^{-\alpha_f S}}_{T1} + \underbrace{R_f^l \left(1 - e^{-\alpha_f S}\right) - \frac{1}{\alpha_f} \left(\frac{\partial R^l}{\partial s}\right)_f \left[1 - e^{-\alpha_f S}(1 + \alpha_f S)\right]}_{T2} \qquad (5)$$

This equation is a solution to the RTE (Eq. 1) between point uf and point f in Fig. 2a. Term $T1$ is the transmitted intensity. Term $T2$ results from retaining two terms of a Taylor series expansion about point f of the emission and inscattering terms in Eq. (1). The extinction coefficient α and variable R^l are defined by:

$$\alpha = K_a + \sigma_s \qquad\qquad R^l = \frac{K_a I_b + \sigma_s \bar{I}^l}{\alpha} \qquad (6)$$

To complete the closure, I_{uf}^l is found by interpolation (e.g. interpolation between W and P in Fig. 2a), and R_f^l and $(\partial R^l/\partial s)_f$ are found by linear interpolation using values of R^l stored at the nodes. Substitution of the I_f^l expressions from Eq. (5) into Eq. (4) results in an expression involving nodal values alone.

Certain additional approximations were introduced in the present study to simplify the algebra. These neither reduce the formal order of accuracy of the scheme, nor affect the property that the method reduces exactly to the diffusion limit for a strongly participating medium. The first approximation is that the value of R^l at the two integration points on a control volume face are taken to be the same; for example, in Fig. 2a, $R_1^l = R_2^l = R_w^l$. The second approximation is that the derivatives of R^l at the two integration points on each face are the same, that the contributions of

the derivatives parallel to the face are ignored, and that the derivative normal to the face is obtained using the two nearest nodal values in the normal direction (e.g., $(\partial R^i/\partial y)_w$ is found from R^i_W and R^i_P).

A few comments on the treatment of the inscattering term, $\bar{I}^i_p$ in Eq. (4) are in order because the current recommended procedure is somewhat different than that given by Raithby and Chui [1]. $\bar{I}^i_p$ results from the integration of Eq. (2) over ω^i (see Fig. 1a), so that

$$\bar{I}^i_p = \frac{1}{4\pi} \sum_{j}^{m} I^j_p \hat{\Phi} \tag{7}$$

where

$$\hat{\Phi} = \frac{\int_{\omega^i} \int_{\omega^j} \Phi(\hat{r}, \hat{s}) d\omega^j d\omega^i}{\omega^i} \tag{8}$$

The value of $\hat{\Phi}$ is obtained by exact, or very accurate numerical, integration of the phase function. This formulation was discussed and demonstrated tested by Chui et al. [3].

3.2 Final Form of the Approximate RTE

Substitution of the closure relations into Eq. (4) results in an algebraic equation relating I^i_p to the intensity at the eight neighbour nodes in Fig. 1b. This equation has the form

$$a^i_p I^i_p = \sum_{nb} a^i_{nb} I^i_{nb} + b^i_p \tag{9}$$

where the subscript nb refers to the neighbour points, and the summation is over the eight neighbours. Some of the coefficients a^i_{nb} may be zero. All the R^i terms from Eq. (5) applied at each integration point are grouped in the source term, b^i_p.

By slightly sacrificing accuracy in the interpolation for the af-values shown in Fig. 2b, the equation for I^i_p can be made to depend only on the "upstream" nodal values (see Raithby and Chui [1]). For the δ^i direction in Fig. 2a, Eq. (9) takes the form

$$a^i_p I^i_p = a^i_W I^i_W + a^i_S I^i_S + a^i_{SW} I^i_{SW} + b^i_p \tag{10}$$

Equation (9 - 10) for each node together with boundary conditions provides the equation set for the nodal intensities in direction δ^i.

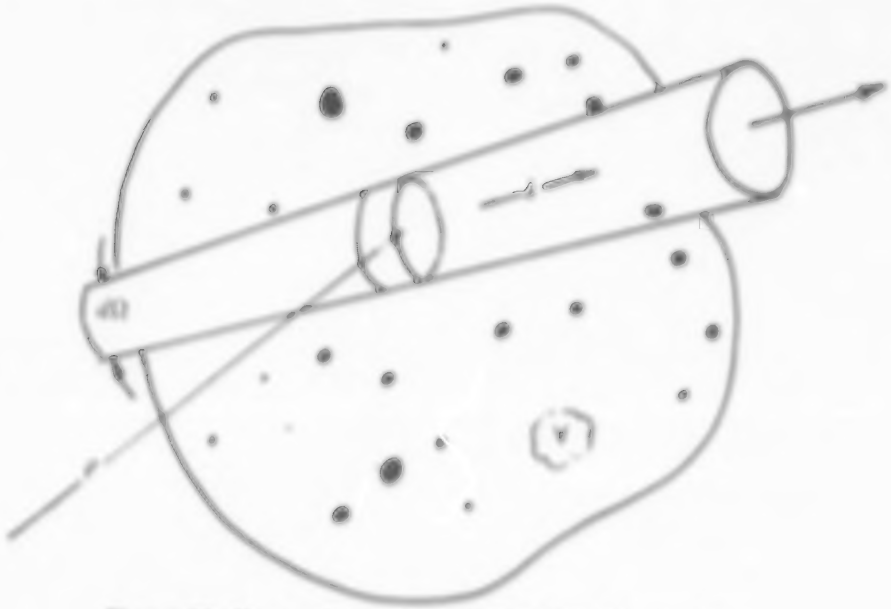

Figure 22: Nomenclature for radiation transfer equation.

The first term on the RHS of Eq. (157) is the net addition to the intensity due to emission minus absorption by the gas, as in Eq. (99). In the second term $\sigma_{s,g}i$ is the outscattering by the gas while $\sigma_{s,g}\hat{i}$ is the gas inscattering contribution. The third term is the contribution to i due to the excess of particle emission over particle absorption; these contributions come from Eqs. (121) and (125) respectively. In the fourth term on the RHS, $\beta^p K^s_{pi}$ decreases i by particle outscattering and $\beta^p K^s_{pj} i_p$ increases i through particle inscattering; these contributions were derived in Chapter 6, Eqs. (132) and (136). The scattering phase functions that appear in Eqs. (158) and (159) are Φ for the gas and Φ_p for the particles. These will be usually quite different.

7.3 Integral Equation for Intensity

The intensity i depends on position $\vec{r}$ and direction $\hat{s}$. Since $\vec{r}$ is specified by three co-ordinates and $\hat{s}$ by two angles, i is a five-dimensional variable. In keeping with the usual finite volume procedure, space is subdivided into discrete volumes. As an obvious extension to this method, direction is subdivided into discrete solid angles. A discrete volume surrounding a node K is designated as $\forall_K$ and a discrete solid angle by Ω^m. The sum of all such volumes completely fills the computation domain without overlap. Similarly, all discrete angles span 4π steradians without overlap. As the starting point for discretization, Eq. (157) must be integrated over $\forall_K$ and

Ω^m.

The left-hand side of Eq. (157) can be written without approximation as

$$\int_{\forall_k} \frac{di}{ds} d\forall = \int_{\forall_k} \hat{s} \cdot \nabla i \, d\forall = \int_{\forall_k} \nabla \cdot (i\hat{s}) d\forall = \int_{S_k} i\hat{s} \cdot \hat{n} ds \tag{160}$$

The second equality is valid because $\hat{s}$ is independent of position. The third equality follows from the divergence theorem, Eq. (179). S_k is the outer surface area of the volume $\forall_k$, and $\hat{n}$ is the unit vector normal to S_k, as shown in Fig. 23. Each term in Eq. (160) represents the net flux of radiant energy out through the surface S_k per unit solid angle. Integrating each term in Eq. (157) over $\forall_k$ and over Ω^m yields the following integral equation

$$\begin{aligned} \int_{S_k} \int_{\Omega^m} i\hat{s} \cdot \hat{n} d\Omega ds \;=\; & \int_{\forall_k} \int_{\Omega^m} (K_{\alpha,\beta}(i_{b\beta} - i) - \sigma_{s,\beta}(i - \bar{i}) \\ & + \sigma_{s,\beta} K^*_{p\beta}(i^p_{s,\beta} - i) - \beta^p K^*_{p\beta}(i - i_{p\beta})) d\Omega d\forall \end{aligned} \tag{161}$$

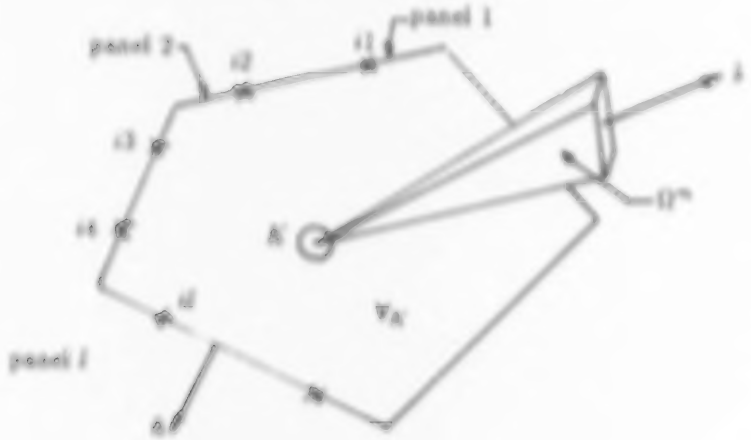

Figure 23. Discrete volume $\forall_K$ surrounding node K, and discrete solid angle Ω^m.

7.4 First Level of Discretization of the Intensity Equation

Equation (161) contains no discretization approximations. To solve this equation each term is eventually replaced by an algebraic equation that contains known quan-

tities and nodal variables. As the first step, the surface of $\forall_k$ is divided into panels $l = 1, 2, \ldots, L$ and and "integration point" ql is located at the center of panel l. The area of panel l is S_l, the total radiant energy crossing panel l within solid angle Ω^m is approximated as follows

$$Q_l^m = \int_{S_l} \int_{\Omega^m} \mathrm{id} \cdot \mathrm{n} d\Omega dA \approx \overline{\mathrm{id}}^{ql} S_l \int_{\Omega^m} \mathrm{s} \cdot \mathrm{n}_{ql} d\Omega = \overline{\mathrm{id}}^{ql} S_l \Omega_l^m \tag{162}$$

The first approximation is that i is taken as constant over the solid angle Ω^m and over the area S_l, and that the normal over S_l is approximated by the normal at integration point ql. The integral of the direction cosine over Ω^m, *i.e.* Ω_l^m, should be calculated exactly.

Approximating the volume integral of all terms on the RHS of Eq. (161) by the nodal point value, and again taking intensity as constant over Ω^m, the first level approximation of Eq. (161) is

$$\begin{aligned}
\sum_{l=1}^{L} Q_l^m &= \sum_{l=1}^{L} \overline{\mathrm{id}}^{ql} S_l \Omega_l^m \\
&= (\overline{K}_{x,k,k}(i_{up,k} - i_k^m) - \sigma_{t,k}(i_k^m - (i)_k^m) \\
&+ i_{p,k}^m \overline{K}_{p,k}(i_{up,k}^m - i_k^m) - \beta_k^m \overline{K}_{p,k}(i_k^m - (i_p)_k^m))\Omega^m \forall_k
\end{aligned} \tag{163}$$

The incattering term for the gas is

$$(i)_k^m = \frac{1}{4\pi} \sum_{m'} i_k^{m'} \Phi(\Omega^{m'}, \Omega^m) \tag{164}$$

where

$$\Phi(\Omega^{m'}, \Omega^m) = \frac{1}{\Omega^m \Omega^{m'}} \int_{\Omega^m} \int_{\Omega^{m'}} \Phi(s', s) \mathrm{n} s' d\Omega \tag{165}$$

A similar equation holds for incattering by the the particles. To conserve scattered energy, it is extremely important that double integral in Eq. (165), and the similar one for particle incattering, be evaluated to high accuracy.

To close Eq. (163), the intensity at each integration point must be approximated in terms of nodal intensities. In the closure scheme proposed by Raithby and Chui (1990) an intensity i_{up}, that lies upstream of i_{ql}, is found by interpolation of nodal values. To relate i_{ql} to i_{up}, Eq. (157) is rewritten as follows:

$$\frac{dI}{ds} + \kappa I = \kappa B \tag{166}$$

where

$$\kappa = K_{a,g} + \sigma_{s,g} + \epsilon^p_p K^-_p + \beta^p K^-_p \tag{167}$$

$$B = (K_{a,g} i_b + \sigma_{s,g} i + \epsilon^p K^-_p i^p_p + \beta^p K^-_p i^p_p)/\kappa \tag{168}$$

The only difference between this equation and the equation described in Appendix B is that κ and B are redefined by Eqs. (167) and (168) to include the effect of particles.

In fact, from this point the derivation and application of the FVM follows exactly that given in Appendices B to E. Inclusion of the effects of particle scattering therefore should cause no significant difficulty.

7.5 Internal Energy Source Terms due to Radiation

The conversion of internal energy of the gas within volume V into radiant energy, Q^R_G in Eq. (58), is just the excess of emission by the gas over gas absorption.

$$Q^R_G = \int_V \int_{4\pi} K_{a,g}(i_b - i) d\Omega dV \approx K_{a,g}(i_b - < i >) 4\pi V \tag{169}$$

where $< i >$ is the direction average defined by Eq. (111).

The net radiation from a given particle of radius r_p and temperature T_p for a gray diffuse particle is

$$Q^R_p = \epsilon_p (\pi i_{b,p}(T_p) - \pi < i >) 4\pi r_p^2 \tag{170}$$

where the emission is given by Eq. (113) and the absorption is obtained by integrating Eq. (69).

Both Q^R_G and Q^R_p can be found once the values of i are known.

8 CLOSING COMMENTS

This report has provided a detailed derivation of the equations of motion for the particles and gas in a reacting flow. The integral equations serve as a useful starting point for the creation of discrete finite volume models. In the present derivation, the boundaries of the integral volume are allowed to change with time, because many applications are best solved using a moving computational mesh. By providing detailed derivations, all the approximations that are required to reach the 'standard' set of equations are clearly spelled out. Furthermore, many models reported in the literature use incorrect equations as their starting point; the errors usually arise from incorrectly accounting for the transfer of mass of the particles to, or from, the gas phase. Besides (hopefully) providing the correct equations, and listing the approximations, this report brings together in one source the complete equations of motion (volume, mass, momentum, thermal energy, and radiant energy equations).

As already mentioned in the Introduction, this report represents only a fraction of the total effort under the contract. Almost 60% of the total contract effort was undertaken under sub-contract to Imperial College. Their task was to further develop and test the coal combustion model that CANMET had helped fund. The focus of this work was prediction of combustion of low volatile coals. Their final report on this work will appear separately.

The remainder of the work by Thermal Science Ltd. is not described in any reports. This work was focussed on fully acquiring the technology that resides in the Lockwood codes. The literature has been reviewed, the *FAFNIR* code has been connected, and several cold and reacting flow predictions have been made. As an indicator that this technology now *truly* resides in Canada, the models used in the Lockwood codes are now being created in TASCflow, a three-dimensional commercial code written by Advanced Scientific Computing Ltd. in Waterloo, Ontario. Also, new technology created by Thermal Science Ltd., under the partial support of this contract, has now been inserted into PCFlame, a code owned by, and for license from, CANMET. This new model has resulted in dramatic improvements in the furnace wall temperature predictions in the near-burner zone. Furthermore, E. Chui, who was partially supported by this contract during his PhD studies, is now applying his knowledge in his job at the ERL Laboratory.

REFERENCES

Bird, R. B., Stewart, W. E. and Lightfoot, E. N., Transport Phenomena, John Wiley & Sons, 1960.

Chui, E. H-K and Hughes, P. M. J. (1991), Combustion and Carbonization Lab, CANMET, Personal communication.

Chui, E. H-K, (1990), Modelling of Radiation Heat Transfer in Participating Media by the Finite Volume Method, PhD Thesis, Dept. of Mechanical Engineering, University of Waterloo.

Chui, E. H-K and Hughes, P. M. J. (1991), Personal communication.

Howell, J. R. (1988), "Thermal Radiation in Participating Media: The Past, the Present, and Some Possible Futures", *Journal of Heat Transfer*, Vol. 110, pp. 1220-1226.

Lockwood, F. C. and Shah, N. G. (1981), "A New Radiation Solution Method for Incorporation in General Combustion Prediction Procedures", 18th Symposium on Combustion, Waterloo, Canada.

Panton, R. L. (1984), Incompressible Flow, McGraw-Hill, p.134.

Raithby, G. D. and Chui, E. H-K (1990), A Finite-Volume Method for Predicting Radiant Heat Transfer in Enclosure with Participating Media, *J. Heat Transfer*, Vol. 112, pp. 415-423.

Rizvi, S. M. A. (1985), Prediction of Flow, Combustion and Heat Transfer in Pulverized Coal Flames, PhD Thesis, Dept. Mech. Eng., Imperial College.

Siegel, R. and Howell, J. R. (1981), Thermal Radiation Heat Transfer, Hemisphere Publishing, New York.

Thorpe, J. F. (1962) *Am. J. Phys.*, 30, p.637.

Viskanta, R. (1984), "Radiative Heat Transfer", *Fortschrift der Verfahrenstechnik*, Vol. 22A, pp. 51-81.

Viskanta, R. and Megüç, M. P. (1987), "Radiation Heat Transfer in Combustion Systems", *Progress in Energy and Combustion Science*, Vol. 13, No. 2, pp. 97-160.

9 APPENDIX A: REVIEW OF INTEGRAL RELATIONS

A.1 Leibnitz Rule

A control volume, with surface area S and volume $\forall$, is shown in Fig. 24. The control volume surface moves at local velocity $\vec{W}$, which is in general different from the local fluid velocity $\vec{V}$. The position of the control surface at time t and at $t + dt$ are shown. The outward unit vector that is normal to S is $\hat{n}$.

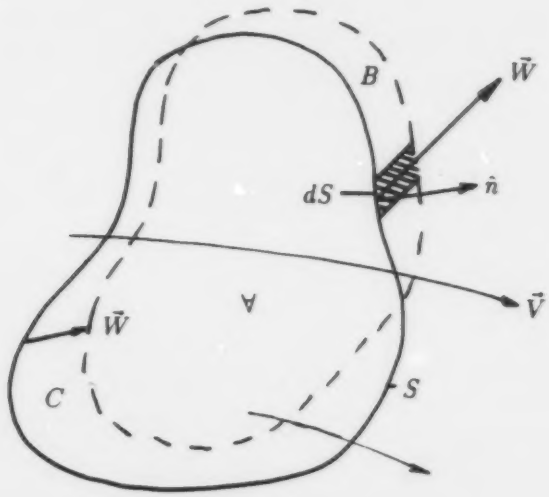

Figure 24: Definition sketch of control volume.

Let $f(x_i, t)$ be any property of the fluid expressed on a per unit volume basis. The total amount of this property within $\forall$ at time t is

$$F(t) = \int_{\forall(t)} f(x_i, t) d\forall \tag{171}$$

The rate of increase of F with t within the control volume (for the volume moving at its velocity $\vec{W}$ and its surface traversed by fluid moving at $\vec{V}$) is given by Leibnitz rule

$$\frac{dF}{dt} = \int_S f\vec{W} \cdot \hat{n} dS + \int_\forall \frac{\partial f}{\partial t} d\forall \tag{172}$$

This result can (of course) be rigorously derived but is so obvious that such a derivation is superfluous, and perhaps masks the simple underlying idea.

The second term on the RHS of Eq. (172) in Eq. (172) denotes the increase in F due to the increase in f at each location within the volume. It is immaterial whether $\forall$ is evaluated at t or $t + dt$; the difference between using $\forall(t)$ and $\forall(t + dt)$ is a higher order term that can be neglected for $dt \to 0$.

Because the control surface moves, some new fluid is 'captured' within $\forall$ (e.g., fluid within region B in Fig. 25), while other fluid that was within $\forall$ becomes 'lost' (e.g., fluid within region C). The new volume captured through the surface area dS in Fig. 24, denoted by cross-hatching, is $\vec{W} \cdot \hat{n} dS dt$. The amount of f captured through dS is therefore $f\vec{W} \cdot \hat{n} dS dt$. The integral over S of this quantity (term 1 on the RHS of Eq. (172)) is therefore the net increase in f captured through S in dt. Where $\vec{W} \cdot \hat{n}$ is positive, f has been captured (region B in Fig. 24) and where $\vec{W} \cdot \hat{n}$ is negative, f has been lost (region C in Fig. 24).

Example 1: $f = 1$

Application of Eq. (172) yields

$$\frac{d\forall}{dt} = \int_S \vec{W} \cdot \hat{n} dS \tag{173}$$

This is an obvious equation for the rate of increase of the volume of the control volume. It has sometimes been called the 'law of space conservation'.

Example 2: $f = \rho(x_i, t)$

$$F = \int_\forall \rho(x_i, t) d\forall = M(t) = \text{mass within } \forall(t)$$

Applying Eq. (172)

$$\frac{dM}{dt} = \int_S \rho \vec{W} \cdot \hat{n} dS + \int_\forall \frac{\partial \rho}{\partial t} d\forall \tag{174}$$

Example 3: $f = \rho g$, where g is any intensive (per unit mass) property.

$$f = \int_\forall \rho g d\forall = G(t)$$

From Eq. (172)

$$\frac{dG}{dt} = \int_S \rho g \vec{W} \cdot \hat{n} dS + \int_\forall \frac{\partial}{\partial t}(\rho g) d\forall \tag{175}$$

The symbol g could represent a velocity component u_i (i.e., i-momentum per unit mass), energy per unt mass, etc.

Leibnitz equation is frequently used in the derivations of this Report.

A.2 Gauss' Theorem

The usual form of Gauss' Theorem is

$$\int_{\forall} \vec{\nabla} \cdot \vec{B} d\forall = \int_S \vec{B} \cdot \hat{n} dS \tag{176}$$

where $\vec{B} = (B_x, B_y, B_z)$ here is a vector that represents a flux of something per unit area normal to the $\vec{B}$-direction (e.g., $\vec{q}$ = heat flux, $\rho\vec{V}$ = mass flux, $\rho\vec{V}g$ = flux of g transported with the mass, etc.) This relation can also be rigorously proved but with a little algebra it too is self evident.

The RHS of Eq. (176) is a statement of the transport of F across the boundary S.

In 2D, LHS of Eq. (176) is the volume integral

$$\begin{aligned} \int_{\forall} \vec{\nabla} \cdot \vec{B} d\forall &= \lim_{\Delta\forall_k \to 0} \sum_k \left(\frac{\partial B_x}{\partial x} + \frac{\partial B_y}{\partial y} \right)_k \Delta\forall_k \\ &= \lim_{\Delta\forall_k \to 0} \sum_k \left\{ \left[\frac{B_x(x+dx) - B_x(x)}{dx} \right]_k \Delta\forall_k \right. \\ &+ \left. \left[\frac{B_y(y+dy) - B_y(y)}{dy} \right] \Delta\forall_k \right\} \end{aligned} \tag{177}$$

Recognizing that, for example, $B_x(x+dx)\Delta\forall/dx \to B_x(x+dx)A_x = F_x(x+dx)$ which is the flux of B through the $x+dx$ face of $\Delta\forall$, Eq. (177) can be written as

$$\begin{aligned} \int_{\forall} \vec{\nabla} \cdot \vec{B} d\forall &= \{F_x(2) - F_x(1) + F_y(2) - F_y(1)\} + \{F_x(3) - F_x(2) + F_y(3) \\ &- F_y(4)\} + \{F_y(4) - F_y(5) + F_x(5) - F_x(4)\} + \cdots \end{aligned} \tag{178}$$

These fluxes are shown in Fig. (25).

Note that when the summation is performed, fluxes across all interior faces cancel, leaving only the net flux of B through the exterior control volume faces. Equation (176) is therefore the obvious outcome of this cancellation.

Gauss' Theorem is valid not only for vectors but for scalars and tensors as well. The general equation is

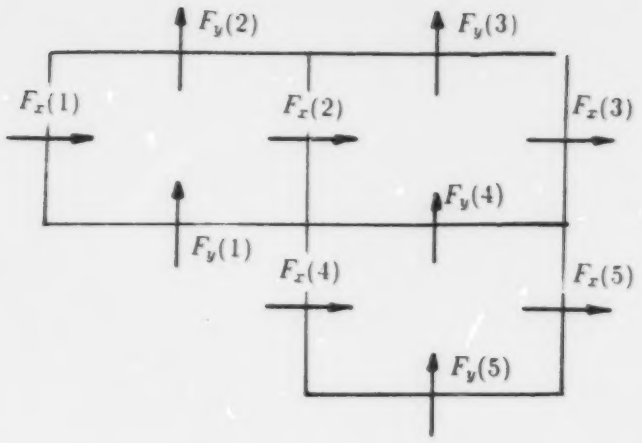

Figure 25: Figure showing fluxes across differential control volume faces.

$$\int_{\forall} \frac{\partial B_j}{\partial x_j} d\forall = \int_S B_j n_j dS \tag{179}$$

When B_j are components of a vector $\vec{B}$, Eq. (179) is seen to be equivalent to Eq. (176). If $B_j = p$, a scalar

$$\int_{\forall} \frac{\partial p}{\partial x_j} d\forall = \int_S p n_j dS \tag{180}$$

This is also easy to prove. Using Fig. 26

$$\int_{\forall} \frac{\partial p}{\partial x_j} d\forall = \int_{\forall} \frac{\partial p}{\partial x_j} dx_j dA = \int_A (p_2 - p_1) dA = \int_S p\hat{n} \cdot \hat{e}_j dS = \int_S p n_j dS \tag{181}$$

which is exactly Eq. (180). It is the interior cancellation that gives rise to the second quality, that again leads to Eq. (180).

For a tensor, e.g., τ_{ji}, Eq. (179) becomes

$$\int_{\forall} \frac{\partial \tau_{ji}}{\partial x_j} d\forall = \int_S \tau_{ji} n_j dS$$

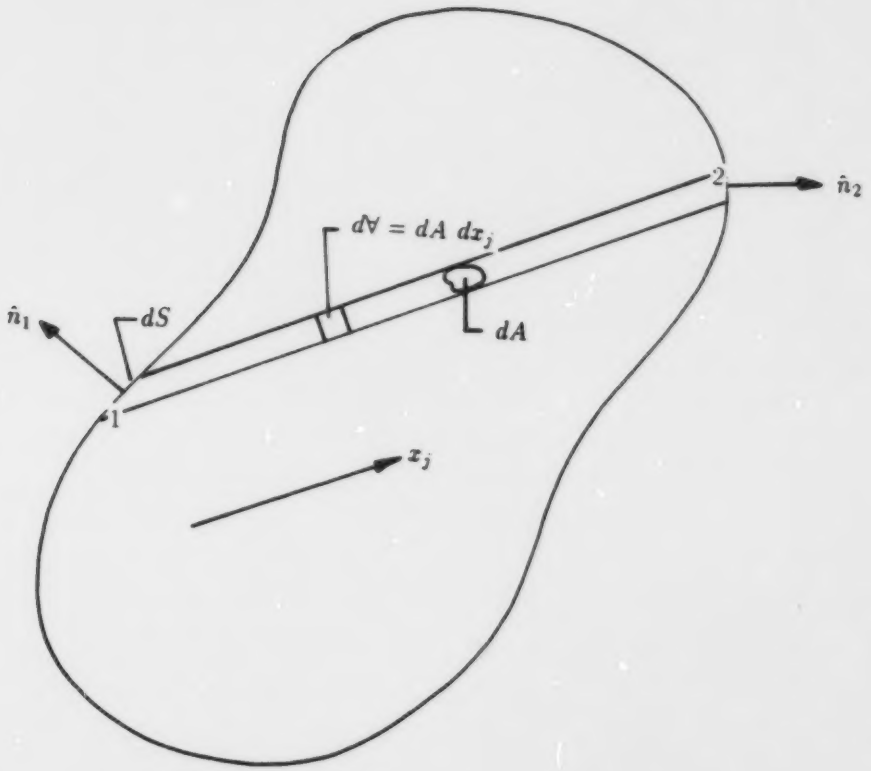

Figure 26: Figure for application of Gauss' Theorem to a scalar.

10 Appendix B - A Finite-Volume Method for Predicting Radiant Heat Transfer in Enclosures with Participating Media

Reprinted from May 1990, Vol. 112, Journal of Heat Transfer

A Finite-Volume Method for Predicting a Radiant Heat Transfer in Enclosures With Participating Media

G. D. Raithby

E. H. Chui

Department of Mechanical Engineering,
University of Waterloo
Waterloo, Ontario, Canada N2L 3G1

A new "finite-volume" method is proposed to predict radiant heat transfer in enclosures with participating media. The method can conceptually be applied with the same nonorthogonal computational grids used to compute fluid flow and convective heat transfer. A fairly general version of the method is derived, and details are illustrated by applying it to several simple benchmark problems. Test results indicate that good accuracy is obtained on coarse computational grids, and that solution errors diminish rapidly as the grid is refined.

Introduction

Fluid flow and convective heat transfer can now be predicted with reasonable economy and accuracy in very complex geometries. Most methods use finite difference, finite volume, or finite element methods to reduce the continuous equations of motion to a set of coupled algebraic equations that can be solved by computer. For many situations, e.g., flows with combustion, it would be desirable to add a solution for radiant exchange to the code that solves the fluid flow and internal energy equations; it would be convenient if the radiation model were based on the same philosophy and perhaps even used the same computational grid, as the fluid flow solver. Among the solution methods that are currently available, such as the many variations on the Monte Carlo, Zonal, Ray Tracing, Flux, and Discrete Ordinates methods none is fully satisfactory for this purpose except in the limit when the diffusion approximation applies (optically dense medium). Since excellent recent reviews of the state of the art are provided by Viskanta and Mengüç (1984, 1987), the competing methods for predicting radiative heat exchange will not be reviewed here.

According to the finite volume method, a solution domain is subdivided by a computational mesh that defines nodes for each variable and a control volume surrounding each node. To compute flows in complex domains, the flexibility allowed by a nonorthogonal boundary-fitted mesh is desirable. The present paper describes a new method for predicting radiative heat transfer that also uses such a grid. Besides using the same mesh as the flow solver, the method accounts for absorption, emission, and scattering in the medium, permits spectral dependence through a broad-band model (Viskanta and Mengüç, 1987), allows radiation properties to depend on other variables (like local pressure, concentration and temperature), and permits desired reflectivity properties of the wall to be incorporated. The method is also fully conservative in the sense that the global conservation balance for each discrete intensity component, as well as for the radiative flux, is exactly satisfied by the discrete equations.

The model has, until now, only been exercised for simple cases. These include heat transfer in rectangular enclosures, with diffuse gray isothermal walls, that contain gray emitting-absorbing and/or isotropically scattering media. To limit the model description to these cases would, however, make it difficult to appreciate the general applicability of the model. On the other hand, to provide the model in its full generality would result in notational complexity that would encumber the presentation. As a compromise, generality is restricted in those areas where removing the restriction is obvious and simple (e.g., gray medium and diffuse wall). The complexity of a nonisotropically scattering medium and a nonorthogonal grid is retained in the model development, even though these are not used in the test problems.

Finite Volume Approximation

The Volume-Integrated Equation for Intensity. Referring to the definition sketch (Fig. 1A) $\mathbf{r}$ denotes a location in space, $d\omega$ is a differential solid angle that is centered on the unit vector $\mathbf{s}$, and s is distance along a particular pencil of radiation that lies in the $\mathbf{s}$ direction. Over the path length ds in the direction of the unit vector $\mathbf{s}$, the rate of increase of total intensity $I(\mathbf{r}, \mathbf{s})$ is (Siegel, 1981)

$$\frac{dI}{ds} = -(K + \sigma^s)I + (KI_b + \sigma^s \bar{I}) \tag{1}$$

where the first term on the right-hand side is attenuation through absorption and outscattering and the second term is augmentation due to emission and inscattering. Because of the gray-medium approximation, the absorption coefficient K and the scattering coefficient σ^s are appropriate wavelength-averaged quantities. The inscattering term is given by

$$\bar{I}(\mathbf{r}, \mathbf{s}) = \frac{1}{4\pi} \int_{4\pi} I(\mathbf{r}, \mathbf{s}')\Phi(\mathbf{s}, \mathbf{s}')d\omega' \tag{2}$$

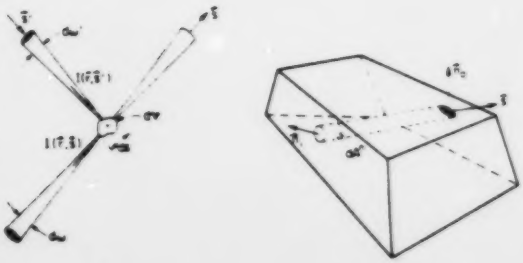

A B

Fig. 1 Part A shows notation used in the model. The control volume, for which the integral equation for intensity is derived, appears in B.

Contributed by the Heat Transfer Division and presented at the National Heat Transfer Conference, Philadelphia, August 6-9, 1989. Manuscript received by the Heat Transfer Division December 8, 1988. Keywords: Numerical Methods, Radiation, Radiation Interactions.

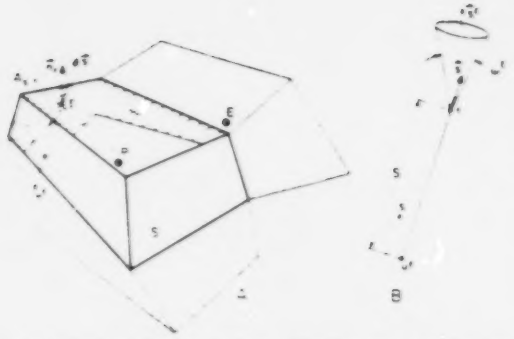

Fig. 2 Discrete surface panels on the discrete volume centered at P, and neighbor control volumes. The intensity I'_p, from which the flux through $A_{s,f}$ is found, is expressed as an "upstream" value I'_{up} found by interpolation from nodal values, and a change between up and f.

where $I(\mathbf{r}, \mathbf{s}')$ is the intensity at $\mathbf{r}$ within the solid angle $d\omega'$ that lies in the direction of the unit vector $\mathbf{s}'$.

Integration of equation (1) over any specified volume yields the desired integral equation. Choosing the hexahedron in Fig. 1(B) for purposes of illustration, the volume is subdivided into pencils along $\mathbf{s}$ of the cross-sectional area dA^*. Multiplication of equation (1) by the differential volume $d\mathcal{V} = dA^* ds$, carrying out the integration, and multiplying the resulting equation by $d\omega$, yields

$$\int_{A_s} I_s(\mathbf{s}\cdot\mathbf{n})dA_s d\omega = \int_{\mathcal{V}} [-(K+\sigma^s)I + KI_b + \sigma^s \bar{I}]d\mathcal{V}d\omega \qquad (3)$$

where A_s and $\mathcal{V}$ are the surface area and volume of the hexahedron, $\mathbf{n}$ is the unit surface normal, and I_s is the intensity at the surface. This equation demands that the net radiant energy within $d\omega$ that leaves through all surfaces of the volume is exactly balanced by the excess, within the volume, of inscattering and emission over outscattering and absorption.

Discrete Equation, Level 1 Approximation. According to the finite volume method, space within the interior of the domain of interest is subdivided into discrete nonoverlapping volumes, and a single "node" is located centrally within each volume. The control volume in Fig. 1(B) is redrawn in Fig. 2, showing its central node P, and nodes E and S for the neighboring control volumes to the east and south.

Since direction is also an independent variable, it is consistent with the finite volume method to subdivide direction into N^l discrete, nonoverlapping, solid angles of size ω^l, $l = 1, 2, 3, \ldots$, which sum to 4π. The number of angles and their size distribution is, like the discretization of space, at the discretion of the analyst.

The objective of the finite volume method is to find I'_p, the intensity at each node P associated with each discrete bundle ω^l. An algebraic equation for I'_p, is obtained by introducing approximations into equation (3).

Choosing the volume in equation (3) to be the control volume associated with node P in Fig. 2, with surface area $A_{S,p}$, and integrating the equation over the discrete solid angle ω^l, (3) becomes

$$\int_{\omega^l}\int_{A_{S,p}} I_S(\mathbf{s}\cdot\mathbf{n})dA_S d\omega = \int_{\omega^l}\int_{\mathcal{V}_p} [-(K+\sigma^s)I + KI_b + \sigma^s \bar{I}]d\mathcal{V}d\omega \qquad (4)$$

The simplest approximation of the right-hand side of equation (4) is

$$\int_{\omega^l}\int_{\mathcal{V}_p} [-(K+\sigma^s)I + KI_b + \sigma^s \bar{I}]d\mathcal{V}d\omega = [-(K_p+\sigma^s_p)I'_p + K_p I'_{b,p} + \sigma^s_p \bar{I}'_p]\mathcal{V}_p\omega^l \qquad (5)$$

In carrying out the volume integrations, all variables have been assumed constant over $\mathcal{V}_p$ and ω_l. A more accurate representation, involving, for example some linear distribution between nodes, is possible but is both more complex and may have serious negative computational effects (like a strong coupling between intensities in different directions that is not consistent with equation (1)).

As the first step to approximating the left-hand side of equation (4), the surface of the control volume is subdivided into N_f surface panels of area $A_{S,f}$, a few of which are shown in Fig. 2(A). Denoting the radiant transfer through panel f and within ω^l by Q^l_f, the left-hand side of equation (4) is just the

Nomenclature

A_s = surface area of control volume, m^2
$A_{s,f}$ = surface area of panel f of control volume, m^2
B_p = source term in algebraic equation, e.g., equation (24)
D = depth of one-dimensional plane layer, m
$\mathbf{e}_j$ = unit vector in the j direction
I = radiation intensity, W/m^{2}Sr
$\bar{I}$ = scattered intensity, W/m^{2}Sr, see equation (2)
I_a = average intensity, equation (13)
I_b = blackbody intensity $= \sigma T^4/\pi$
I'_b = discrete intensity at the bottom surface within ω^l
I'_p = discrete intensity at node P within ω^l
I_S = intensity at surface control volume
I'_T = discrete intensity at the top surface within ω^l
K = absorption coefficient, m^{-1}
L_x, L_y = dimensions of rectangular cavity in x and y directions, m
m = index denoting the ω^l with boundaries at θ^m_- and θ^m_+ (see Fig. 3(B))
n = index denoting the ω^l with boundaries at ϕ^n_- and ϕ^n_+
$\mathbf{n}$ = unit vector normal to a control volume surface
N^l = total number of discrete solid angles
N_x, N_y, N_z = number of control volumes in the x, y, and z directions, respectively
N^θ, N^ϕ = number of discrete angles in θ and ϕ directions
q = heat flux, W/m^2
Q = total radiant heat transfer rate, W
Q^l_f = radiant heat transfer across surface panel f
$\mathbf{r}$ = position in space
R = $(KI_b + \sigma^s \bar{I})/\pi$, W/m^{2}Sr
$\hat{R}, \bar{R}$ = see equation (21)

attenuation) from the interpolation point *uf* to the integration point on the panel.

In the optically thick limit ($\kappa_f \to \infty$)

$$Q_f' - A_{s,f} R_f' \int_{\omega=f} (\mathbf{s}\cdot\mathbf{e}_3)\,d\omega - \frac{A_{s,f}}{\kappa_f} \sum_{j=1}^{3} \left(\frac{\partial R'}{\partial x_j}\right)_f \int_{\omega=f} (\mathbf{e}_j\cdot\mathbf{s})(\mathbf{s}\cdot\mathbf{e}_3)\,d\omega$$

Summing over l to obtain the net radiant heat transfer crossing the panel, and for isotropic scattering (so that R becomes independent of angle l)

$$Q_f = \sum_l Q_f' = A_{s,f}\left(-\frac{4\pi}{3\kappa_f}\right)\left(\frac{\partial R}{\partial x_3}\right)_f$$

This is the correct diffusion approximation for the optically thick limit (Siegel, 1981). Thus the expression for Q_f given by equation (10) has retained sufficient generality to capture both the optically thin and thick limits. Note that, had the third term in equation (9) been omitted (which is the usual solution (Siegel, 1981) to (8*A*) for constant κ and R), the radiation heat transfer across the panel would not have recovered the diffusion approximation.

Returning to the development of the discrete equation for I_P', equation (10) is substituted into equation (7). The only remaining issues are how to interpolate I_{uf}' from nodal-point values like I_P', and how to find R_f'. As already mentioned, the interpolation will be illustrated when the method is implemented on a specific mesh. The value of R_f' is obtained by a straightforward linear interpolation using values of R', such as R_P', that are calculated and stored at the nodes.

To find R_P' at the nodes requires an evaluation of both its components (see equation (8*B*)) $\bar{I}_P'$ and $I_{b,P}$. $\bar{I}_P'$ is obtained from the following discrete approximations to equation (2):

$$\bar{I}_P' = \frac{1}{4\pi} \sum_{l'} I_P' \Phi(l', l)\omega^{l'} \tag{12}$$

where $\Phi(l', l)$ is the phase function for scattering from the solid angle $\omega^{l'}$ to the solid angle ω^l. For isotropic scattering, $\Phi = 1$ and equation (12) becomes

$$\bar{I}_P' = \frac{1}{4\pi} \sum_{l'} I_P' \omega^{l'} = I_{a,P} \tag{13A}$$

where $I_{a,P}$ is the discrete approximation at node P of the average intensity I_a:

$$I_a(\mathbf{r}) = \frac{1}{4\pi}\int_{4\pi} I(\mathbf{r}, \mathbf{s}')\,d\omega' \tag{13B}$$

The value of the second component of R_P, i.e., $I_{b,P} = \sigma T_P^4/\pi$, is found from the thermal energy balance for the P control volume. The increase in internal energy due to radiation crossing the boundaries of the control volume in Fig. 2(*A*) is obtained by replacing the integration limit ω^l in equation (4) by 4π.

$$-\int_{A_{S,P}} \int_{4\pi} I(\mathbf{s}\cdot\mathbf{n})\,d\omega\,dA_S = 4\pi \int_{\forall_P} K(I_a - I_b)\,d\forall \tag{14A}$$

$$= 4\pi K_P (I_{a,P} - I_{b,P})\forall_P \tag{14B}$$

The scattering contribution drops out of this energy balance for both isotropic and nonisotropic scattering. The temperature is established, in general, by a complex interaction (Siegel, 1981) of this term with advection and diffusion of energy, and with work done by the pressure and other stresses. For the simplest case of radiative equilibrium, the fluid temperatures adjusts to make the net surface heat transfer in equation (14*A*) zero, so that

$$I_{b,P} = I_{a,P} \tag{15}$$

For the special case of isotropic scattering and radiative equilibrium, combining equations (8*B*), (13), and (15) results in

$$R_P' = R_P = I_{a,P} = I_{b,P} \tag{16}$$

Summary and Discussion. This section has provided the details of a general finite volume method, except for the interpolation to obtain I_{uf}' and the application of boundary conditions. These details, and the performance of the method, are illustrated in the following sections by application to some simple problems for which benchmark solutions are available.

One-Dimensional Radiant Heat Transfer in a Plane Medium

Problem Description. Very precise solutions (Heaslet, 1965) (see Viskanta and Mengüç 1987 for other references) have been obtained for radiant heat transfer between two isothermal, diffuse, flat plates, at temperatures T_B and T_T and emissivities ϵ_B and ϵ_T (see Fig. 3), that enclose a gray isotropically scattering or absorbing-emitting medium with constant scattering and absorption coefficients, and that is in radiative equilibrium. The finite volume method is first applied to this problem.

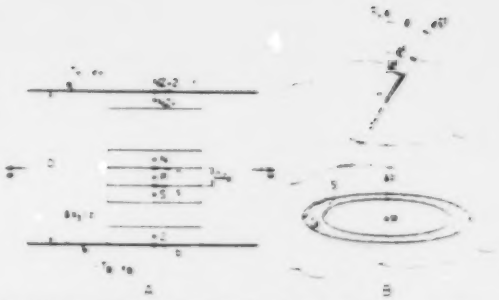

Fig. 3 Geometry and control volumes for radiation in a plane participating medium contained between isothermal gray walls

Discrete Equations. The natural control volumes for this problem are shown in Fig. 3(*A*). The depth Δz of each control volume is arbitrary and nodes are located midway between the control volume faces, except for the first and last nodes, which are located on the plates. Integration points, like n and s, which are denoted by $\times$, lie on the volume faces. On the walls, the integration points b and t lie in the medium distance δ from the walls, where $\delta \to 0$.

For this problem, the radiation intensity depends on z and θ (Fig. 3(B)). The discrete solid angle ω^l is defined as the annular cone between θ_-^l and θ_+^l. The interpolation point *uf* that is upstream of the integration point n is taken to lie on the plane of node P, as shown in the figure. From the assumption that the intensity varies spatially only with z, I_{uf}' in equation (10) can be replaced by I_P^l for $\mathbf{s}\cdot\mathbf{e}_3 > 0$ and by I_N^l for $\mathbf{s}\cdot\mathbf{e}_3 < 0$. For $\mathbf{s}\cdot\mathbf{e}_3 > 0$, the radiant heat transfer within ω^l that travels through the control volume surface n that lies north of node P is, according to equation (10) and Fig. 3(*B*)

$$Q_n^l = F_n^l I_P^l + G_n^l R_n - H_n^l \left(\frac{\partial R}{\partial z}\right)_n \tag{17}$$

where the angular dependence of R has been dropped due to the isotropic scattering approximation. In this equation

$$F_n^l = A_S e^{-\kappa S^l} N^l \qquad G_n^l = A_S(1 - e^{-\kappa S^l})N^l \tag{18A}$$

$$H_n^l = \frac{A_S}{\kappa}(1 - e^{-\kappa S^l}(1 + \kappa S^l))D_l^l \tag{18B}$$

$S^l = (z_n - z_P)/\cos\theta^l$ is defined here as the distance S in Fig.

3(B) for the angle $\theta = \theta' = (\theta'_{i-} + \theta'_{i+})/2$. From equation (11) for this geometry

$$N' = \int_{\omega'} (\mathbf{s}\cdot\mathbf{e}_z)\,d\omega = -\pi[\cos^2\theta'_{i-} - \cos^2\theta'_{i+}] \tag{18C}$$

$$D'_i = \int_{\omega'} (\mathbf{s}\cdot\mathbf{e}_z)^2\,d\omega = -\frac{2\pi}{3}[\cos^3\theta'_{i-} - \cos^3\theta'_{i+}] \tag{18D}$$

and the solid angle is

$$\omega' = \int_{\theta'_{i-}}^{\theta'_{i+}} 2\pi \sin\theta\,d\theta = -2\pi[\cos\theta'_{i-} - \cos\theta'_{i+}] \tag{18E}$$

Substitution of equation (17) for Q'_{i-} and a similar equation for the heat transfer through the south face Q'_{i+} into equation (7), and collection of all terms involving R into a "source term," b'_p, results in the following equation for I'_p (for $\mathbf{s}\cdot\mathbf{e}_z > 0$):

$$a'_p I'_p = a'_S I'_S + a'_{i-} I'_{i-} + b'_p \tag{19A}$$

where

$$a'_p = F'_n + \kappa\mathcal{V}_p\omega' \qquad a'_S = F'_s \qquad a'_{i-} = D'_i \tag{19B}$$

$$b'_p = \left[G'_e R_e - H'_e\left(\frac{\partial R}{\partial z}\right)_e\right] - \left[G'_w R_w - H'_w\left(\frac{\partial R}{\partial z}\right)_w\right] + \kappa R_p \mathcal{V}_p \omega' \tag{19C}$$

The values of R and $(\partial R/\partial z)$ at an integration point (i.e., at a face) are found by linear interpolation of the nodal point values or, at the top and bottom plates, by linear extrapolation from interior nodal values.

For a diffuse top surface, at temperature T_T, the boundary condition for the surface intensity I'_T for radiation into the medium, $\mathbf{s}'\cdot\mathbf{e}_z < 0$, is

$$(1-\epsilon_T)\sum_{\mathbf{s}'\cdot\mathbf{e}_z>0} Q'_i + \epsilon_T A_S \sigma T_T^4 = \sum_{\mathbf{s}'\cdot\mathbf{e}_z<0} Q'_T = A_S \pi I'_T \tag{20}$$

The terms on the left-hand side of equation (20) represent reflected and emitted radiation from the T surface, which constitute the total radiation into the medium. The last equality defines the intensity through the gray-surface approximation. A similar equation at the bottom surface relates the intensities into the medium ($\mathbf{s}'\cdot\mathbf{e}_z > 0$) to the bottom surface temperature and to intensities incident on the bottom.

Solution Method. For fixed nodal values of R and upward intensities at the bottom surface, I'_p values are found for a given I by application of equation (19A) to each interior node, starting at the bottom and sweeping upward. This is repeated for each I for which $\mathbf{s}'\cdot\mathbf{e}_z > 0$. Equation (17) provides the incident fluxes onto the top surface, from which equation (20) gives the downward intensities. Equations similar to equation (19A), but with a'_S rather than a'_{i-} equal to zero, are then solved for the downward intensities and incident fluxes on the lower surface. The lower surface boundary condition yields the upward boundary intensities to complete one cycle.

If the nodal values of R are fixed, one cycle yields the desired result if $\epsilon_B = \epsilon_T = 1.0$. Several cycles will be required for reflective boundaries.

The determination of R is, of course, part of the solution procedure. The simplest "explicit" method is to obtain the intensities for an assumed R in the manner just described, to substitute these into equation (13A) and thus obtain new R values from equation (16). This cycle is repeated until convergence is achieved. Convergence was deemed satisfactory when the change, between successive updates of R, in net heat flux at both surfaces was less than 0.001 percent.

Results. When a fine grid (see below) was used, the non-dimensional heat transfer, $q^* = q/\sigma(T_B^4 - T_T^4)$, obtained using the finite volume method agreed to within 1 in the fourth significant figure with the predictions reported by Heaslet and Warming (1965). The gas temperature, and temperature jump at the boundary, were also predicted correctly.

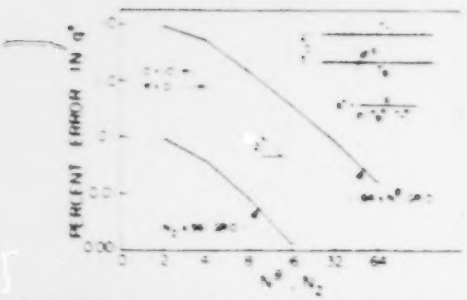

Fig. 4 Results of computational experiments to determine the rate at which the error in heat transfer from the surface decreases with grid refinement. The slope of 2:1 on the figure denotes quadratic convergence.

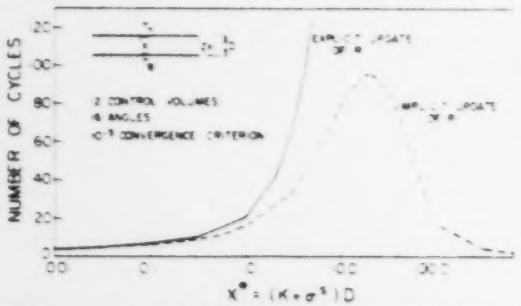

Fig. 5 The number of R-update cycles required to obtain a wall heat transfer that changed less than 0.001 percent between cycles

Table 1 Comparison of finite volume results for uniform grid of four control volumes and eight angles with "exact" results (Heaslet and Warming, 1965); $\kappa^* = \kappa D$

κ^*	$q^* = q/\sigma(T_B^4 - T_T^4)$ Coarse grid finite volume results	Exact results	Percent error	CPU, s
0.0	1.0000	1.0000	0.0	0.1
0.1	0.9125	0.9157	0.3	0.2
0.5	0.6964	0.7040	1.1	0.3
1.0	0.5469	0.5532	1.1	0.4
2.0	0.3865	0.3900	0.9	0.4

Even for a coarse grid (see Fig. 3) of four uniform control volumes in the z direction and with polar angle θ divided into eight equal intervals, the finite volume method predicts the correct heat transfer to within about 1 percent, for a wide range of optical depths, as shown in Table 1. The CPU time required was less than 0.5 s on a MicroVax II computer.

Having established that the finite volume method does yield the correct results as the grid is refined, it is of major interest to establish how quickly the accuracy improves with grid refinement. For $\kappa^* = \kappa D$ of 1.0, the heat transfer was obtained using $N_z = 64$ uniform control volumes and $N' = N'' = 96$ equal angle intervals. To study error reduction with N_z, q^* was recalculated on a sequence of grids of size $(N_z \times 96)$, $N_z = 2, 4, \ldots, 64$. The results in Fig. 4 indicate the q^* is obtained to within 0.1 percent with $N_z = 2$, and for $N_z \geq 4$ the error becomes proportional to $(N_z)^{-2}$ (i.e., quadratic convergence).

To study error reduction with angular refinement, q^* was calculated for grids of $(64 \times N^\theta)$, $N^\theta = 2, 4, 6, \ldots, 96$. The error decreases from about 10 percent for $N^\theta = 2$, and for $N^\theta \geq 4$, and decreases roughly as $(N^\theta)^{-2}$.

Another issue of major interest is the number of updates of R required to obtain convergence. For black surfaces, and for a change of q^* at the surfaces of less than 0.001 percent between R updates, the number of iterations required by the explicit method is plotted against $\kappa^* = \kappa D$ in Fig. 5. As $\kappa^* \to 0$, the correct solution is obtained without iteration because the intensities become independent of R. The number rises sharply with κ^* but convergence is satisfactory for $\kappa^* < 4.0$, which includes the range of interest for many practical applications. The number of iterations increases sharply with κ^* for $\kappa^* \leq 4.0$. A similar behavior, of increasingly difficult convergence with increasing κ^*, has been encountered in the use of the discrete ordinates method (Viskanta and Menguç, 1987). The next section addresses this issue.

Implicit Solution for Strongly Participating Medium. For applications that involve strongly participating media ($\kappa^* \geq 4$ for a plane layer), the explicit update of R becomes unsatisfactory. This section describes a method that enhances convergence for large κ^*. The method is, for simplicity, presented in the context of the present one-dimensional problem, but the derivation is kept sufficiently general to include nonisotropic scattering.

To re-introduce nonisotropic scattering, R in equation (19C) is replaced by R', and the nodal values of R are split as follows:

$$R'_{\omega^l p} = \frac{K_p I_{b,p} + \sigma'_p I_{a,p}}{\kappa_p} + \frac{\sigma'_p}{\kappa_p}(\bar{I}'_p - I_{a,p}) = \hat{R}_p + \hat{R}'_p \qquad (21)$$

For isotropic scattering, $\hat{R} = 0$. Expressing the integration point values of R'_f and $(\partial R^l/\partial z)_f$, $f = s$ and n, in equation (19C) in terms of nodal point values using linear interpolation, substituting the resultant b'_p expression into equation (19A), and dividing by a'_p, yields an equation for $\bar{I}'_p$ of the form

$$\bar{I}'_p = \frac{a'_S}{a'_p}\bar{I}'_S + \frac{a'_N}{a'_p}\bar{I}'_N - A'_p\hat{R}_p + A'_S\hat{R}_S + A'_N\hat{R}_N + B'_p \qquad (22)$$

where terms involving $\hat{R}'$ have been grouped into B'_p. Multiplication of equation (22) by ω^l, summation over all ω^l, and division of the resulting equation by 4π yields an equation of the form

$$I_{a,p} = -\hat{A}_p\hat{R}_p + A_S\hat{R}_S + A_N\hat{R}_N + B_p \qquad (23)$$

For the special case of isotropic scattering and radiative equilibrium, $\hat{R}_p = I_{a,p}$ (from equation (16)) so that equation (23) becomes

$$A_p I_{a,p} = A_S I_{a,S} + A_N I_{a,N} + B_p \qquad (24)$$

which is an implicit equation for $I_{a,p} = I_{b,p}$ that is simply solved by application of the Thomas (or tridiagonal) algorithm. This replaces the "explicit" update of R described in the previous section. It is also easily shown that, as $\kappa^* \to \infty$, equation (24) becomes the discrete representation of the diffusion approximation of radiation heat transfer. For large κ^*, therefore, the first solution for $I_{a,p}$ will yield nearly the correct $I_{a,p} = R_p$ values, which, used in the b'_p term in equation (19A), will yield nearly converged values of $\bar{I}'_p$, so that very few cycles will lead to the converged result.

Figure 5 shows the number of cycles required by this implicit method to obtain surface heat transfers that changed less than 0.001 percent between R-update cycles. The maximum number of cycles is required for $\kappa^* \approx 20$. For $\kappa^* \to 0$ and $\kappa^* \to \infty$, the converged results are obtained in one solution cycle.

Although the method has not yet been applied to problems involving nonisotropic scattering and radiative nonequilibrium, it is interesting to speculate how the implicit method could be used to accelerate convergence. Splitting $\hat{R}$ in equation (23) into its I_a and I_b components results in an equation of the form

$$A^{ap}_p I_{a,p} = A^{ap}_S I_{a,S} + A^{ap}_N I_{a,N} - A^{bp}_p I_{b,p} + A^{bp}_N I_{b,S} + A^{bp}_S I_{b,S} + B^{ap}_p \qquad (25)$$

where the first superscript on the coefficients refers to the equation and the second to the variable it multiplies (either a for the variable I_a or b for the variable I_b).

The thermal energy equation has diffusion and convection terms that are linear in T, and a source term given by equation (14B) that contains I_a and $I_b = \sigma T^4/\pi$. If radiation dominates the internal energy balance, it is appropriate to linearize the discrete energy equation in the form

$$A^{bp}_p I_{b,p} = A^{bp}_S I_{b,S} + A^{bp}_N I_{b,N} + A^{ap}_p I_{a,p} + B^{bp}_p \qquad (26)$$

Equation (25) and (26) can be efficiently solved for $I_{a,p}$ and $I_{b,p}$ (e.g., use a (2×2) block tridiagonal solver). If radiation only weakly affects the medium temperature, it would be more appropriate to linearize the equations such that T instead of I_b appears as the dependent variable in equations (25) and (26). In either case, iteration is required to converge to the solution of the equations in which some terms involve T and others T^4.

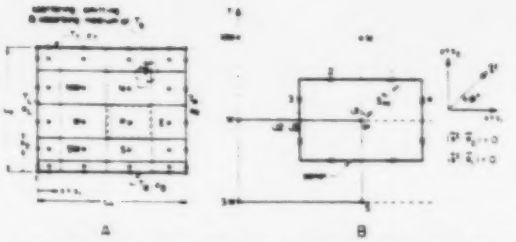

Fig. 6 Schematic of a rectangular cavity with isothermal walls with a Cartesian computational grid. Part B shows details related to determination of the integration point intensities for those intensities that are directed upward and to the right.

Two-Dimensional Exchange in Rectangular Enclosures

Problem Description. The finite volume method will now be applied to a more complex class of problems that involve two-dimensional (2D) radiative heat transfer in rectangular enclosures with isothermal, diffusely reflecting, gray walls. The enclosed medium is also assumed to be gray, and to scatter isotropically. Figure 6(A) shows a typical enclosure. The objective is to predict radiative heat transfer at the boundaries, and the medium temperature under the assumption of radiative equilibrium. To test the finite volume method, several benchmark problems will be solved. To simplify notation in the development that follows, the (x_1, x_2, x_3) coordinates will be used interchangeably with (x, y, z).

Discretization. Space is divided into control volumes of unit depth in the z direction and with boundaries defined by the solid lines in Fig. 6(A). Nodes, also called grid points, are located centrally in each interior volume as well as on the boundary. Each control volume face is divided into two panels with an integration point, such as 1, 2, 3, in Fig. 6(B), located at the center of each panel.

The angular orientation of intensity is defined by a polar angle θ, measured from the $x_3 = z$ axis, and the azimuthal angle ϕ, that lies in the (x, y) plane measured from the x axis. The solid angle ω^l is defined by the range $\theta^m_- \leq \theta \leq \theta^m_+$, $\phi^n_- \leq \phi \leq \phi^n_+$. All results shown are for N^θ equal increments of θ in the range $0 \leq \theta \leq \pi/2$ and for N^ϕ equal increments in ϕ in the range $0 \leq \phi \leq 2\pi$, where, for simplicity, N^ϕ was always chosen to be a multiple of 4.

To apply the general equations of section 2 to the grid system just described, some details must be decided. The central ray within ω^l, i.e., the one along s^l, is defined by (θ^m, ϕ^n), where each angle lies in the middle of its range (e.g., $\phi^n = (\phi_-^n + \phi^n)/2$). The path length $\bar{S}^l$ is taken as the distance from the integration point to the point where the $-s_l$ that passes through the integration point intersects the closest member of the set of surface that join the grid points. For example, in Fig. 6(B), for integration point $f = 1$

$$\bar{S}^l = S_{xy}^n / \sin \theta^m$$

where S_{xy}^n is the projection of $\bar{S}^l$ onto the x–y plane.

Intensities at u_1, u_2, etc. in Fig. 6(B) must be related to the nodal intensities by interpolation functions. This step requires great care. I_{u1}^l could, for example, be found by linear interpolation between I_N^l and I_P^l, but this would cause I_N^l to appear in the I_P^l equation. This is undesirable because the equation for I_P^l can no longer be solved by marching, and because such dependence of "downstream" intensities is inconsistent with the transportive properties of the differential equation for intensity. A better alternative is to find I_{u1} by extrapolation using I_P^l and I_S^l, but applying this practice at each integration point results in a computational molecule that connects I_P^l with as many as six upstream nodal intensities. While this is fairly easily accommodated, a simpler approach was used for the present application. When (for s^l upward and to the right) an interpolation point lies on a solid line in Fig. 6(B), linear interpolation between nodes was used. When it lies on a broken line, the interpolation value was taken as the value at the nearest "upstream" node on the line. According to this scheme I_{u1}^l and I_{u4}^l would be both approximated by I_P^l for $(s^l \cdot \mathbf{e}_j) \geq 0$, $j = 1, 2$. I_{u2}^l and I_{u3}^l would both be found by a linear interpolation involving I_P^l and I_W^l.

If linear interpolation or extrapolation were used to find all interpolation-point values, the solution error should decrease quadratically with mesh refinement, as for the one-dimensional problem, but it is well known (from experience in approximating fluid advection) that "wiggles" in the solution can occur. The interpolation practice adopted here is less likely to admit wiggles, but it is expected that errors due to spatial discretization will decrease with grid refinement at a rate that is between a linear and quadratic. These are features that will be examined when the benchmark problems are solved.

Solution Procedure. For intensities in those s^l directions that are upward to the right, the discrete equation for I_P^l has the form

$$a_P^l I_P^l = a_W^l I_W^l + a_S^l I_S^l + a_{SW}^l I_{SW}^l + b_P^l \qquad (27)$$

Given the boundary values of I^l along the left and bottom surfaces in Fig. 6(A), nodal values of I_P^l are found by direct substitution into equation (27), sweeping the domain in the positive x and y directions. With new incident intensities on the right boundary known, boundary conditions are applied to update the intensities leaving this surface, and an equation similar to equation (27) establishes nodal values for s^l in the range $(s \cdot \mathbf{e}_1) < 0$ and $(s \cdot \mathbf{e}_2) > 0$. Repeating this for all four sectors leads to a new I_P^l solution, for a given R_P distribution. R_P is then explicitly updated by calculating $I_{wP} = R_P$ from equation (13A).

For simplicity, the coefficients of equation (27) were recalculated each time the set of intensities associated with a particular ω^l was updated. The run times for the problems solved could be dramatically reduced by storing coefficients or even by using simple, computationally inexpensive approximations to the exponential terms. The intensities were stored in a four dimensional matrix, also for simplicity. For isotropic scattering, it is only necessary to store the complete I_P^l values at boundary nodes so that four-dimensional storage is not required.

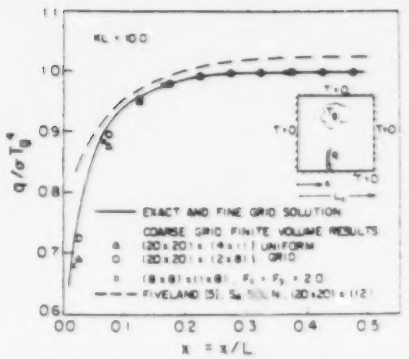
KL = 10.0
q/σT_g^4
x = x/L
EXACT AND FINE GRID SOLUTION
COARSE GRID FINITE VOLUME RESULTS
(20 x 20) x (4 x 1) UNIFORM
(20 x 20) x (2 x 8) GRID
FIVELAND [5], S6 SOLN., (20 x 20) x (12

Fig. 7 Nondimensional heat transfer on the wall of a square cavity containing an emitting gas at uniform temperature T_g and with zero wall temperature for an optically thick case ($KL = 10.0$)

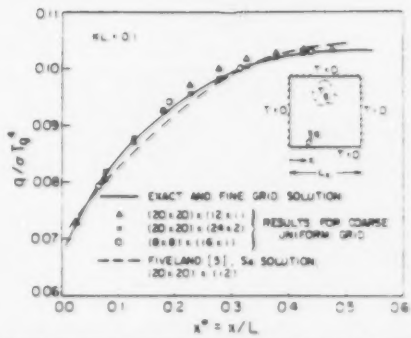
KL = 0.1
q/σT_g^4
x° = x/L
EXACT AND FINE GRID SOLUTION
RESULTS FOR COARSE UNIFORM GRID
FIVELAND [5], S6 SOLUTION
(20 x 20) x (12 x 1)
(20 x 20) x (24 x 2)
(8 x 8) x (16 x 1)

Fig. 8 Nondimensional heat transfer on the wall of a square cavity containing an emitting gas at uniform temperature T_g and with zero wall temperature for an optically thin case ($KL = 0.1$)

Comparison With One-Dimensional Solutions. The two-dimensional solution was applied first to the one-dimensional problem described in the last section, for a range of surface emissivities. As the grid was refined, the two-dimensional model converged to the same result as the one-dimensional model.

Problem 1: Black Enclosure With Emitting Medium. The first benchmark problem is the prediction of surface heat transfer in a square enclosure ($L_x = L_y = L$) with cold walls (at 0 K), which contains a gas at uniform temperature, T_g. The gas does not scatter ($\sigma^l = 0$) but does emit and absorb ($K \neq 0$). With the gas temperature known, the value of R in equation (10) is prescribed.

The local heat flux calculated to fall on the lower wall is plotted in Figs. 7 and 8 for the cases of strongly emitting medium ($KL = 10$) and weakly emitting medium ($KL = 0.1$), respectively. The "exact" solution was obtained by analytically integrating the radiation transfer equation for a given angle to the point of interest on the wall from the "upstream" wall, and then numerically integrating over all angles to find the local heat transfer. The present finite volume model could be made to agree with these exact results to any desired tolerance by refining the spatial and angular grids.

The S_6 discrete ordinates solution by Fiveland (1984) to this problem, using a (20×20) uniform spatial grid and with twelve quadrature points for the angular integrations are shown on Fig. 7 for $KL = 10$. Truelove (1987) was able to improve Fiveland's discrete ordinates solution by changing the

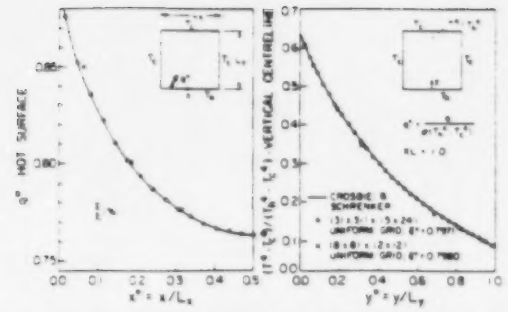

Fig. 9 Nondimensional heat transfer on the bottom, and centerline temperature distribution, in a square cavity with one heated wall enclosing a scattering gas with $\sigma^s L = 1.0$

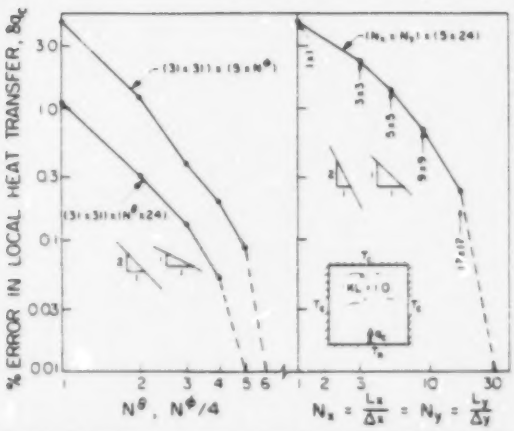

Fig. 10 Reduction in the error in local heat transfer at the center of the heated cavity wall with angle refinement (left side) and spatial refinement (right side)

quadrature points. Comparisons are made here with Fivelands solution, because the quadrature he used was not tuned to this particular class of problem. The present finite volume solutions for 20 uniform control volumes in each direction, $(N_x \times N_y) = (20 \times 20)$, and with a uniform angular discretization of $(N^\theta \times N^\phi) = (1 \times 4)$ and (2×8) are also shown in Fig. 7, and they give reasonable agreement with the exact solution. Reducing the spatial grid to (8×8) but using an expanding mesh that doubles the size of each successive control volume moving from the corners to the centerlines ($F_x = F_y = 2.0$ in Fig. 7), and using a uniform (1×8) angular discretization, results in excellent agreement with the exact solution. The solution time for $(20 \times 20) \times (2 \times 8)$ problem was 15 s on a MicroVax II computer.

Similar results appear in Fig. 8 for the $KL = 0.1$ case. The finite volume results obtained using all the coarse grids shown in Figs. 7 and 8 predict a total heat transfer on the bottom, which agrees with the exact values to within 0.8 percent.

The results for this sample problem illustrate that the finite volume method converges to the exact solution as the angular and spatial grids are refined, and that predictions of good accuracy can be obtained on quite coarse grids.

Problem 2: Two-Dimensional Heat Transfer in an Enclosure With One Hot Wall. The second two-dimensional problem involves radiative exchange in rectangular enclosures with the left, top, and right wall temperatures set to T_c and the bottom wall set a higher temperature T_h. The medium scatters

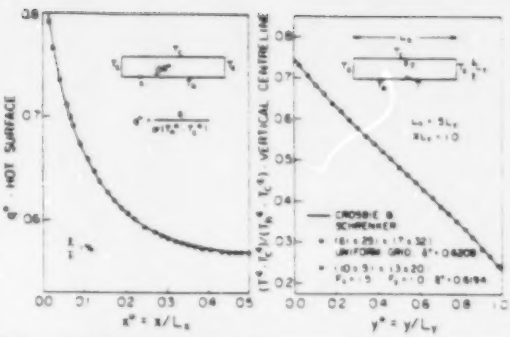

Fig. 11 Nondimensional heat transfer on the bottom, and centerline temperature distribution, in a 5:1 aspect ratio cavity enclosing a scattering gas with $\sigma^s L_y = 1.0$

isotropically and is assumed to be in radiative equilibrium. The objective is to predict the heat transfer that leaves the bottom surface as well as the temperature of the medium. Careful solutions to this problem have been reported by Crosbie and Schrenker (1984) for a range of cavity aspect ratios and scattering coefficients. Comparisons with finite volume predictions are presented here for three cases.

The "exact" (Crosbie and Schrenker, 1984) dimensionless local heat transfer q^* leaving the hot wall and temperature distribution along a vertical line in the center of a square enclosure are plotted as solid lines in Fig. 9 for a medium with $\sigma^s L = 1.0$. Application of the finite volume method with a very fine mesh $(N_x \times N_y) \times (N^\theta \times N^\phi) = (31 \times 31) \times (5 \times 24)$ is shown to give almost exact agreement (local heat fluxes agree to well within 0.1 percent). Use of a coarse $(8 \times 8) \times (2 \times 12)$ grid, such as would be of more practical interest, also yields excellent accuracy, with an average heat transfer $\bar{q}^*$ that is only 0.1 percent too high. To obtain a solution on this grid, in which the absolute value of the heat transfer on all walls changed by less than 0.05 percent between R-updated cycles, required eight cycles and 32 s on a MicroVax II computer.

As previously discussed, it is important to know how quickly the solution error decreases with grid refinement. To perform this evaluation, the error in the local heat transfer at the center of the hot wall ($x/L = 0.5$) was examined. Retaining (32×32) uniform control volumes, fixing N^ϕ at 24, and varying N^θ, Fig. 10 shows that the error diminishes quadratically with N^θ. Similarly, for N^θ fixed at 5, increasing N^ϕ results in a quadratic decrease in error. For a fine angular grid (5×24) and with refinement of a uniform spatial grid, the error is seen in Fig. 10 to decrease somewhere between linear and quadratic with increasing $N_x = N_y$. These results are in agreement with the expectations that were previously discussed.

For an enclosure with an aspect ratio of $L_x/L_y = 5$, the "exact solution" of Crosbie and Schrenker (1984) and a fine-grid $(61 \times 25) \times (7 \times 32)$ finite volume solution are plotted in Fig. 11 for $\sigma^s L_y = 1.0$. The finite volume predictions of heat flux agree with the exact values to within 0.2 percent, and the temperature is also closely predicted. Figure 11 also shows that a much coarser grid $(10 \times 5) \times (3 \times 20)$, where the control volumes widths in the x direction expand by a factor of 1.5 moving from the outer walls toward the center ($F_x = 1.5$), yields virtually identical results, with an average heat transfer $(\bar{q}^*)$ just 0.2 percent below the fine grid prediction. The prediction on the $(10 \times 5) \times (3 \times 20)$ grid required five R-update cycles and 17.6 s to achieve a total absolute value of heat transfer on the boundaries that changed less than 0.05 percent between cycles.

The last test problem described in this paper has been specifically chosen to demonstrate that, as mentioned earlier,

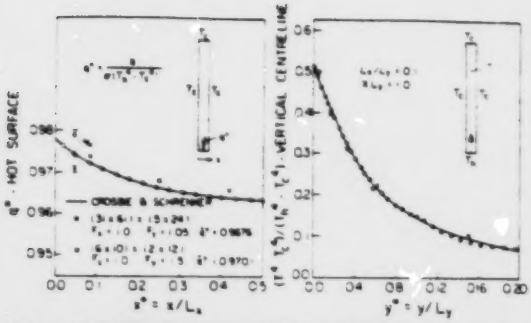

Fig. 12 Nondimensional heat transfer on the bottom, and centerline temperature distribution, in a 1:10 aspect ratio cavity enclosing a scattering gas with $\sigma^2 L_y = 1.0$

profile wiggles can occur under adverse conditions. Results for a cavity with $\sigma^2 L_y = 1.0$ and $L_x/L_y = 10$ are compared to the predictions of Crosbie and Schrenker in Fig. 12. Calculations on a fine $(31 \times 61) \times (5 \times 24)$ grid, with uniform control volumes in the x direction and with volumes in the y direction that increase by expansion factor of $F_y = 1.05$, yielded local heat transfer predictions that are in excellent agreement with Crosbie and Schrenker (Fig. 12). The predicted centerline temperature near the bottom wall (right side of Fig. 12) is also very accurate but, when the aspect ratio of the control volumes become large in the center to top of the cavity, the predicted temperatures oscillate (or wiggle) slightly about the profile of Crosbie and Schrenker. This "wiggle" is a consequence of the assumed linear profile of I' between nodes in Fig. 6(B), and is analogous to the wiggles that are often tolerated when a linear profile between nodes is used in the approximation of the advective transport terms in fluid flows. Such wiggles can be overcome (Roache, 1972) at the expense of accuracy by adopting a simple "upwind" approximation, or by using a more elaborate discretization.

Figure 12 also shows predictions using a coarse $(6 \times 10) \times (2 \times 12)$ mesh that has uniform spacing in the x direction and expands rapidly ($F_y = 1.5$) in the y direction away from the heated wall. This grid yields good temperature predictions, and heat transfer rates that are within 0.3 percent of exact values.

Summary and Discussion

A new finite volume method has been proposed for the prediction of radiative heat transfer that can be implemented on nonorthogonal grids of the type employed to predict complex fluid flows. The theory is advanced for an absorbing-emitting and scattering gray medium in an enclosure with gray diffuse walls, but extensions to a broad bandwidth model and to include walls with other reflective properties are straightforward. For strongly participating media, the method captures the diffusion approximation to the radiant heat transfer equations. The method ensures that the intensity in a given direction, as well as the net radiative heat transfer, satisfy the global conservation constraints. The approximations of the solid-angle integrals also prevent any occurrence of the "ray effects" encountered in discrete ordinate methods (Viskanta, 1987). The method also appears to be the first that shares the philosophy of, and can use the same nonorthogonal boundary fitted mesh as, modern methods for computing fluid flows and that also converges with grid refinement to the exact solution of the radiation transport equation.

The authors are indebted to anonymous reviewers for pointing out that it may be undesirable for a radiation grid to be congruent with the fluid flow grid since the need for grid refinement may occur in different regions. Such situations are already encountered when the internal energy equation is solved over extensive regions of the flow in which the temperature is nearly constant, but in these regions a fine grid is needed to compute the fluid flow. It is common practice in such cases to use the same grid for both the fluid flow and heat transfer for the sake of simplicity. Similarly, for fluid flow and radiation different grids could certainly be used, but at the expense of complexity. Even if different grids were used, it is still desirable to use a philosophically consistent method.

The method has been demonstrated for a one-dimensional problem, and several simple two-dimensional problems, for which benchmark solutions and other approximate solutions are available. The method is shown to yield good accuracy on coarse grids, and errors due to the discrete representations of the continuous equations reduce rapidly with grid refinement.

Acknowledgments

This work was supported by a contract, negotiated through the Unsolicited Proposal Program, from the Combustion and Carbonization Research Laboratory of the Energy Resources Laboratory, CANMET, which is part of the Energy Mines and Resources Department of the Canadian Federal Government. The authors gratefully acknowledge the support and assistance of the Scientific Advisor, Mr. Pat Hughes. Our thanks also to Professor K.G.T Hollands of the Mechanical Engineering Department at the University of Waterloo for his encouragement, criticism and enthusiasm. Professor R. Viskanta has also provided valuable comments.

References

Crosbie, A. L., and Schrenker, R. G., 1984, "Radiative Transfer in a Two-Dimensional Rectangular Medium Exposed to Diffuse Radiation," *J. Quant. Spectrosc. Radiat. Transfer*, Vol. 31, pp. 339–372.

Fiveland, W. A., 1984, "Discrete-Ordinates Solutions of the Radiation Transport Equation for Rectangular Enclosures," ASME JOURNAL OF HEAT TRANSFER, Vol. 106, pp. 699–706.

Heaslet, M. A., and Warming, R. F., 1965, "Radiative Transport and Wall Temperature Slip in Absorbing Planar Medium," *Int. J. Heat Mass Transfer*, Vol. 8, pp. 979–994.

Roache, P. J., 1972, *Computational Fluid Dynamics*, Hermosa Publ., Albuquerque, NM.

Siegel, R., and Howell, J. R., 1981, *Thermal Radiation Heat Transfer*, Hemisphere Publishing Corp., New York.

Truelove, J. S., 1987, "Discrete Ordinate Solutions of the Radiation Transport Equation," ASME JOURNAL OF HEAT TRANSFER, Vol. 109, pp. 1048–1051.

Viskanta, R., 1984, "Radiative Heat Transfer," *Fortschrift der Verfahrenstechnik*, Vol. 22A, pp. 51–81.

Viskanta, R., and Mengüç, M. P., 1987, "Radiation Heat Transfer in Combustion Systems," *Prog. Energy Combust. Sci.*, Vol. 13, pp. 97–160.

11 Appendix C - Prediction of Radiant Exchange in Cylindrical Enclosures with the Finite-Volume Method

Paper In Press
J. Thermophysics & Heat Transfer.

PREDICTION OF RADIATIVE TRANSFER IN CYLINDRICAL ENCLOSURES WITH THE FINITE VOLUME METHOD

by

E.H. CHUI[1], G. D. RAITHBY[2]

University of Waterloo, Waterloo, Ontario

P. M. J. HUGHES[3]

Energy Research Laboratories, CANMET, Ottawa, Ontario

March 1991

---

1. PhD (1990), Dept. Mechanical Engineering, University of Waterloo, Waterloo, Ontario, Canada, N2L 5J8

2. Professor, Dept. Mechanical Engineering, University of Waterloo, Waterloo, Ontario, Canada, N2L 5J8

3. Research Scientist, Energy Research Laboratories, CANMET, 555 Booth St., Ottawa, Ontario, Canada, K1A 0G1

ABSTRACT

This paper shows how the finite volume method can be implemented to solve three dimensional radiation problems in cylindrical enclosures. The medium is considered to be gray, and absorption, emission and either isotropic or non-isotropic scattering are included. For the special case of axisymmetric radiation, a mapping is described that yields a complete solution by solving for the intensity in a single azimuthal direction. The method is shown to rapidly converge to the solution of the radiation transfer equation as the spatial and directional grid is refined. Results from the solution of axisymmetric benchmark problems show that the method is stable, accurate, and computationally efficient.

NOMENCLATURE

A	area, m^2
D_f^l	direction cosine to surface normal integrated over ω^l (Eq. 3)
$I(\vec{R}, \vec{s})$	radiant intensity, $W/(m^2\ sr)$
$\bar{I}\ (\vec{R}, \vec{s})$	inscattering term at $\vec{R}$ in direction $\vec{s}$ (Eqs.(2) and (8B))
$\bar{I}^l$	inscattering term for solid angle ω^l (Eq. (8A))
I_b	blackbody intensity, $W/(m^2\ sr)$
I_f^l	intensity at integration point f within ω^l, $W/(m^2\ sr)$
I_P^l	intensity at node P within ω^l, $W/(m^2\ sr)$
I_{uf}^l	upstream intensity for integration point f within ω^l, $W/(m^2\ sr)$
K_a	absorption coefficient, m^{-1}
N_r, N_z	number of control volumes in the r and z directions respectively
N_θ, N_ϕ	number of control volumes in polar (θ) and azimuthal (ϕ) directions
$\vec{n}$	outward unit normal to a surface
q	radiant heat flux, W/m^2
$\vec{q}$	radiant heat flux vector, W/m^2

r	radius in the (x,y) plane, m
$\bar{R}$	position vector
R	the intensity source function (Eq. (6))
$\bar{s}$	unit vector in direction of intensity
S	path length, m
T	temperature, K
V	volume, m^3
x', y', z'	directions parallel to the x,y and z axes (Fig. 1)

GREEK SYMBOLS

ε	surface emissivity
θ	polar angle measured from the z direction
κ	extinction coefficient (Eq. (6))
σ	Stefan-Boltzmann constant
σ_s	scattering coefficient, m^{-1}
ϕ	azimuthal angle measured from the radial direction (Fig. 1)
φ	azimuthal angle measured from the x' axis (Fig. 1)
Φ	scattering phase function, Eq.(2)
$\bar{\Phi}$	new variable for phase function, Eq. (8B)

ψ	scattering angle between incident and scattered directions
ω_s	scattering albedo
ω	solid angle, sr

SUPERSCRIPTS AND SUBSCRIPTS

*	refers to a dummy variable or a nondimensional quantity
b	refers to blackbody
B	refers to the boundary
f	refers to integration point f on the surface of a control volume
g	association with medium
l	associated with solid angle ω^l
l^-, l^+	denote the boundaries of solid angle ω^l
P	refers to nodal point P
r	refers to the radial direction
u	refers to an upstream position
w	refers to the boundary

INTRODUCTION

Axisymmetric radiative transfer in cylindrical enclosures has been studied by a substantial number of researchers, and almost every radiation model has been applied to this type of problem (e.g. Monte Carlo Method (Perlmutter and Howell[1]), Flux Method (Lowes et al[2]), Zone Method (Steward and Tennankora[3]), Discrete Ordinates Method (Fiveland[4]), Galerkin Finite Element Method (Fernandes and Francis[5]), and Spherical Harmonic Method (Mengüç and Viskanta[6]). As an additional small sample of the extensive recent literature on this problem, the reader may consult Jamaluddin and Smith[7], Yucel and Williams[8], and Carvalho et al[9]. There is such widespread interest in axisymmetric radiation because it allows the performance of radiation models to be assessed on simple problems, and because radiation in boilers, furnaces and combustors can sometimes be modelled as axisymmetric.

From recent reviews by Howell[10] and Viskanta and Mengüç[11], it is evident that no single radiation model can be regarded as the best for all problems. In the context of modelling reacting flows, the flux methods are often adopted because of their compatibility with the numerical algorithms used for solving the fluid dynamics equations. The spherical harmonic (P_3) method and the discrete ordinate (S_N) method are generally more accurate than the simple four or six flux models, but they too have shortcomings[6,12]. The need for better models still exists.

Raithby and Chui[13] recently proposed a Finite Volume Method (FVM) that shares the same philosophy and grid as the finite volume techniques currently used in predicting fluid flow and convective heat transfer. In this method the computational domain is subdivided into discrete (finite) volumes and direction is subdivided into discrete solid angles. The radiation transfer equation (RTE) integrated over both a discrete volume and solid angle serves as the starting

point.

Although this method has many similarities to the Discrete Ordinates Method, it does not use the quadrature that gives rise to the discrete ordinates. The Discrete Ordinates Method is also usually applied by approximating derivatives in the RTE by finite differences, although Fiveland[14] recently started from the volume-integrated equation. By starting with the integral of the RTE over both discrete angles and volumes, the FVM avoids "ray effects[15]" by guaranteeing exact global conservation of radiant energy. Total inscattering is also exactly balanced by total outscattering for each finite volume for any phase function, whereas the Discrete Ordinates Method has, to the authors' knowledge, only been applied on Cartesian and circular-cylinder computational grids, the FVM was designed for use on virtually any of the grid types that are currently used to compute fluid flow.

There are, of course, many ways to implement a FVM. The particular implementation of the FVM used by Raithby and Chui[13] exactly captured the diffusion limit for strongly participating media, and reduced non-physical 'wiggles' in the solution, by use of a special discretization approximation. Although somewhat algebraically complex, the method was shown to be stable, accurate, and computationally efficient for rectangular enclosures.

In this paper, a particular implementation of the general FVM will be described that applies to spatially three-dimensional (3D) radiation problems on a circular-cylinder mesh. The medium may be absorbing, emitting, and isotropically or anisotropically scattering. This method is applied to axisymmetric problems involving cylindrical enclosures of finite length. The contributions of this paper include,

1. a new discretization scheme for 3D problems,

2. a less restrictive treatment of scattering than previous methods,

3. a mapping that simplifies the solution of axisymmetric problems, and

4. a demonstration of performance of the method for axisymmetric problems.

The gray gas approximation is implicitly used throughout the present paper.

It may be helpful to explain why a general 3D model is described in a paper where the focus is on axisymmetric problems. The main reason is that it is simpler to draw the diagrams and explain the method for the general 3D case, and all the material presented is needed for the axisymmetric problem. The second reason is that the 3D model applies to any problem for which the mesh is orthogonal, so may be itself of interest. Results for the general 3D model have not been provided to avoid diffusing the focus of this paper.

GOVERNING EQUATION

The basis for quantitative studies of radiative heat transfer is the Radiative Transfer Equation (RTE). For a gray medium, the RTE has the form (see Siegel and Howell[16]):

$$\frac{dI(\vec{R}, \vec{s})}{ds} = -(K_a + \sigma_s) I(\vec{R}, \vec{s}) + K_a I_b(\vec{R}) + \sigma_s \bar{I}(\vec{R}, \vec{s}) \qquad (1)$$

This equation describes the increase in radiant intensity $I(\vec{R}, \vec{s})$ at spatial location $\vec{R}$ over the path length ds in the direction of unit vector $\vec{s}$, as shown in Fig. 1. The first and third terms on the right side of Eq. (1) represent the effects of absorption and emission respectively. 'Outscattering', term two, reduces the intensity in the $\vec{s}$ direction, while 'inscattering', term four, redirects energy from other directions into the $\vec{s}$ direction. The inscattering term is defined by

$$\sigma_s \bar{I}(\vec{R}, \vec{s}) = \frac{\sigma_s}{4\pi} \int_{4\pi} I(\vec{R}, \vec{s}') \Phi(\vec{s}, \vec{s}') d\omega' \qquad (2)$$

where the fraction of the intensity $I(\vec{R}, \vec{s}')$ in direction $\vec{s}'$ that is scattered into direction $\vec{s}$ is defined by the phase function $\Phi(\vec{s}, \vec{s}')$.

FINITE VOLUME SOLUTION OF THE RTE

Discrete Energy Balance

Equation (1) expresses the conservation of radiant energy in direction $\vec{s}$ over an infinitesimal control volume and within an infinitesimal solid angle. The FVM yields an approximate (discrete) solution to this equation which converges to the solution as Eq. (1) as the computational grid is refined.

To implement the method, the computational domain is divided into volumes by a computational mesh. Figures 2a and b show a typical subdivision for a cylindrical enclosure. Furthermore direction is subdivided into discrete solid angles, ω^l, with each one defined by a particular range of angles θ and ϕ in Fig. 1. The intensity within the volume centered at P and within ω^l is represented by a single value, I_p^l. The equation for I_p^l is the RTE integrated over the volume V_p and over ω^l.

The control volume centered at *P* in Fig. 2 is redrawn in Fig. 3a. The "integration points" f = 1, 2, ..., 6 lie on the volume faces, at the intersection of the co-ordinate surfaces that pass

through the nodes. The radiant energy Q_f^l, that lies within ω^l and that crosses face f of area A_f, is approximated by

$$Q_f = I_f^l A_f \int_{\omega^l} \vec{s} \cdot \vec{n}_f \, d\omega = I_f^l A_f D_f^l \tag{3}$$

where I_f^l and $\vec{n}_f$ (the unit surface normal) at point f are used to approximate their values across the control volume surface A_f. D_f^l is evaluated analytically.

Integration of the RTE over V_p and ω^l (see Raithby and Chui[13]) results in the conservation constraint that the net radiant flux leaving through the surfaces of V_p within ω^l equals the net "generation" of radiant energy within V_p and ω^l by emission, absorption, inscattering and outscattering. Approximating the generation term using nodal-point values of intensity, this conservation balance becomes

$$\sum_{f=1}^{6} Q_f = \sum_{f=1}^{6} I_f^l A_f D_f^l = \left[K_p I_{b,p} - (K_p + \sigma_{s,p}) I_p^l + \sigma_{s,p} \overline{I}_p^l \right] V_p \omega^l \tag{4}$$

For this to be a useful equation for I_p^l, the integration-point values I_f^l must be related to nodal point values of I^l. This is discussed in the next section.

Evaluation of I_f^l

If the intensity I_{uf} at some point uf that lies distance S "upstream" of f along the direction

Using mass conservation (Eq. (9)) to replace the second term on the LHS of Eq. (35) by a surface integral, and rearranging the equation, the desired equation for P_i is obtained

$$\int_{\forall_P} \rho u_i d\forall = P_i = M_P \frac{dR_i}{dt} + \int_{S_P} \rho(r_i - R_i)(\vec{V} - \vec{W}) \cdot \hat{n}_P dS \tag{36}$$

which can be rewritten as

$$P_i = M_P u_i^{COM} + \int_{S_P} (r_i - R_i) \dot{m}''_P dS \tag{37}$$

Equation (37) achieves the first goal of finding the expression for particle momentum in terms of the velocity of its centre of mass. There are some interesting, and perhaps unexpected, features already in this equation. For example, if $\dot{m}''_P > 0$ on the back of the particle (where $r_i < R_i$) and $\dot{m}_P = 0$ elsewhere on its surface, and if the velocity throughout the particle is uniform at V_{iP}, Eq. (37) shows that $V_{iP} < u_i^{COM}$ (the particle velocity is less than the velocity of its centre of mass). This results because the unsymmetrical mass loss causes the centre of mass to move forward relative to the velocity of the particle.

Now attention is turned to expressing Newton's law for the particle in terms of centre of mass quantities. Following exactly the steps that gave rise to Eq. (19), except that the integration is over $\forall_P$

$$\begin{aligned} \left(\frac{d}{dt}\left(\int_{\forall_P} \rho u_i d\forall\right) \equiv \frac{dP_i}{dt}\right) &= -\int_{S_P} \rho u_i (\vec{V} - \vec{W}) \cdot \hat{n}_P dS \\ &- \int_{S_P} (p\hat{n}_P \cdot \hat{e}_i + \tau_{ji}\hat{n}_P \cdot \hat{e}_j) dS + \int_{\forall_P} f_i^B d\forall \end{aligned} \tag{38}$$

or

$$\frac{dP_i}{dt} = -\int_{S_P} u_i \dot{m}''_P dS + F_{i,P}^D + F_P^B \tag{39}$$

Differentiating Eq. (37)

$$\frac{dP_i}{dt} = M_P \frac{du_i^{COM}}{dt} + u_i^{COM} \frac{dM_P}{dt} + \frac{d}{dt} \int_{S_P} \rho(r_i - R_i)(\vec{V} - \vec{W}) \cdot \hat{n}_P dS \tag{40}$$

Substituting the expression for $\frac{dP_i}{dt}$ from Eq. (38) into Eq. (40), and using mass conservation, yields the desired equation

$$M_P \frac{du_i^{COM}}{dt} = \int_{S_P} \rho(u_i^{COM} - u_i)(\vec{V} - \vec{W}) \cdot \hat{n}_P dS$$

$$+ \frac{d}{dt} \int_{S_P} \rho(r_i - R_i)(\vec{V} - \vec{W}) \cdot \hat{n}_P dS + F_{i,P}^D + F_{i,P}^B$$

or

$$M_P \frac{du_i^{COM}}{dt} = \int_{S_P} (u_i^{COM} - u_i) \dot{m}_P'' dS - \frac{d}{dt} \int_{S_P} (r_i - R_i) \dot{m}_P'' dS + F_{i,P}^D + F_{i,P}^B \qquad (41)$$

The first term on the RHS of Eq. (41) is the rocket effect. The second term accounts for movement of the centre of mass due to non-uniform $\dot{m}_P''$. Both these terms are usually excluded when the particle momentum equation is written. They disappear if $\dot{m}_P'' = 0$, but also if both $\dot{m}_P''$ is uniform over the surface and u_i is constant at u_i^{COM}. Evaporation will rarely be truly uniform, so the presence of the added terms must be kept in mind. For a particle whose mass varies with time, it is also important to note that the particle mass, M_P, on the LHS of Eq. (41) correctly lies outside the time derivative; the left side is often recorded in textbooks $\frac{d}{dt}(M_P u_i^{COM})$ without the statement that M_P has been assumed constant.

3.4 Particle Equation in Cylindrical Co-ordinates

For the present problems, the first two terms on the RHS of Eq. (41) will likely be small, but they must be neglected in any case unless the details of the distribution of $\dot{m}_P''$ can be estimated. With these approximations, Eq. (41), written in vector form, becomes

$$M_P \frac{d\vec{V}^{COM}}{dt} = \vec{F}_P^D + \vec{F}_P^B \qquad (42)$$

The conversion of this equation to circular cylinder co-ordinates is straightforward, but this will be shown here because the results are required for problems of current interest. Using the nomenclature in Fig. 8

$$\vec{V}^{COM} = u_r^{COM} \hat{e}_r + u_\theta^{COM} \hat{e}_\theta + u_z^{COM} \hat{e}_z \qquad (43)$$

where u_r, u_θ and u_z are the radial, circumferential and axial velocity components.

The derivative in Eq. (43) becomes

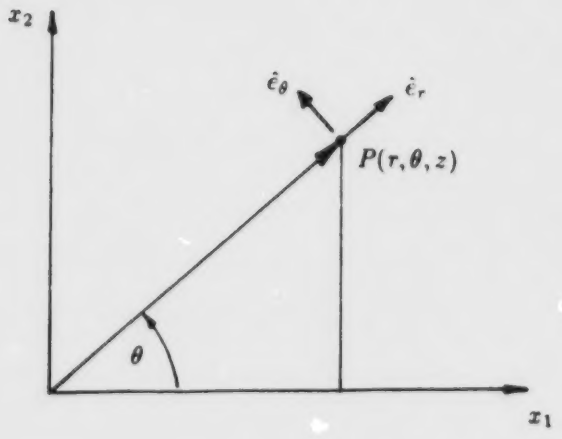

Figure 8: Circular cylinder co-ordinate system.

$$\frac{d\vec{V}^{COM}}{dt} = \left[\hat{e}_r \frac{du_r^{COM}}{dt} + \hat{e}_\theta \frac{du_\theta^{COM}}{dt} + \hat{e}_z \frac{du_z^{COM}}{dt} + u_r^{COM} \frac{d\hat{e}_r}{dt} + u_\theta^{COM} \frac{d\hat{e}_\theta}{dt}\right] \quad (44)$$

The transformation between $(\hat{e}_r, \hat{e}_\theta, \hat{e}_z)$ and $(\hat{e}_1, \hat{e}_2, \hat{e}_3)$ is

$$\begin{Bmatrix} \hat{e}_r \\ \hat{e}_\theta \\ \hat{e}_z \end{Bmatrix} = \begin{bmatrix} cos\theta & sin\theta & 0 \\ -sin\theta & cos\theta & 0 \\ 0 & 0 & 1 \end{bmatrix} \begin{Bmatrix} \hat{e}_1 \\ \hat{e}_2 \\ \hat{e}_3 \end{Bmatrix}$$

which permits the derivatives of $\hat{e}_r$ and $\hat{e}_\theta$ to be evaluated. Equation (44) then becomes

$$\frac{d\vec{V}^{COM}}{dt} = \left(\frac{du_r}{dt} - \frac{u_\theta^2}{r}\right)\hat{e}_r + \left(\frac{du_\theta}{dt} + \frac{u_r u_\theta}{r}\right)\hat{e}_\theta + \frac{du_z}{dt}\hat{e}_z \quad (45)$$

Splitting Eq. (42) into its components

$$M_P\left(\frac{du_r}{dt} - \frac{u_\theta^2}{r}\right) = F_{r,P}^D + F_{r,P}^B \quad (46)$$

$$M_P\left(\frac{du_\theta}{dt} + \frac{u_r u_\theta}{r}\right) = F_{\theta,P}^D + F_{\theta,P}^B \quad (47)$$

$$M_P\frac{du_z}{dt} = F_{z,P}^D + F_{z,P}^B \quad (48)$$

(49)

3.5 Source of Momentum from Moving Particles

The rate of i-momentum transfer from one particle to the gas is, from Eq. (21) or Eq. (24), $\dot{m}_P u_{i,P-surf}$, where subscript $_{P-surface}$ denotes the particle surface. Following the steps leading to Eq. (11) for mass, and referring to Fig. 3.

$$\left\{ \begin{array}{l} \text{Total Rate of Transfer of} \\ i - \text{Momentum to gas within} \\ \forall \text{ From One Particle in } \Delta t \end{array} \right\} = \int_{s_1(t)}^{s_2(t)} \frac{\dot{m}_P u_{i,P-surf} \dot{N}_P}{|\vec{V}_P|} ds \tag{50}$$

Adding the contributions from all the particle paths crossing the control volume, the last two terms in Eq. (26) become

$$\sum_P \left[\dot{m}_P (u_{i,P-surf} - u_{i,k}) - F^D_{i,P} \right] = \sum_k \left\{ \int_{s_1(t)}^{s_2(t)} \left[\dot{m}_P (u_{i,P-surf} - u_{i,k}) - F^D_{i,P} \right] \frac{\dot{N}_P}{|\vec{V}_P|} ds \right\}_{path k} \tag{51}$$

For the special case of a stationary control volume, the convection term in Eq. (50) (the other terms in Eq. (51) are similarly treated) can be approximated by

$$\left\{ \begin{array}{l} \text{Total Rate of Transfer of} \\ i - \text{Momentum to gas within} \\ \forall \text{ From One Particle in } \Delta t \end{array} \right\} \approx (M_{P,1} - M_{P,2}) \bar{u}_{i,P-surf} \dot{N}_P \tag{52}$$

where $\bar{u}_{i,P-surf}$ is the average i-velocity component at the particle surface during its flight from points 1 to 2 in Fig. 4A. The following approximation is often made, but is <u>INCORRECT</u>:

$$\left\{ \begin{array}{l} \text{Total Rate of Transfer of} \\ i - \text{Momentum to gas within} \\ \forall \text{ From One Particle in } \Delta t \end{array} \right\} \approx \left[(M_P u_{i,P-surf})_1 - (M_P u_{i,P-surf})_2 \right] \dot{N}_P \tag{53}$$

For the special case in Fig, 4B, where the particle is traced from A to B but spends only a portion of its time in the volume $\forall$,

$$\left\{ \begin{array}{l} \text{Total Rate of Transfer of} \\ i - \text{Momentum to gas within} \\ \forall \text{ From One Particle in } \Delta t \end{array} \right\} \approx (M_{P,A} - M_{P,B}) \bar{u}_{i,P-surf} \dot{N}_P \frac{(t_2 - t_1)}{(t_B - t_A)} \tag{54}$$

4 ENERGY CONSERVATION

4.1 Differential Equation of Energy Conservation

The energy $\hat{e}$ of a material, per unit mass, has three components: internal (e), kinetic ($\frac{1}{2}\rho V^2$) and potential (gZ).

The conservation equation for $\hat{e}$ for a differential volume is (Bird et al., 1960)

$$\frac{\partial}{\partial t}(\rho\hat{e}) = -\frac{\partial}{\partial x_j}(\rho u_j \hat{e}) - \frac{\partial}{\partial x_j}(q_j^C + q_j^R) - \frac{\partial}{\partial x_j}(pu_j + u_i\tau_{ji}) + f_j^B u_j + \dot{S}''' \quad (55)$$

This equation states that the rate of increase of energy in the differential volume equals the advected transport of $\hat{e}$ into the volume, plus the rate of convective and radiative heat transfer to the volume, plus the work done by surface forces on the control volume, plus the work done by body forces, plus the rate of internal generation of energy, $\dot{S}'''$.

Each term is a per-unit-volume quantity. This equation applies locally to a solid, liquid or gas.

4.2 Gas Energy Equation

The rate of increase of energy within the gas volume $\forall_G$ is, by Leibnitz rule,

$$\frac{d}{dt}\int_{\forall_G} \rho\hat{e}d\forall = \int_{\forall_G} \frac{\partial}{\partial t}(\rho\hat{e})d\forall + \int_{S_{OG}+S_I} \rho\hat{e}\vec{W}\cdot\hat{n}dS \quad (56)$$

Figure 9 shows the boundaries of the control region. Substituting Eq. (55) into (56) to eliminate the first term on the RHS, and using Gauss' Theorem to convert volume integrals to surface integrals,

$$\frac{d}{dt}\int_{\forall_G} \rho\hat{e}d\forall = -\int_{S_{OG}+S_I} \rho(\hat{e}+\frac{p}{\rho})(\vec{V}-\vec{W})\cdot\hat{n}dS - \int_{S_{OG}+S_I} (\vec{q}^C + \vec{q}^R)\cdot\hat{n}dS$$
$$- \int_{S_{OG}+S_I} p\vec{W}\cdot\vec{n}dS - \int_{S_{OG}+S_I} u_i\tau_{ji}n_j dS + \int_{\forall_G} f_j^B u_j d\forall + \int_{\forall_G} \dot{S}''' d\forall \quad (57)$$

The total heat gain by the gas by convection and radiation, see Fig. 9, is defined as

$$-\int_{S_{OG}+S_I} (\vec{q}^C + \vec{q}^R)\cdot\hat{n}dS = -\dot{Q}_{OG}^C - \dot{Q}_I^C - \dot{Q}_G^R$$
$$= -\dot{Q}_{OG}^C + \sum_P \dot{Q}_P^C - \dot{Q}_G^R \quad (58)$$

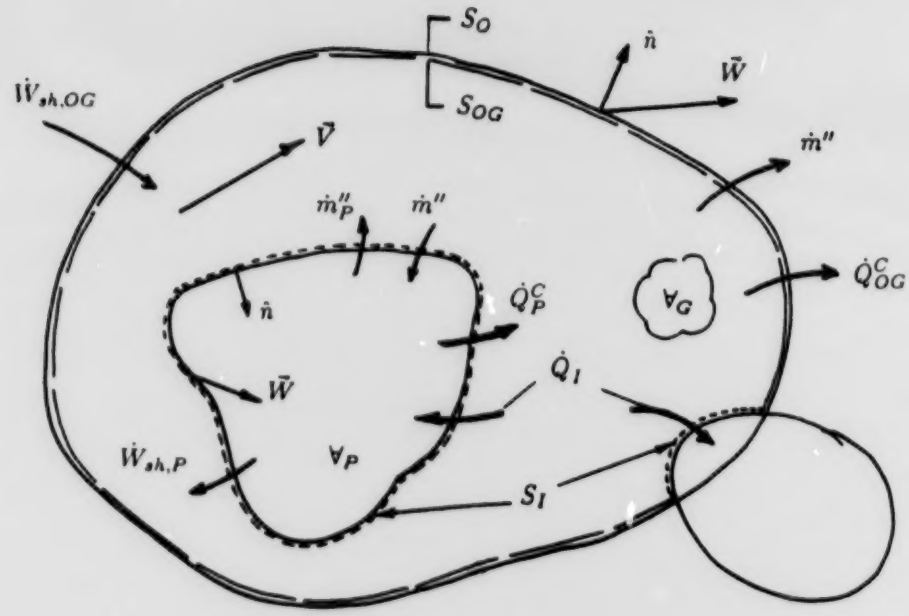

Figure 9: Notation for energy balance on gas.

Note that $\dot{Q}_{OG}$ and $\dot{Q}_I$ are defined as positive if heat is lost by the gas. $\dot{Q}_P$ is positive when heat is lost by the particle, which represents a gain by the gas. $\dot{Q}^R_G$ is the net loss of internal energy by the gas through conversion to radiant energy.

Term 3 on the RHS of Eq. (57) is the work done at the control volume surfaces on the gas by compression (the $-p\,d\forall$ work of thermodynamics). Term 4 is the total work done by boundary shear forces at the outer gas boundary, and at all the particle boundaries inside $\forall$. This is written as

$$-\int_{S_{OG}+S_I} u_i \tau_{ji} n_j dS = \dot{W}_{sh,OG} + \sum_P \dot{W}_{sh,P} \tag{59}$$

The summation is over all particles that are in, or partly in, S_0, so $\dot{W}_{sh,P}$ is the total work done on the gas by the surface shear stresses on the portions of all particles P that lie within S_0. Term 5 of Eq. (57) is the work done by body forces other than gravity (the effect of work done by gravity has been converted to the potential energy term contained in $\hat{e}$ on the LHS of Eq. (57).

$$\int_{\forall_G} f^B_j u_j d\forall = \dot{W}^B_G \tag{60}$$

Term 6 is the total generation of internal energy.

$$\int_{\forall_G} \dot{S}''' d\forall = \dot{S}_G \tag{61}$$

Term 1 on the RHS of Eq. (57) is the advective transport of enthalpy $h = (e+p/\rho)$ plus potential and kinetic energy into the gas through $S_{OG} + S_I$, and can be written as

$$-\int_{S_{OG}+S_I}(\hat{e} + \frac{p}{\rho})\rho(\vec{V}-\vec{W})\cdot\hat{n}dS = -\int_{S_{OG}}(\hat{e}+\frac{p}{\rho})\dot{m}''dS - \int_{S_I}(\hat{e}+p/\rho)\dot{m}''dS \quad (62)$$

$$= -\int_{S_{OG}}(\hat{e}+p/\rho)\dot{m}''dS + \sum_P \int_{S_P}(\hat{e}+\frac{p}{\rho})\dot{m}''_P dS \quad (63)$$

where the summation is over all particles that have surface area within S_O, and S_P is the surface area of particle P that lies within S_O in Fig. 9.

Introducing all this notation into Eq. (57) yields the complete energy equation

$$\frac{d}{dt}\int_{\forall_G}\rho\hat{e}d\forall = -\int_{S_{OG}}(\hat{e}+\frac{p}{\rho})\dot{m}''dS - \dot{Q}^C_{OG} - \int_{S_{OG}} p\vec{W}\cdot\hat{n}dS + \dot{W}_{sh,OG}$$
$$+ \dot{W}^B_G + \dot{S}_G - \dot{Q}^R_G + \sum_P\left\{\int_{S_P}(\hat{e}+\frac{p}{\rho})\dot{m}''_P dS + Q^C_P + \dot{W}_{sh,P}\right\} \quad (64)$$

It needs to be emphasized that the summation is over all particles that have surface area within the control volume (within boundary S_O in Fig. 9), but that the contribution from particle P in the parenthesis is only from that portion of the particle surface that lies within S_O.

For problems of current interest the gas velocities are small enough to neglect kinetic energy relative to internal energy. Similarly the work done by the viscous forces (of which viscous heating is part) can be ignored. Potential energy changes are also small enough to be neglected, and $\dot{W}^B_G$ is dropped. With these approximations, Eq. (64) can be written as

$$\frac{d}{dt}\int_{\forall_G}\rho e d\forall = -\int_{S_{OG}} h\dot{m}''dS - \dot{Q}^C_{OG} - \dot{Q}^R_G + \dot{S}_G + \underbrace{\sum_P\left\{\int_{S_P} h\dot{m}''_P dS + \dot{Q}^C_P\right\}} \quad (65)$$

where h is enthalpy, and the last term is the contribution to gas internal energy from that portion of particle P that lies within S_O.

4.3 Discretization of the Gas Energy Equation

The increase of internal energy for control volume K shown in Fig. 10 is

$$\frac{d}{dt}(M_{G,K}e_K) = -\sum_l h^l\dot{m}^l_G - \sum_l \dot{Q}^{C,l} - \dot{Q}^R_{G,K} + \dot{S}_{G,K} + \sum_P\left\{\int_{S_P} h\dot{m}''_P dS + \dot{Q}^C_P\right\} \quad (66)$$

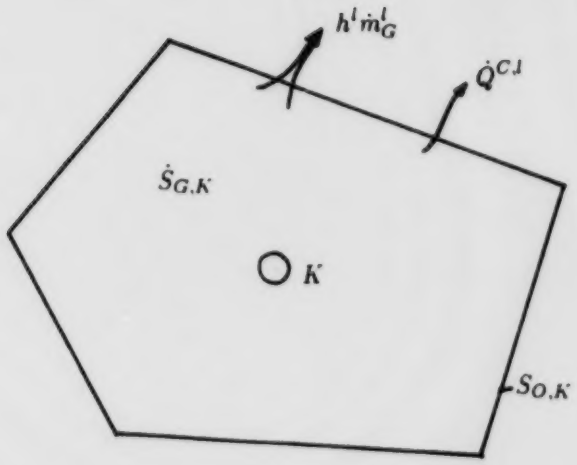

Figure 10: Notation for discrete control volume K.

where, as before, the superscript l refers to surface panel l of the control volume, and subscript K refers to the node K or to the volume surrounding node K. $\dot{Q}^{C,l}$ is the heat transfer by diffusion across panel l, positive in the direction shown.

The mass conservation equation for the gas in this control volume is given by Eq. (25). Multiplying this by the enthalpy at node K, and subtracting the resulting equation from Eq. (66)

$$\begin{aligned} M_{G,K}\frac{de_K}{dt} &= \left(\frac{p}{\rho}\right)_K \frac{dM_{G,K}}{dt} - \sum_l \dot{m}_G^l(h^l - h_K) - \sum_l \dot{Q}^{C,l} - \dot{Q}_{G,K}^R + \dot{S}_{G,K} \\ &+ \sum_P \dot{Q}_{P,K}^C + \sum_P (h_{P-surf} - h_K)\dot{m}_{P,K} \end{aligned} \tag{67}$$

where h_{P-surf} denotes the enthalpy of the gas leaving the surface of particle P, and $\dot{m}_{P,K}$ is the mass flow rate of gas leaving the portion of particle P that lies within $S_{O,K}$ (Fig. 10).

4.4 Particle Energy Equation

Following exactly the steps used to derive the integral equation for gas energy conservation, Eq. (64), except that the domain of integration is $\forall_P$ (Fig. 10) rather than $\forall_G$ (Fig. 9),

$$\begin{aligned} \frac{d}{dt}\int_{\forall_P} \rho\hat{e}d\forall &= -\int_{S_P} \rho(\hat{e} + \frac{p}{\rho})(\vec{V} - \vec{W}) \cdot \hat{n}_P dS \\ &- \dot{Q}_P^{C+R} - \dot{W}_{sh,P} + \dot{S}_P - \int_{S_P} p\vec{W} \cdot \hat{n}_P dS + \int_{\forall_P} f_j^B u_j d\forall \end{aligned} \tag{68}$$

Neglecting potential and kinetic energy (which excludes, for example, the internal energy rise when the particle collides with a surface), the work done by shear stresses at the surface (term 3 on RHS of Eq. (68), and the work done by body forces other than gravity (term 6 of Eq. (68)), the particle energy equation is

$$\frac{d}{dt}\int_{\forall_P} \rho e d\forall = -\dot{Q}_P^{C+R} - \int_{s_P} h\dot{m}_P'' dS + \dot{S}_P - \frac{p_{P-surf}}{\rho_P}\frac{dM_P}{dt} \tag{69}$$

where the particle density has been assumed uniform in the evaluation of the last (small) term.

4.5 Source of Energy From Moving Particles

The rate of heat and enthalpy transfer from one particle to the gas as it moves along the path shown in Fig. 3 is given by the first two terms on the RHS of Eq. (69). Following the steps leading to Eq. (11) for mass, and referring to Fig. 3:

$$\left(\begin{array}{l}\text{Total rate of transfer of}\\ \text{energy to gas in } \forall \text{ from one}\\ \text{particle path in } \Delta t\end{array}\right) = \int_{s_1(t)}^{s_2(t)} \frac{(\dot{m}_P h_{P-surf} + \dot{Q}_P^C)\dot{N}_P}{|\vec{V}_P|} ds \tag{70}$$

To find the total rate of internal energy transfer from the particles to the gas, the last two terms in Eqs. (65) or (67), the contributions from all paths that traverse the control volume would be summed (as in Eq. (51). For the special case of the stationary control volume in Fig. 4, Eq. (70) can be approximated as

$$\left(\begin{array}{l}\text{Total rate of transfer of}\\ \text{energy to gas in } \forall \text{ from one}\\ \text{particle path in } \Delta t\end{array}\right) \approx \left[(M_{P,1} - M_{P,2})\bar{h}_{P-surf} + \bar{\dot{Q}}_P^C(t_2 - t_1)\right]\dot{N}_P \tag{71}$$

where the overbar denotes the time average during the particle flight from point 1 to 2.

For the case shown in Fig. 4B

$$\left(\begin{array}{l}\text{Total rate of transfer of}\\ \text{energy to gas in } \forall \text{ from one}\\ \text{particle path in } \Delta t\end{array}\right) \approx \left[\frac{(M_{P,1} - M_{P,2})\bar{h}_{P-surf}}{t_B - t_A} + \bar{\dot{Q}}_P^C\right]\dot{N}_P(t_2 - t_1) \tag{72}$$

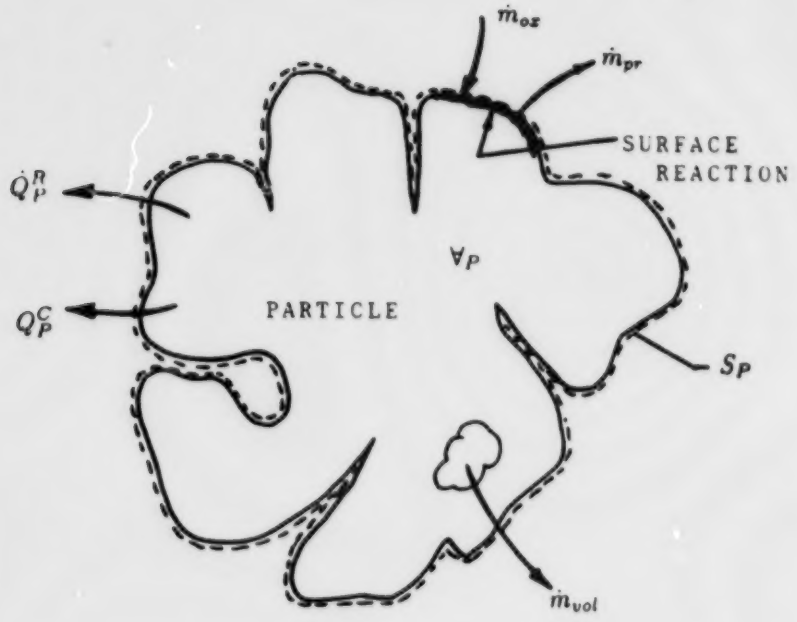

Figure 11: Nomenclature for particle energy balance with combustion and devolatilization.

4.6 Details of the Particle Energy Balance Including Chemical Reaction

Equation (68), or after some approximations Eq. (69), is the energy balance for a particle. Since e depends mainly on the particle temperature, its temperature distribution is required to evaluate the LHS. For a typical coal particle of 30 $[\mu m]$ diameter, the convective heat transfer coefficient is roughly $h^C \approx 4000[W/m^2K]$ and the radiative coefficient is roughly $h^R = 24000[W/m^2K]$. The Biot number, which is a measure of the internal to surface heat transfer resistances, is therefore

$$Bi = \frac{(h^C + h^R)D_P}{k_P} \sim 0.004.$$

For such a small internal resistance, the temperature will be nearly uniform inside the particle, so that

$$\frac{d}{dt}\int_{\forall_P} \rho e d\forall \approx \frac{d}{dt}(M_P e_P) \tag{73}$$

If the enthalpies and internal energies in Eq. (69) include the molecular bonding energy, the heat of reaction and volitilization is included so $\dot{S}_P$ will be zero. Combining the first and last terms in Eq. (69) to convert internal energy to enthalpy, and

separating the mass flow rates of the oxidant and products for the heterogeneous reaction and of the volatiles for the devolitilization (see Fig. 11), Eq. (69) becomes

$$\frac{d}{dt}(M_P h_P) - M_P \frac{d}{dt}\left(\frac{p_{P-surf}}{\rho_P}\right) = -\dot{Q}_P^{C+R} + \dot{m}_{ox} h_{ox}(T_P) - \dot{m}_{pr} h_{pr}(T_P) - \dot{m}_{vol} h_{vol}(T_P) \quad (74)$$

where ox, pr, vol refer respectively to the oxidant, products and volatiles, and where the mass flow rates are positive in the directions shown on Fig. 11.

From a mass balance for the heterogeneous reaction

$$\dot{m}_{fu} + \dot{m}_{ox} = \dot{m}_{pr} \quad (75)$$

where $\dot{m}_{fu}$ is the rate of disappearance of the fuel for the reaction which in turn accounts for some of the disappearance of the particle mass

$$\dot{m}_{fu} = -\frac{dM_{P,fu}}{dt} \quad (76)$$

The rate of disappearance of a particle that becomes volatiles accounts for the remainder of the particle mass loss

$$\dot{m}_{vol} = \frac{-dM_{P,vol}}{dt} \quad (77)$$

The particle enthalpy is defined as the sum of the enthalpies that become fuel, volatiles, and ash respectively

$$M_P h_P = M_{P,vol} h_{P,vol} + M_{P,fu} h_{P,fu} + M_{P,ash} h_{P,ash} \quad (78)$$

Substituting Eqs. (75) to (78) into (74), and assuming that the pressure is uniform in the particle and equal to its surface value (so that the second term in Eq. (74) combines with the first term to convert e_P to h_P), Eq. (74) becomes

$$M_{P,vol}\frac{de_{P,vol}}{dt} + M_{P,fu}\frac{de_{P,fu}}{dt} + M_{P,ash}\frac{de_{P,ash}}{dt} = -\dot{Q}^{C+R}$$
$$+[\dot{m}_{ox} h_{ox}(T_P) + \dot{m}_{fu} h_{P,fu}(T_P) - \dot{m}_{pr} h_{pr}(T_P)] + \dot{m}_{vol}[h_{P,vol}(T_P) - h_{vol}(T_P)] \quad (79)$$

The term in the first square bracket in Eq. (79) can be written in terms of the heat of reaction $L_H(T_o)$, where T_o is a reference temperature at which the reaction is tabulated. With the aid of the energy balance shown in Fig. 12 this term becomes

$$[\dot{m}_{ox} h_{ox}(T_P) + \dot{m}_{fu} h_{P,fu}(T_P) - \dot{m}_{pr} h_{pr}(T_P)] =$$
$$\dot{m}_{fu} L_H(T_o) + \dot{m}_{ox}\Delta h_{ox} + \dot{m}_{fu}\Delta h_{P,fu} - \dot{m}_{pr}\Delta h_{pr} \quad (80)$$

where $\Delta h_y = h_y(T_P) - h_y(T_o)$ is the enthalpy difference for material y between the reference temperature T_o and the particle temperature T_P.

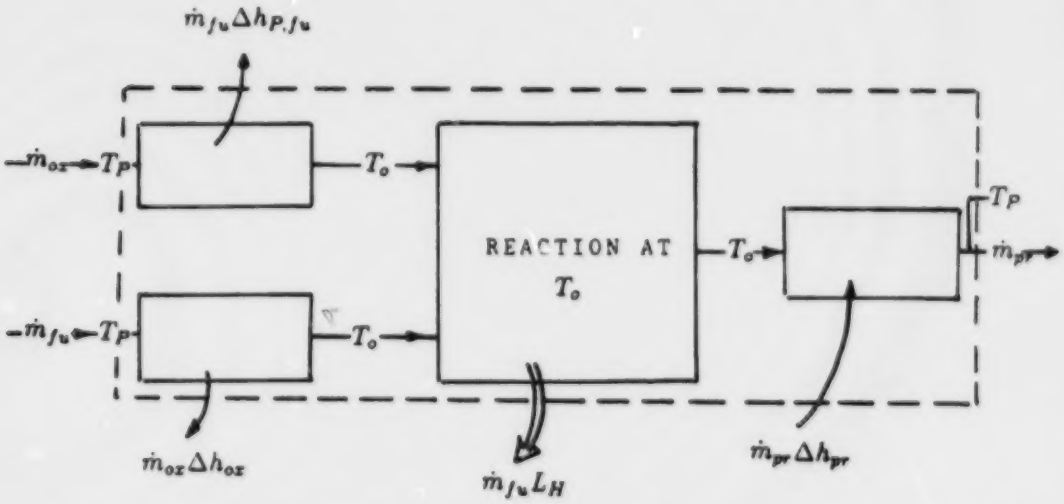

Figure 12: Energy balance to relate energy release by reaction at temperatures T_P to the heat of reaction at T_o.

The energy balance related to devolitilization, shown in Fig. 13, yields

$$\dot{m}_{vol}[h_{vol}(T_P) - h_{P,vol}(T_P)] = \dot{m}_{vol}L_V(T_o) + \dot{m}_{vol}[\Delta h_{vol} - \Delta h_{P,vol}] \tag{81}$$

where Δh is defined as in Eq. (80). Substituting Eq. (80) and Eq. (81) into Eq. (79)

$$M_{P,fu}\frac{de_{P,fu}}{dt} + M_{P,vol}\frac{de_{P,vol}}{dt} + M_{P,ash}\frac{de_{P,ash}}{dt} = -\dot{Q}_P^{C+R} + \dot{m}_{fu}L_H(T_o) - \dot{m}_{vol}L_V(T_o) + [\dot{m}_{ox}\Delta h_{ox} + \dot{m}_{fu}\Delta h_{P,fu} - \dot{m}_{pr}\Delta h_{pr}] + [\dot{m}_{vol}(\Delta h_{P,vol} - \Delta h_{vol})] \tag{82}$$

For hydrocarbon fuels, the terms in square brackets are often small and therefore neglected. If the internal energy is written in terms of the specific heats of the portions of the particle that become fuel and volatiles respectively

$$\begin{aligned} M_{P,fu}\frac{de_{P,fu}}{dt} &+ M_{P,vol}\frac{de_{P,vol}}{dt} + M_{P,ash}\frac{de_{P,ash}}{dt} \\ &= (M_{P,fu}C_{P,fu} + M_{P,vol}C_{P,vol} + M_{P,ash}C_{P,ash})\frac{dT_P}{dt} \\ &= M_P\bar{C}_P\frac{dT_P}{dt} \end{aligned} \tag{83}$$

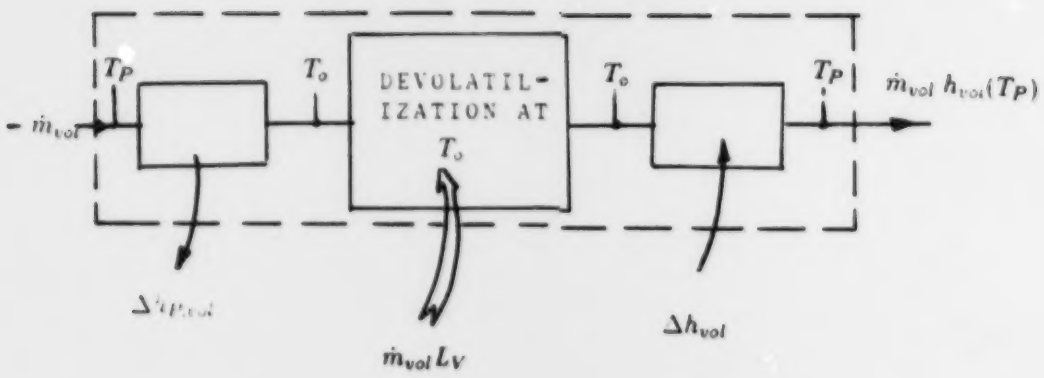

Figure 13: Energy balance to relate energy required for devolatilization at temperature T_P to that at T_o.

With these approximations, Eq. (82) becomes

$$M_P \bar{C}_P \frac{dT_P}{dt} \approx -\dot{Q}_P^{C+R} + \dot{m}_{fu} L_H(T_o) - \dot{m}_{vol} L_V(T_o) \tag{84}$$

5 CONSERVATION OF A CONVECTED AND DIFFUSED SCALAR

5.1 Integral Conservation Equation

Let ϕ^n be the mass of constituent n per unit mass of mixture (e.g., $kg - CO_2/kg - mixture$). Such a scalar can be transported by the bulk motion of the fluid and by diffusion, can be generated (e.g. by chemical reaction), and can accumulate. For a differential control volume, conservation of ϕ^n is expressed by

$$\frac{\partial}{\partial t}(\rho\phi^n) + \frac{\partial}{\partial x_j}(\rho u_j \phi^n) = -\frac{\partial q_j^n}{\partial x_j} + (\dot{S}^n)''' \tag{85}$$

where ρ and u_j are density and velocity of the mixture that contains constituent ϕ^n and q_j^n is the flux of ϕ^n by diffusion.

According to Leibnitz rule, the rate of increase of the n-constituent in the volume $\forall_G$ in Fig. 14 is

$$\frac{d}{dt}\left(\int_{\forall_G} \rho\phi^n d\forall\right) = \int_{\forall_G} \frac{\partial}{\partial t}(\rho\phi^n) d\forall + \int_{S_{OG}+S_I} \rho\phi^n \vec{W}\cdot\hat{n} dS \tag{86}$$

Combining Eqs. (85) and (86):

$$\frac{d}{dt}\int_{\forall_G} \rho\phi^n d\forall = -\int_{S_{OG}+S_I} \rho\phi^n(\vec{V}-\vec{W})\cdot\hat{n} ds - \int_{S_{OG}+S_I} \vec{q}^{\,n}\cdot\hat{n} dS + \int_{\forall_G} (\dot{S}^n)''' d\forall \tag{87}$$

The advective transport of ϕ^n across the S_{OG} boundary is written as

$$\int_{S_{OG}} \phi^n \dot{m}'' dS = \int_{S_{OG}} \rho\phi^n(\vec{V}-\vec{W})\cdot\hat{n} dS \tag{88}$$

and the transport of ϕ^n across S_{OG} by diffusion is defined by

$$\dot{D}_{OG}^n = \int_{S_{OG}} \vec{q}^{\,n}\cdot\hat{n} dS \tag{89}$$

Similarly, the advective transport of ϕ^n across a particle boundary S_P, positive in the direction of $\hat{n}_P$, that lies partly or entirely inside S_O is defined as

$$\dot{m}_P\phi_{P-surf}^n = \int_{S_P} \dot{m}_P''\phi^n dS = \int_{S_P} \rho\phi^n(\vec{V}-\vec{W})\cdot\hat{n}_P dS \tag{90}$$

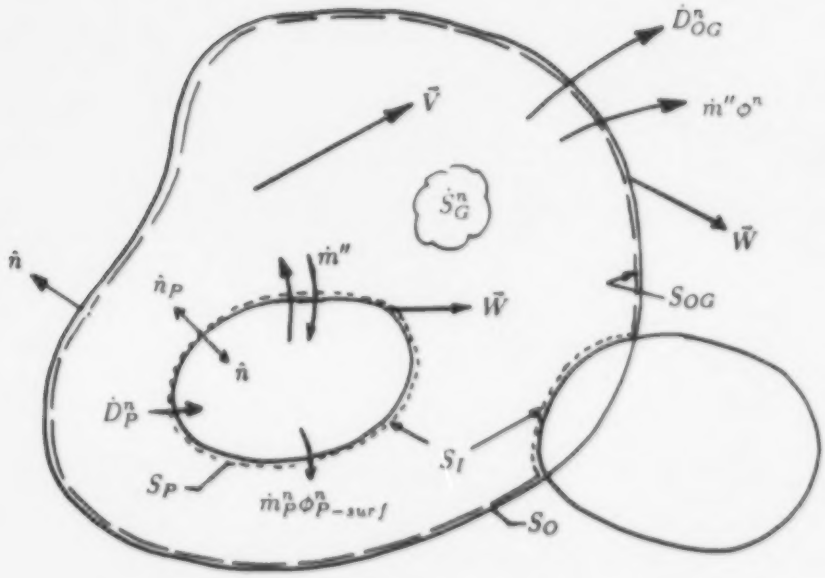

Figure 14: Definition sketch for scalar conservation.

nd the diffusive transport of ϕ^n across S_P, that is convected away in the particle boundary layer, is

$$\dot{D}^n_P = \int_{S_P} \vec{q}^{\,n} \cdot \hat{n} dS \tag{91}$$

Just as $\dot{Q}^C_P$ is the convective heat transfer obtained from the product of the heat transfer coefficient and the temperature difference, so too is D^n_P is obtained from the product of the convective mass transfer coefficient (calculated from the Sherwood number) and the difference in concentration of the species between the surface and the surrounding fluid.

The source of ϕ^n within the gas, normally as a result of gas-phase reaction, is

$$\dot{S}^n_G = \int_{\forall_G} (\dot{S}^n)''' d\forall \tag{92}$$

Substituting Eqs. (88) to (92) into Eq. (87) results in

$$\frac{d}{dt}\int_{\forall_G} \rho\phi^n d\forall = -\int_{S_{OG}} \dot{m}''\phi^n dS - \dot{D}^n_{OG} + \dot{S}^n_G + \sum_P \underbrace{(\dot{m}''_P\phi^n_{P-surf} - \dot{D}^n_P)}_{\dot{S}^n_P} \tag{93}$$

This equation is identical in form to Eq. (65) for internal energy.

5.2 Discretization of the Concentration Equation

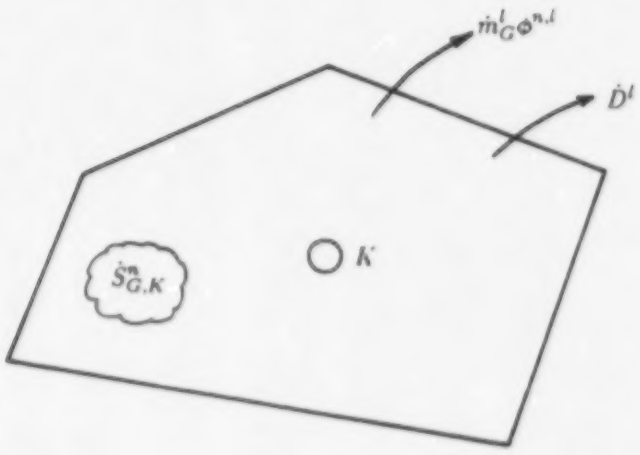

Figure 15: Notation for discrete control volume K.

The first level discrete approximation of Eq. (93) using the notation in Fig. 15, is

$$\frac{d}{dt}(M_{G,K}\phi^n_K) = -\sum_l \dot{m}_G^l \phi^{n,l} - \sum_l \dot{D}^l + \dot{S}^n_{G,K} + \sum_P \dot{S}^n_P \tag{94}$$

where superscript l refers to the surface panel l of the control volume, and subscript K refers to the node or to the finite volume surrounding the node.

Multiplying the mass conservation equation for the gas, Eq. (25), by ϕ^n_K

$$\phi^n_K \frac{d}{dt} M_{G,K} + \sum_l \dot{m}_G^l \phi^n_K = \sum_P \dot{m}_P \phi^n_K \tag{95}$$

Subtracting this from Eq. (94)

$$M_{G,K}\frac{d\phi^n_K}{dt} = -\sum_l \dot{m}_G^l(\phi^{n,l} - \phi^n_K) - \sum_l \dot{D}^l + \dot{S}^n_{G,K} + \sum_P (\dot{m}^n_P(\phi^n_{P-surf} - \phi^n_K) - \dot{D}^n_P) \tag{96}$$

This is the form of the conservation equation for ϕ^n that is suitable for the final stage of discretization, in which the surface fluxes are approximated in terms of the nodal values.

5.3 Source of Constituent n From Moving Particles

As in previous examples, the rate of transfer of constituent n in time Δt from the $\dot{N}_P$ particles per second that move along a particular path that crosses through the stationary volume $\forall$ in Fig. 4 is approximately

$$\left(\begin{array}{l} \text{Total rate of transfer of constituent} \\ n \text{ to the gas from one particle path in } \Delta t \end{array} \right) \approx \bar{\dot{S}}_P^n \dot{N}_P (t_2 - t_1) \tag{97}$$

where the overbar denotes the average $\bar{\dot{S}}_P^n$ over the path from s_1 to s_2 and within the time period Δt. $\dot{S}_P^n$ is defined in Eq. (93).

6 DEVELOPMENT OF GIBB'S DIFFUSION MODEL FOR RADIATION

6.1 Introduction

The radiation model used in MODTUN and FAFNIR is referenced to Gibb, but only the final results of the model seem to be publicly available. Radiation heat transfer is important for the problems of present interest, so it is mandatory to understand the approximations that are inherent in the model. There seems to be no choice but to derive the model from first principles, guided by the few intermediate steps provided by Rizvi (1985). This chapter reports this derivation. The first part of the derivation is rigorous, but the simplification of the rigorous equations to obtain the Gibb model involves approximations that the writer has been unable to fully justify. Physical arguments and/or experimental justification were probably used by Gibb.

To overcome some of the approximations inherent in the Gibb model a new 'Finite Volume' radiation model was developed. Much of the development required for this Finite Volume Method is common with that for the Gibb model and is therefore presented in this Chapter. Specific discussion of the Finite Volume Method is, however, deferred to Chapter 7.

6.2 Radiation Transport Equation

For the narrow beam of radiation in solid angle $d\Omega$ in the direction (see Fig. 16) of the unit vector $\hat{s}$, the increase in spectral intensity with distance is

$$\frac{di_\lambda}{ds} = K_{\lambda a,g}(i_{b\lambda} - i_\lambda) + (E_{\lambda,P} - A_{\lambda,P}) + (S^i_\lambda - S^o_\lambda) \tag{98}$$

where
- $K_{\lambda a,g}$ spectral absorption/emission coefficient of the gas,
- $i_{b\lambda}$ $= \sigma T^4/\pi$ is the black body spectral intensity at λ,
- i_λ = spectral intensity at s in direction $\vec{s}$,
- $E_{\lambda P}ds$ = increase in i_λ due to particle emission in ds,
- $A_{\lambda,P}ds$ = decrease in i_λ due to particle absorption in ds,
- $S^i_\lambda ds$ = increase in i_λ due to inscattering in ds, and
- $S^0_\lambda ds$ = decrease in i_λ due to outscattering in ds.

This is the Radiation Transport Equation (RTE).

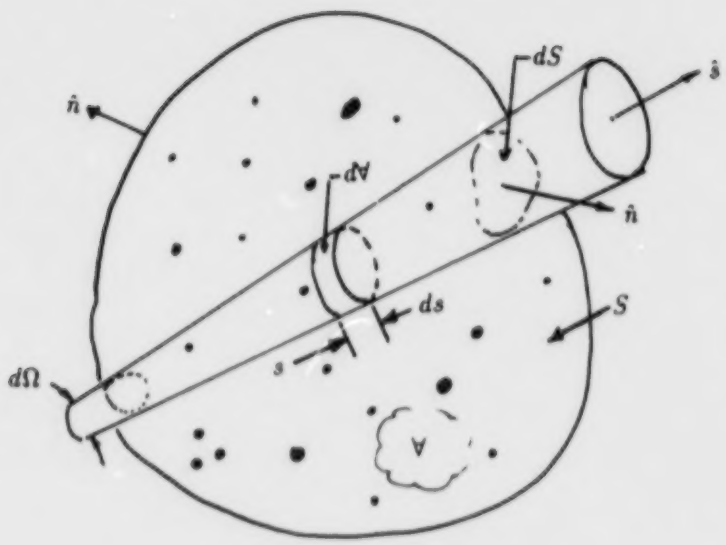

Figure 16: Nomenclature for radiation heat transfer derivation.

The radiation strongly affects the direct heating or cooling of the particles and gas, and the heat flux on the walls enclosing the flow. To calculate these effects, the domain is divided into discrete volumes, such as $\forall$ shown in Fig. 16, and the RTE must be converted to an equation for this volume that permits the quantities of interest to be estimated.

Radiation properties such as absorption coefficient, surface emissivity, etc. are (unfortunately for analysis) strongly dependent on wavelength. This is why the RTE is written for one value of λ. Since the interest is in total radiant flux, each term of the RTE must be integrated over all wavelengths.

The radiative energy flux also depends, often very strongly, on direction. The equations are written in terms of radiation intensity within a solid angle $d\Omega$ that is in a particular direction $\hat{s}$. To find the net radiative energy transfer, a summation or integration over all solid angles is required.

The integrations over wavelength and solid angle result in an equation for radiation transfer for a differential volume. To obtain an equation for the discrete volume, an additional integration over a finite volume $\forall$ is required.

The following sections provide the details of these integrations for each term of the RTE, and the approximations that lead to Gibb's model. Assumptions will be introduced where needed to maintain reasonable simplicity.

6.3 Integration of the di_λ/ds Term

The 'total' intensity is related to the spectral intensity in Eq. (98) by

$$i = \int_0^\infty i_\lambda d\lambda \tag{99}$$

Integration of the di_λ/ds term in the RTE gives

$$\int_0^\infty \frac{di_\lambda}{ds} d\lambda = \frac{di}{ds} \tag{100}$$

Integrating this over the volume in Fig. 16

$$\int_\forall \int_0^\infty \frac{di_\lambda}{ds} d\lambda d\forall = \int_\forall \vec{\nabla} i \cdot \hat{s} d\forall = \int_\forall \vec{\nabla} \cdot (i\hat{s}) d\forall = \int_S i\hat{s} \cdot \hat{n} dS \tag{101}$$

In this equation $\hat{s}$ is a unit vector in the direction of the displacement. Equation (101) gives the net rate at which radiative energy leaves (i.e., positive in the direction of $\hat{n}$) through the surface of $\forall$ per unit solid angle for the given direction $\hat{s}$.

Integrating Eq. (101) over all solid angles

$$\int_{4\pi} \int_\forall \int_0^\infty \frac{di_\lambda}{ds} d\lambda d\forall d\Omega = \int_S \left(\int_{4\pi} i\hat{s} d\Omega \right) \cdot \hat{n} dS = \int_S \vec{q}^R \cdot \hat{n} dS \tag{102}$$

This is the net rate at which radiant energy, including contributions from all directions, leaves through the surface of $\forall$. The radiation heat flux vector $\vec{q}^R$, used in the energy balance (e.g., Eq. (57)), is defined as

$$\vec{q}^R = \int_{4\pi} i\hat{s} d\Omega \tag{103}$$

To be strictly correct, the volume integration in Eq. (101) should be only over the gas portion of the control volume, and the surface S should include the outside control volume surface AND and surfaces of all particles within $\forall$. The integral over the particle surfaces leads to the emission, absorption and scattering of the particles. Rather than keep track of all these details, the volume of the particles within $\forall$ is ignored and their effect is included in the particle emission, absorption and scattering source terms of the RHS of Eq. (98).

6.4 Integration of the Gas Emission Term

Integration of the gas emission term, term 1 on the RHS of Eq. (98), over wavelength results in

$$\int_0^\infty K_{\lambda a,g} i_{b\lambda} d\lambda \approx K_{a,g} \int_0^\infty i_{b\lambda} d\lambda = K_{a,g} i_b(T_G) \tag{104}$$

where

$$i_b(T_G) = \sigma T_G^4/\pi \tag{105}$$

To carry out this integration, the gas has been assumed to be gray ($K_{a,g} = K_{\lambda,a,g}$), which is a poor approximation but one that is required for simplicity. i_b is the black body emissive power at the gas temperature T_G.

Integrating over the volume $\forall$

$$\int_\forall \int_0^\infty K_{\lambda a,g} i_{b\lambda} d\lambda d\forall = \bar{K}_{a,g}^{\forall} \bar{i}_b^{\forall} \forall \tag{106}$$

where the overbar denotes the average over the volume. This is the total rate at which radiative energy is emitted from the gas in $\forall$ per unit solid angle. Integration over all directions yields the total gas emission rate. Since $K_{a,g}$ and i_b are directionally independent,

$$\int_{4\pi} \int_0^\infty \int_\forall K_{\lambda a,g} i_{b\lambda} d\lambda d\forall d\Omega = \bar{K}_{a,g}^{\forall} \bar{i}_b^{\forall}(T_G) 4\pi \forall \tag{107}$$

6.5 Integration of the Gas Absorption Term

Following the same steps as for the gas emission term

$$\int_0^\infty K_{\lambda a,g} i_\lambda d\lambda \approx K_{a,g} i \tag{108}$$

which assumes again that the gas is gray. Integrating over the volume

$$\int_\forall \int_0^\infty K_{\lambda a,g} i_\lambda d\lambda d\forall = \bar{K}_{a,g}^{\forall} \int_{4\pi} i d\forall = \bar{K}_{a,g}^{\forall} \bar{i}^{\forall} \forall \tag{109}$$

Integrating over all directions

$$\int_{4\pi}\int_{V}\int_{0}^{\infty} K_{\lambda a,g} i_\lambda d\lambda dV d\Omega = \bar{K}^{V}_{a,g} < \bar{i}^{V} > 4\pi V \tag{110}$$

where the directional average is defined by

$$< \bar{i}^{V} > = \frac{1}{4\pi}\int_{4\pi} \bar{i}^{V} d\Omega \tag{111}$$

6.6 Particle Emission

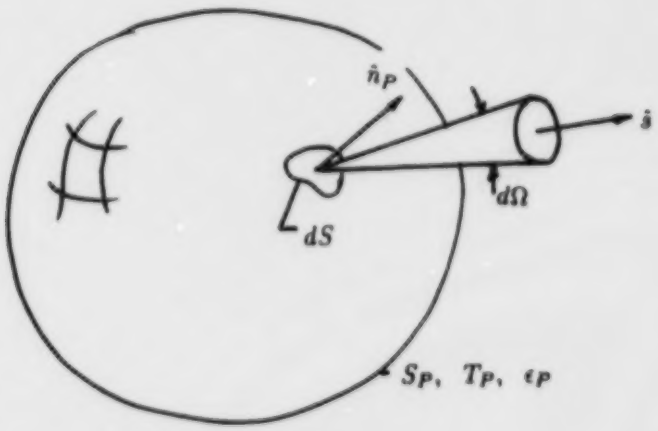

Figure 17: Nomenclature for particle emission

The emission in the wavelength window $d\lambda$ from one particle (Fig. 17) with surface area S_P and uniform temperature T_P is

$$\left(\begin{array}{l}\text{rate of emission of energy}\\ \text{from one particle over } d\lambda\end{array}\right) = \int_{S_P}\int_{2\pi} \epsilon_{\lambda,P} i_{b,\lambda}(T_P)\hat{n}_P \cdot \hat{s} d\Omega dS d\lambda \tag{112}$$

Assuming that the surface emissivity is directionally independent and that the particle is spherical

$$\left(\begin{array}{l}\text{rate of emission of energy}\\ \text{from particle of radius } r_P \&\\ \text{temperature } T_P \text{ within } d\lambda\end{array}\right) = \epsilon_{\lambda,P} i_{b\lambda}(T_P)\pi 4\pi r_P^2 d\lambda \tag{113}$$

This radiation will be isotropic, so the radiation emitted in any particular $d\Omega$ will be $d\Omega/4\pi$ of the amount in Eq. (113)

$$\left(\begin{array}{l}\text{rate of emission of energy}\\ \text{from particle of radius } r_P \text{ and}\\ \text{temperature } T_P \text{ within } d\Omega \text{ and } d\lambda\end{array}\right) = \epsilon_{\lambda,P} i_{b,\lambda}(T_P)\pi r_P^2 d\lambda d\Omega \tag{114}$$

There will be a distribution of particle sizes and temperatures within the volume $\forall$ in Fig. 16. Using the notation of Rizvi, let $n(r_P, T_P)dr_P dT_P$ be the number of particles per unit volume that have radii within the window dr_P and temperatures within dT_P. The total emission from all the particles within $\forall$ is therefore

$$\left(\begin{array}{l}\text{rate of emission}\\ \text{of energy from}\\ \text{all particles in}\\ \forall \text{ into } d\Omega\end{array}\right) = \int_{\forall}\int_0^\infty \left\{\int_0^\infty \int_0^\infty \epsilon_{\lambda,P} i_{b,\lambda}(T_P)\pi r_P^2 n(r_P, T_P)dr_P dT_P\right\} d\lambda d\forall d\Omega \tag{115}$$

For gray particles (which is a reasonable approximation) $\epsilon_{\lambda,P} = \epsilon_P$,

$$\left(\begin{array}{l}\text{rate of emission}\\ \text{of energy from}\\ \text{all particles in}\\ \forall \text{ into } d\Omega\end{array}\right) = \int_{\forall}\left\{\int_0^\infty \int_0^\infty \epsilon_P i_b(T_P)\pi r_P^2 n(r_P, T_P)dr_P dT_P\right\} d\forall d\Omega \tag{116}$$

where $i_b(T_P) = \sigma T_P^4/\pi$.

The following quantities are defined

$$K'_P = \int_0^\infty \int_0^\infty \pi r_P^2 n(r_P, T_P)dr_P dT_P = \left(\begin{array}{l}\text{cross section of particles}\\ \text{per unit volume}\end{array}\right) \tag{117}$$

$$\bar{\epsilon}_P^P = \frac{1}{K'_P}\int_0^\infty \int_0^\infty \epsilon_P \pi r_P^2 n(r_P, T_P)dr_P dT_P = \left(\begin{array}{l}\text{average emissivity of}\\ \text{particles per unit volume}\end{array}\right) \tag{118}$$

$$\bar{\rho}_P^P = \frac{1}{K'_P}\int_0^\infty \int_0^\infty \rho_P \pi r_P^2 n(r_P, T_P)dr_P dT_P = (\text{average reflectivity}) \tag{119}$$

$$\bar{i}_{b,P}^P = \frac{1}{\bar{\epsilon}_P^P K'_P}\int_0^\infty \int_0^\infty \epsilon_P i_b(T_P)\pi r_P^2 n(r_P, T_P)dr_P dT_P \tag{120}$$

where the overbar(e.g. $\bar{\epsilon}^P$) denotes an average over all particles. Using Eq. (117) in Eq. (116)

$$\left(\begin{array}{l} \text{rate of emission of energy} \\ \text{from particles within } \forall \text{ into } d\Omega \end{array} \right) = \int_{\forall} \bar{\epsilon}_P^P K_P' \bar{i}_{b,P}^P d\forall d\Omega \tag{121}$$

Integrating this over all directions

$$\begin{aligned} \left(\begin{array}{l} \text{rate of emission of energy} \\ \text{from particles in } \forall \end{array} \right) &= 4\pi \int_{\forall} \bar{\epsilon}_P^P K_P' \bar{i}_{b,P}^P d\forall \\ &= \int_{4\pi} \int_0^{\infty} \int_{\forall} E_{\lambda,P} d\forall d\lambda d\Omega = 4\pi \, \bar{\bar{\epsilon}}_P^{\forall} \, \bar{K}_P'^{\forall} \, \bar{\bar{i}}_{b,P}^{\forall} \forall \end{aligned} \tag{122}$$

6.7 Particle Absorption

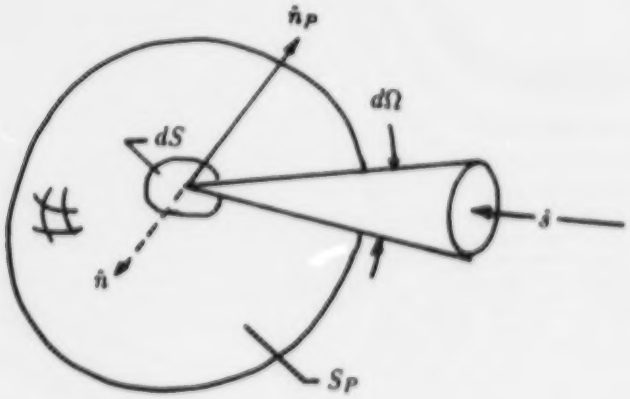

Figure 18: Nomenclature for particle absorption.

The energy absorbed on the surface area S_P of one particle from radiation in direction $\hat{s}$ within solid angle $d\Omega$ (see Fig. 18) and within the wavelength window $d\lambda$ is

$$\int_{\left(\begin{array}{l} \text{all } S_P \text{ for} \\ \hat{s} \cdot \hat{n} > 0 \end{array} \right)} \epsilon_{\lambda,P} i_\lambda (\hat{s} \cdot \hat{n}) dS d\Omega d\lambda = \epsilon_{\lambda,P} i_\lambda \pi r_P^2 d\Omega d\lambda \tag{123}$$

If the particles are gray, the radiation absorbed by all particles is

$$\left(\begin{array}{l}\text{rate of energy}\\ \text{absorption by all}\\ \text{particles in } \forall \text{ of}\\ \text{radiation within}\\ d\Omega \text{ and } d\lambda\end{array}\right) = \int_{\forall}\left\{\int_0^\infty\int_0^\infty \epsilon_{\lambda,p} i_\lambda(\hat{s})\pi r_p^2 n(r_p,T_p)dr_p dT_p\right\}d\forall d\Omega d\lambda \quad (124)$$

$$= \int_{\forall} i_\lambda(\hat{s})K'_p \bar{e}_p^p d\forall d\Omega d\lambda \quad (125)$$

where the definition in Eq. (118) has been used. Integrating this over all λ and over all angles

$$\left(\begin{array}{l}\text{Total rate of absorption}\\ \text{of energy by}\\ \text{all particles within } \forall\end{array}\right) = 4\pi < \bar{i}^{\forall} > K'^{\forall}_p \bar{\epsilon}^{\forall}_p \forall \quad (126)$$

6.8 Gas Scattering

The gas outscattering term in Eq. (98) is

$$S^0_{\lambda,g} = K_{\lambda s,g} i_\lambda(\hat{s}) \quad (127)$$

and the gas inscattering term is

$$S^i_{\lambda,g} = \frac{K_{\lambda s,g}}{4\pi}\int_{4\pi}\Phi(\hat{s}',\hat{s})i_\lambda(\hat{s}')d\Omega' \quad (128)$$

where $d\Omega'$ is the solid angle centered on the unit vector $\hat{s}'$, and Φ is the phase function that describes the amount of scattering that occurs from $d\Omega'$ into unit solid angle in the $\hat{s}$ direction. The total reduction in radiant energy due to outscattering in the volume $d\forall$ and in the wavelength window $d\lambda$ is

$$d\lambda d\forall \int_{4\pi} S^0_{\lambda,g} d\Omega = K_{\lambda s,g}\int_{4\pi} i_\lambda(\hat{s})d\Omega d\lambda d\forall = K_{\lambda s,g} 4\pi < i_\lambda > d\lambda d\forall \quad (129)$$

The total increase in energy in the same $d\forall$ and $d\lambda$ due to inscattering is

$$\begin{aligned} d\lambda d\forall \int_{4\pi} S^i_{\lambda,g} d\Omega &= K_{\lambda s,g} d\lambda d\forall \int_{4\pi}\frac{1}{4\pi}\left\{\int_{4\pi} i_\lambda(\hat{s}')\Phi(\hat{s}',\hat{s})d\Omega'\right\}d\Omega \\ &= K_{\lambda s,g} d\lambda d\forall \int_{4\pi} i_\lambda(\hat{s}')\left\{\frac{1}{4\pi}\int_{4\pi}\Phi(\hat{s}',\hat{s})d\Omega\right\}d\Omega' \\ &= K_{\lambda s,g} 4\pi < i_\lambda > d\lambda d\forall \end{aligned} \quad (130)$$

The total outscattered energy for any $d\lambda$ and $d\forall$ is therefore exactly balanced by the total inscattered energy for the same $d\lambda$ and $d\forall$. Scattering can affect the amount of radiant energy travelling in a given direction, but not the total amount (over all angles) of radiant energy.

6.9 Particle Outscattering

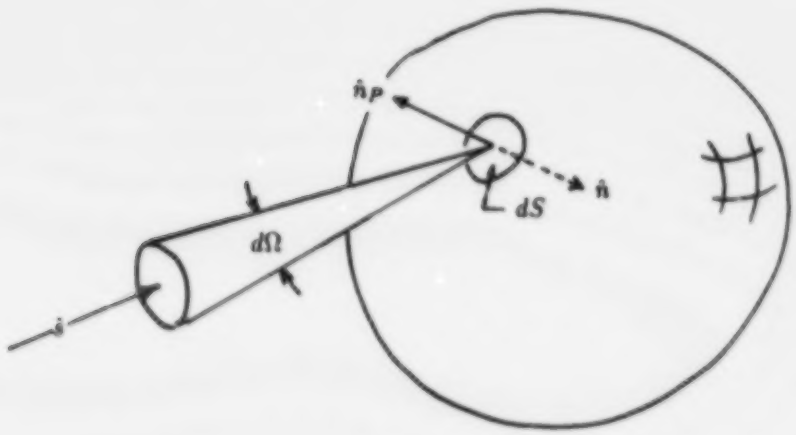

Figure 19: Nomenclature for particle outscattering.

The reflectivity of the particle in Fig. 19 is assumed to diffuse. The reflected energy is

$$\left(\begin{array}{l}\text{Rate of which}\\ \text{radiant energy}\\ \text{in } d\Omega \text{ and } d\lambda \text{ is}\\ \text{scattered from}\\ \text{one particle}\end{array}\right) = \int_{S_P \text{ for } \hat{s}\cdot\hat{n}>0} \rho_\lambda i_\lambda(\hat{s})\hat{s}\cdot\hat{n}\,dS\,d\Omega\,d\lambda$$

$$= \rho_{\lambda,P} i_\lambda(\hat{s})\pi r_P^2 d\Omega\,d\lambda \qquad (131)$$

Summing this over all particles, and assuming that the particles are gray

$$\left(\begin{array}{l}\text{Total rate at which}\\ \text{energy in } d\lambda \text{ and } d\Omega\\ \text{is scattered by}\\ \text{the particles in } d\forall\end{array}\right) = \int_0^\infty \int_0^\infty \rho_{\lambda,P} i_\lambda(\hat{s})\pi r_P^2 n(r_P, T_P)\,dr_P\,dT_P\,d\Omega\,d\lambda\,d\forall$$

$$= \bar{\rho}_p^p K'_p i_\lambda(\hat{s}) d\Omega d\lambda dV \tag{132}$$

Integrating over all directions

$$\left(\begin{array}{l} \text{Total rate at which energy} \\ \text{in} d\lambda \text{ is outscattered by} \\ \text{particles in } dV \text{ in all directions} \end{array} \right) = \bar{\rho}_p^p K'_p < i_\lambda > 4\pi d\lambda dV \tag{133}$$

6.10 Particle Inscattering

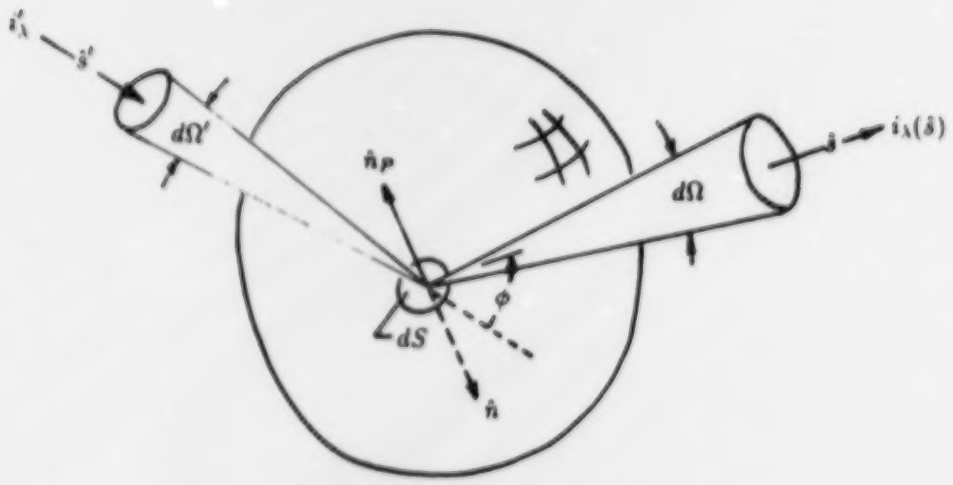

Figure 20: Nomenclature for particle inscattering.

The radiant energy in the window $d\lambda$ from $d\Omega'$ that falls on dS is

$$i'_\lambda d\Omega' dS(\hat{s}' \cdot \hat{n}) d\lambda$$

The reflected energy from dS is $\rho_{\lambda,p}$ times this quantity. Integrating this over the particle surface

$$\left(\begin{array}{l} \text{radiant energy from } d\Omega' \\ \text{in } d\lambda \text{ reflected by particle} \end{array} \right) = \rho_{\lambda,p} i'_\lambda d\Omega' \pi r_p^2 d\lambda \tag{134}$$

The portion of this energy that falls within $d\Omega$ is given in terms of the phase function for the particle $\Phi_p(\hat{s}', \hat{s})$ as follows

$$\left(\begin{array}{l}\text{radiant energy from } d\Omega' \\ \text{in } d\lambda \text{ that is reflected into } d\Omega\end{array}\right) = \rho_{\lambda,p} i'_\lambda d\Omega' \pi r_p^2 d\lambda \frac{d\Omega}{4\pi} \Phi_p(\hat{s}', \hat{s}) \tag{135}$$

The total incident energy on the spherical particle that ends up in the solid angle $d\Omega$ is therefore

$$\left(\begin{array}{l}\text{total incident radiant energy} \\ \text{in } d\lambda \text{ scattered into } d\Omega\end{array}\right) = \rho_{\lambda,p} \left\{\frac{1}{4\pi}\int_{4\pi} i'_\lambda \Phi_p(\hat{s}', \hat{s}) d\Omega'\right\} \pi r_p^2 d\Omega d\lambda \tag{136}$$

For diffuse particles, the phase function is (see Siegel and Howell, 1981)

$$\Phi_p = \frac{8}{3\pi}(\sin\phi - \phi\cos\phi) \tag{137}$$

where ϕ is the angle in Fig. 20 between the forward direction along $\hat{s}'$ and $\hat{s}$.

For all the particles in $d\,\forall$ the energy scattered into $d\Omega$ is

$$\begin{aligned}\left(\begin{array}{l}\text{Total scattered energy} \\ \text{in } d\lambda \text{ from all} \\ \text{directions and from} \\ \text{all particles in} \\ d\forall \text{ into direction } d\Omega\end{array}\right) &= \int_0^\infty \int_0^\infty \rho_\lambda \left\{\frac{1}{4\pi}\int_{4\pi} i'_\lambda \Phi_p d\Omega'\right\} \times \\ &\qquad \pi r_p^2 n(r_p, T_p) dr_p dT_p d\forall d\Omega d\lambda \\ &= \bar{\rho}_\lambda^P K'_P \left\{\frac{1}{4\pi}\int_{4\pi} i'_\lambda \Phi_p d\Omega'\right\} d\forall d\Omega d\lambda \end{aligned} \tag{138}$$

where Eq. (119) has been used.

The total inscattered energy in all directions is obtained by integrating Ω over the solid angle 4π

$$\begin{aligned}\left(\begin{array}{l}\text{Total inscattered energy} \\ \text{in } d\lambda \text{ from all particles} \\ \text{in } d\forall \text{ into all directions}\end{array}\right) &= \bar{\rho}_\lambda^P K'_p d\forall d\lambda \int_{4\pi} \left\{\frac{1}{4\pi}\int_{4\pi} i'_\lambda \Phi_p d\Omega'\right\} d\Omega \\ &= \bar{\rho}^P K'_p d\forall d\lambda \int_{4\pi} i'_\lambda \left(\frac{1}{4\pi}\int_{4\pi} \Phi_p d\Omega\right) d\Omega' \\ &= \bar{\rho}^P K'_p d\forall d\lambda 4\pi < i_\lambda > \end{aligned} \tag{139}$$

The total inscattered energy given by Eq. (139) exactly balances the outscattered energy given by Eq. (133).

6.11 Radiant Energy Balance and the Gibb Model

The Radiation Transport Equation, integrated over all wavelengths, over the volume $\forall$ in Fig. 16, and over all angles, yields the following radiant energy balance.

$$\begin{aligned}\int_S \vec{q}^R \cdot \hat{n} dS &= K_{a,g}\left[i_b(T_G) - \frac{1}{4\pi}\int_{4\pi} i d\Omega\right] 4\pi\forall \\ &+ \epsilon_P K'_P(i^P_{b,P} - \frac{1}{4\pi}\int_{4\pi} i d\Omega) 4\pi\forall \end{aligned} \tag{140}$$

where Eqs. (102) , (107) , (110) , (122) and (126) have been used, where the volume average symbols have been dropped, and where the cancellation of inscattering with the outscattering terms for the gas (Eqs. (129) and (130)) and for the particles (Eqs. (133) and 139)) have been recognized. Gibb defined the radiant temperature T_R by

$$\frac{1}{4\pi}\int_{4\pi} i d\Omega = < i > = \frac{\sigma T_R^4}{\pi} \tag{141}$$

and by analogy to the radiant heat flux in the diffusion limit

$$\vec{q}_R = -\frac{4\sigma}{3K_e}\vec{\nabla}T_R^4 \tag{142}$$

The diffusion limit exists if the medium is highly absorbing or scattering. These effects enter through the coefficient K_e that is defined as

$$K_e = K_{a,g} + K'_P(\epsilon_P + \rho_P(1 - f)) \tag{143}$$

where

$$f = \frac{1}{4\pi}\int_{4\pi}\frac{1}{4\pi}\int_{4\pi} \Phi_P(\hat{s}\cdot\hat{s}')d\Omega' d\Omega \tag{144}$$

Substituting these equations into Eq. (140) and replacing the black-body intensities by the equivalent temperatures

$$\int_S (-\frac{1}{3K_e}\vec{\nabla}T_R^4)\cdot\hat{n}dS = \left[K_{a,g}(T_G^4 - T_R^4) + \epsilon_P K'_P(\bar{T}_P^4 - T_R^4)\right]\forall \tag{145}$$

It is significant that scattering does not appear as a source or sink of radiant energy in this energy balance. Scattering does, however, affect the transport of radiant energy. This is accounted for in 'diffusion' coefficient K_e.

The essence of Gibb's model is contained in Eqs. (142), (143) and (144). The validity of Eq. (142) is open to question when the medium is not optically dense. The justification for Eq. (143) is unknown to this writer.

The net radiant energy leaving the gas, $\dot{Q}^R$ in Eq. (58), is just the excess of gas emission minus absorption.

$$\dot{Q}^R_G = 4\pi \forall K_{a,g}(T^4_G - T^4_R)\frac{\sigma}{\pi} \tag{146}$$

This can be found once T^4_R has been evaluated.

The net radiation leaving a particle (emission minus absorption) is

$$\begin{aligned} \dot{Q}^R_p &= \epsilon_p(\pi i_b(T_p) - \pi < i >)4\pi r_p^2 \\ &= \epsilon_p(\sigma T^4_p - \sigma T^4_R)4\pi r_p^2 \end{aligned} \tag{147}$$

This source term is required in the particle thermal energy equation, Eq. (84).

6.12 Boundary Conditions for Gibbs' Model

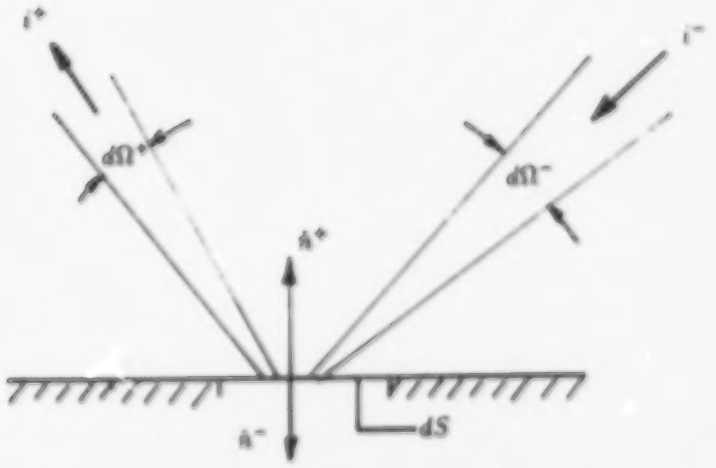

Figure 21: Boundary condition application for Gibb's radiation model.

From Eq. (142), the heat flux into the surface is

$$\vec{q}_R \cdot \hat{n}^- = -\frac{4}{3}\frac{\sigma}{K_e}\frac{\partial T_R^4}{\partial n^-} \tag{148}$$

But the net radiant flux leaving the surface is the difference between the outcoming and ingoing radiant energy

$$-\frac{4}{3}\frac{\sigma}{K_e}\frac{\partial T_R^4}{\partial n^+} = \int_{\substack{2\pi \\ \hat{s}^+ \cdot \hat{n}^+ > 0}} i^+ \hat{s}^+ \cdot \hat{n}^+ d\Omega^+$$

$$- \int_{\substack{2\pi \\ \hat{s}^- \cdot \hat{n}^- > 0}} i^- \hat{s}^- \cdot \hat{n}^- d\Omega^- \tag{149}$$

or

$$-\frac{4}{3}\frac{\sigma}{K_e}\frac{\partial T_R^4}{\partial n^+} = \pi i^+ - \pi i^- \tag{150}$$

It has been assumed that i^- is independent of direction (this will be a poor approximation unless the medium is optically dense). For a gray surface, i^+ will be independent of direction. From the definition of T_R^4, Eq. (141),

$$4\sigma T_R^4 = \int_{4\pi} i d\Omega = \int_{\substack{2\pi \\ \hat{s}^+ \cdot \hat{n}^+ > 0}} i^+ d\Omega^+ + \int_{\substack{2\pi \\ \hat{s}^- \cdot \hat{n}^- > 0}} i^- d\Omega^- \tag{151}$$

Again employing the assumption that i^+ and i^- are directionally independent

$$\sigma T_R^4 = \frac{\pi}{2} i^+ + \frac{\pi}{2} i^- \tag{152}$$

The radiant energy that leaves the surface is the sum of the reflected and emitted energy:

$$\int_{\substack{2\pi \\ \hat{s}^+ \cdot \hat{n}^+ > 0}} i^+ \hat{s}^+ \cdot \hat{n}^+ d\Omega^+ = \epsilon_w \sigma T_w^4 + \rho_w \int_{\substack{2\pi \\ \hat{s}^- \cdot \hat{n}^- > 0}} i^- (\hat{s}^- \cdot \hat{n}^-) d\Omega^- \tag{153}$$

Invoking the approximation again that i^+ and i^- are directionally independent

$$i^+ \pi = \epsilon \sigma T_w^4 + \rho_w \pi i^- \tag{154}$$

Equations (152) and (154) can be solved for i^- and i^+, with the result that

$$\pi(i^+ - i^-) = \frac{2\epsilon_w \sigma}{(2-\epsilon_w)}[T_w^4 - T_R^4] \tag{155}$$

The relation $\rho_w = 1 - \epsilon_w$ has been used to eliminate ρ_w. Substituting Eq. (155) into (150) and rearranging

$$-\frac{\partial T_R^4}{\partial n^+} = \frac{3K_e\epsilon_w}{2(2-\epsilon_w)}[T_w^4 - T_R^4] \tag{156}$$

6.13 Discussion of Gibb's Model

The Gibb model approximates the heat flux by the gradient of the radiant temperature T_R^4, which appears as a new variable. Equation (145) is the conservation equation for T_R^4. The boundary condition for T_R^4 is given by Eq. (156). This equation is equivalent to a Robin condition in convective heat transfer. If the wall temperature is known, this equation yields the wall value of T_R^4. If the net radiant flux leaving the wall ($\pi i^+ - \pi i^-$) is known, then Eq. (150) gives the value of T_R^4 at the wall and the Eq. (156) gives the wall temperature.

When only the wall heat flux $q_w[W/m^2]$ is specified, there is a coupling between convection and radiation that determines the wall temperature. If the convective heat transfer is held fixed when radiation is calculated and the radiation heat transfer is held fixed when the convective heat transfer is calculated, slow convergence can result unless either convection or radiation is dominant. The boundary conditions must be linearized such that changes in convective heat transfer are included in an appropriate way in the radiation boundary conditions, and changes in radiant energy are included when the boundary conditions for convective heat transfer are applied.

The Gibb model has been compared to a more accurate solution of the radiation transport equation by Chui and Hughes (1991). The model was found to be remarkably accurate when the angular distribution of radiation intensity was smooth. For regions in which radiation intensity is very peaked around a given direction, radiant wall fluxes were found to be poorly predicted.

7 FINITE VOLUME MODEL FOR PREDICTION OF RADIANT HEAT TRANSFER

7.1 Introduction

The Gibb model of radiant energy transfer provides quite good predictions far from the combustion region, but poor accuracy is expected near the burner. Unfortunately it is precisely this near burner zone where accurate predictions are needed most.

Early in the present study (in the Fall of 1987) a literature review was undertaken to establish if alternative radiation models were available that would provide the desired accuracy. It was required that the radiation model converge to the solution of the Radiation Transfer Equation as the computational mesh is refined, that it be applicable on the same non-orthogonal, boundary-fitted computational mesh as used to solve the fluid flow equations, that it be useful for the full range of optical thickness, and that it be able to treat both isotropic and anisotropic scattering. Guidance in the literature search was provided by the reviews of Viskanta and Mengüç (1984, 1987) and Howell (1988).

An early conclusion of this study was that no practical models exist that account for the spectral properties of the radiation; the medium is always treated as gray. If radiation in the flame is dominated by the soot or coal particles, the gray approximation is quite reasonable. To account for the spectral dependence of the gaseous radiation introduces tremendous complexity. For these reasons, the gray-medium approximation was accepted as both necessary and marginally reasonable.

The Monte Carlo method was eliminated because of its high computational cost and its incompatibility with the computational procedures used to solve the fluid motion. The Discrete Transfer Method of Lockwood and Shah (1981) fulfills the criteria except that it shares little with the fluid flow solution procedure and that scattering is difficult to treat. Many Flux methods exist that can be applied on the kinds of computational meshes of interest, but these methods do not converge to the solution of the Radiation Transfer Equation. The most widely applied method is the Discrete Ordinates Method. It appears that this method is only applicable on a Cartesian or cylindrical mesh, that it does not conserve radiant energy, and that convergence is very slow when the medium becomes optically dense.

To address the need for a radiation model with the desired properties, the Finite Volume Method (FVM) was conceived and developed as part of the present contract.

This method shares the philosophy frequently used to discretize and solve fluid flow equations, so uses the same computational mesh and the results approach the solution of the Radiation Transfer Equation as the mesh is refined. Any optical density can be treated, although a special implicit solution method becomes necessary for large optical densities. In such cases, the FVM captures exactly the Rosseland diffusion limit (Siegel and Howell (1981)) as the optical density becomes large. The method handles both isotropic and anisotropic scattering in a natural way. The method fully conserves radiant energy over discrete solid angles, and conserves total radiant energy. The only difficulty with the model, besides the gray medium limitation, is that special care is required when the boundaries of the domain are complex, but this difficulty has also been largely overcome.

The underlying method has appeared in the literature (Raithby and Chui (1990)); this paper is attached as Appendix B. The method was studied and enhanced by Chui (1990) in a PhD thesis that was also partially supported by the present contract. A paper (in press) on the application of the FVM to axisymmetric problems appears here as Appendix C, another paper (also in press) that refines the implicit solution method for strongly participating media appears as Appendix D, and a paper (draft version) on the application of the method on non-orthogonal meshes is included as Appendix E.

These papers do not include the effect of particles in the medium. This chapter contains a very brief development of the method that includes this effect.

7.2 Differential Radiation Equation

The Radiation Transfer Equation (Eq.(98)) is rewritten here in the form required for development of the FVM. The medium is assumed to be gray. For the radiant intensity i at location $\vec{r}$, in the direction of the unit vector $\hat{s}$, and within the solid angle, $d\Omega$, the rate of increase of i with distance s is

$$\frac{di}{ds} = K_{a,g}(i_{b_g} - i) - \sigma_{s,g}(i - \bar{i}) + \bar{e}_p^P K_p'(\bar{i}_{b,p}^P - i) - \bar{\rho}^P K_p'(i - \bar{i}_P) \qquad (157)$$

where

$$\bar{i} = \frac{1}{4\pi}\int_{4\pi} i(\vec{r},\hat{s}')\Phi(\hat{s}',\hat{s})d\Omega' \qquad (158)$$

$$\bar{i}_P = \frac{1}{4\pi}\int_{4\pi} i(\vec{r},\hat{s}')\Phi_P(\hat{s}',\hat{s})d\Omega' \qquad (159)$$

and where the superscript $^{-P}$ denotes the average overall particles defined by Eq. (120).

Equations of Motion for Reacting, Particle-Laden, Flows

G. D. Raithby
Thermal Science Ltd.
187 Castlegate Crescent, Waterloo, Ontario, N2L 5V1

Report Submitted to:

P. M. J. Hughes
Energy, Mines and Resources, CANMET, ERL Division
555 Booth Street, Ottawa, Ontario, K1A 0G1

Partial report on work supported by Unsolicited Proposal Contract
"COMPUTER MODELLING OF COAL COMBUSTION", UP-T6-022
Contract Serial No. 23440-7-9130/01 SQ
SSC File No. 03 SQ.23440-7-9130

December 1991

Executive Summary of Contract

Funding under this contract supported work both at Imperial College in England and at Thermal Science Ltd. (TSL) in Waterloo, Ontario. The overall objectives were to enhance mathematical models describing the combustion of low volatile coals, and to acquire the modelling technology in Canada.

About 60% of the total contract effort was undertaken at Imperial College under the direction of Dr. F. Lockwood. In this work the model for low volatile combustion was improved and a large number of computer simulations were made. These results will be presented in a separate report.

TSL has carefully studied the Lockwood code, has run computer simulations for both cold and reacting flows, has checked the model by deriving the equations and evaluating the assumptions used, and has developed and tested a new radiation model.

For the complex particle-laden flows of current interest, no source could be found which derived the equations of motion and heat transfer, and which listed reasonable and/or necessary approximations. The objective of this final report is to provide this information. It is hoped that the report will serve as a reference document for further development of coal combustion models.

NOMENCLATURE

$A_{\lambda,P}$	decrease of spectral intensity due to particle absorption, Eq. (98), $[W/m^2\ sr\ m\ \mu m]$
$\bar{C}_P$	specific heat of particle, Eq. (83), [J/kg K]
e	internal energy, [J/kg]
e_P	internal energy of particle, [J/kg]
$\dot{e}$	total energy (internal + kinetic + potential), [J/kg]
$E_{\lambda,P}$	increase of intensity due to particle emission, Eq. (98), $[W/m^2 sr m\mu m]$
h	enthalpy $= e + p/\rho$ [J/kg]
h_{ox}	enthalpy of the oxidant for the heterogenous particle reaction, [J/kg]
$h_{P,fu}$	enthalpy of the particle that is consumed in heterogenous reaction, [J/kg]
$h_{P,vol}$	enthalpy of the particle that becomes volatiles, [kJ/kg]
h_{vol}	enthalpy of the volatiles that leave the particle, [J/kg]
i	radiation intensity, $[W/m^2 sr]$
$\bar{i}$	inscattering intensity in gas, Eq. (158), $[W/m^2 sr]$
i_b	black body intensity, $[W/m^2 sr]$
$i_{b\lambda}$	spectral black body intensity, $[W/m^2 sr\mu m]$
i_λ	spectral radiation intensity, $[W/m^2 sr\mu m]$
$K_{a,g}$	absorption coefficient for gas, $[1/m]$
K_e	Gibb's coefficient, Eq. (143), $[1/m]$
K'_P	cross-section of particles per unit volume, Eq. (117), $[m^2/m^3]$
$K_{\lambda a,g}$	spectral absorption coefficient for gas, $[1/m\ \mu m]$
L_H	latent heat of reaction for char combustion, $[J/kg - fuel]$

L_V	latent heat of volatilization, $[J/kg - volatiles]$
$\dot{m}''$	mass flux across boundary, positive in direction of, $\hat{n}[kg/m^2 s]$
$\dot{m}_{fu}$	rate of consumption of fuel from particle, $[kg/s]$
$M_{G,K}$	mass of gas in control volume associated with node K, [kg]
$\dot{m}_G^l$	mass flow rate of gas crossing panel l of control Bvolume, $[kg/s]$
$\dot{m}_{ox}$	mass flow rate of oxidant to a particle, $[kg/s]$
$\dot{m}_P''$	mass flux across boundary of particle, positive in direction of $\hat{n}_P$, $[kg/m^2 - s]$
$\dot{m}_P$	total mass flow rate leaving a particle, $[kg/s]$
M_P	mass of particle, [kg]
$M_{P,1}, M_{P,2}$	mass of particle where it enters and leaves control volume, Fig. 4, [kg]
$M_{P,ash}$	mass of particle that remains as ash, [kg]
$M_{P,fu}$	mass of particle that will be burned in char combustion, [kg]
$M_{P,vol}$	mass of particle that will be volatized, [kg]
$\dot{m}_{vol}$	mass flow rate of volatiles leaving particle, [kg/s]
$n(r_P, T_P)$ $dr_P dT_P$	number of particles with radii within dr_P and temperatures within dT_P, per unit volume, $[no./m^3]$
$\hat{n}$	unit normal at surface in gas control volume, Fig. 1, 2
$\dot{N}_P$	number of particles per unit time that travel a given path through the gas, [no/s]
p	pressure, $[Pa]$
P_i	component of particle momentum in the x_i direction, Eq. (30), [kg m/s]
$\bar{q}^C$	heat flux by conduction in gas either at the boundary of the gas control volume or at the surface of particles, $[W/m^2]$

$\vec{q}^{\,R}$	radiant flux in the gas, $[W/m^2]$
$\dot{Q}^C_{OG}$	total heat transfer by conduction through the boundary S_{OG}, $[W]$
$\dot{Q}^C_I$	total heat transfer by conduction at all particle boundaries or portions of particle boundaries that lie within S_O, $[W]$
$\dot{Q}^R_G$	net transfer of internal energy of the gas within a volume into radiant energy, $[W]$
r_i	i-component of position vector $\vec{r}$, $[m]$
R_i	i-component of the vector to the centre of mass of particle, $[m]$
r_P	radius of parti . $[m]$
S	surface area, $[m^2]$
s_1, s_2	arc length along a given particle path in the gas; Fig. 4, $[m]$
S_I	surface area of all particles, or portions of particles, that lie within S_O, $[m^2]$
S_O	outside surface area of a control volume that contains gas and particles, $[m^2]$
S_{OG}	portion of S_O that is gas, $[m^2]$
S_P	surface area of a particle, $[m^2]$
$\dot{S}^m$	source of internal energy, $[W/m^3]$
S^I_λ	augmentation of radiant intensity due to inscattering, Eq. (98), $[W/m^2\ sr\ m\ \mu m]$
S^O_λ	decrease in radiant intensity due to outscattering, Eq. (98), $[W/m^2\ sr\ m\ \mu m]$
t	time, $[s]$
t_1, t_2	time at which a particle moving on a given particle path traverses control volume boundary, Fig. 4, $[s]$
T_G	temperature of gas, $[K]$
T_R	Gibb's radiation temperature, Eq. (141), $[K]$

T_w	solid wall temperature, $[K]$
u_i	velocity component in the $\hat{e}_i$ direction, $[m/s]$
u_i^{COM}	u_i at the centre-of-mass of particle, $[m/s]$
$\forall$	volume, $[m^3]$
$\vec{V}$	material velocity (solid, liquid, gas), $[m/s]$
$\vec{V}^{COM}$	velocity of centre-of-mass of particle, $[m/s]$
$\forall_G$	portion of $\forall$ that is gas, $[m^3]$
$\forall_K$	volume of control volume associated with node K, $[m^3]$
$\forall_P$	volume of particle, $[m^3]$
$\vec{W}$	velocity of control volume surface. At external control volume surfaces $\vec{W}$ can be chosen by analyst. At boundaries around particle, $\vec{W}$ is assumed to move with the local particle velocity, $[m/s]$
x_i	Cartesian coordinate in the i-direction, $[m]$
ϵ_P	particle emissivity, $[-]$
$\bar{\epsilon}_P^P$	average emissivity of particles in control volume, Eq. (118), $[-]$
ϵ_w	wall emissivity, $[-]$
$\epsilon_{\lambda,P}$	spectral emissivity of particle, $[-]$
$d\lambda$	differential change in wavelength, $[\mu m]$
ρ	material density, $[kg/m^3]$
$\bar{\rho}^P$	average reflectivity of particles in control volume, Eq. (119), $[-]$
σ	Stefan-Boltzmann constant, $[W/m^2K^4]$
$\sigma_{s,g}$	scattering coefficient of gas, $[1/m]$
τ_{ij}	molecular stress in fluid, $[N/m^2]$
ϕ^n	concentration of constituent n, $[kg - n/kg - mixture]$

$\Phi(\hat{s}', \hat{s})$	phase function for scattering, [–]
$d\Omega$	differential solid angle, [sr]

Contents

1 INTRODUCTION 1

2 NOTATION, VOLUME CONSERVATION AND MASS CONSERVATION 3

2.1 Notation 3

2.2 Volume Conservation 5

2.3 Mass Conservation For The Gas 5

2.4 Mass Conservation for a Particle 6

2.5 Source of Mass From Moving Particles 7

3 MOMENTUM CONSERVATION 10

3.1 Gas Momentum Equation 10

3.2 Notes on Discretization of the Gas Momentum Equation 12

3.3 Particle Momentum Equation 14

3.4 Particle Equation in Cylindrical Co-ordinates 17

3.5 Source of Momentum from Moving Particles 19

4 ENERGY CONSERVATION 20

4.1 Differential Equation of Energy Conservation 20

4.2 Gas Energy Equation 20

4.3 Discretization of the Gas Energy Equation 22

4.4 Particle Energy Equation 23

4.5 Source of Energy From Moving Particles 24

4.6 Details of the Particle Energy Balance Including Chemical Reaction 25

5 CONSERVATION OF A CONVECTED AND DIFFUSED SCALAR 29

5.1 Integral Conservation Equation 29

5.2 Discretization of the Concentration Equation 31
5.3 Source of Constituent n From Moving Particles 32

6 DEVELOPMENT OF GIBB'S DIFFUSION MODEL FOR RADIATION 33

6.1 Introduction 33
6.2 Radiation Transport Equation 33
6.3 Integration of the di_λ/ds Term 35
6.4 Integration of the Gas Emission Term 36
6.5 Integration of the Gas Absorption Term 36
6.6 Particle Emission 37
6.7 Particle Absorption 39
6.8 Gas Scattering 40
6.9 Particle Outscattering 41
6.10 Particle Inscattering 42
6.11 Radiant Energy Balance and the Gibb Model 44
6.12 Boundary Conditions for Gibbs' Model 45
6.13 Discussion of Gibb's Model 47

7 FINITE VOLUME MODEL FOR PREDICTION OF RADIANT HEAT TRANSFER 48

7.1 Introduction 48
7.2 Differential Radiation Equation 49
7.3 Integral Equation for Intensity 50
7.4 First Level of Discretization of the Intensity Equation 51
7.5 Internal Energy Source Terms due to Radiation 53

8 CLOSING COMMENTS 54

9 APPENDIX A: REVIEW OF INTEGRAL RELATIONS 56

10 Appendix B - A Finite-Volume Method for Predicting Radiant Heat Transfer in Enclosures with Participating Media 61

11 Appendix C - Prediction of Radiant Exchange in Cylindrical Enclosures with the Finite-Volume Method 62

12 Appendix D - Implicit Solution Method to Improve Convergence Rate in Radiative Heat Transfer Problems 63

13 Appendix E - Application of the Finite-Volume Method to Non-Orthogonal Computational Meshes 64

List of Figures

1	Notation for a control volume containing gas and particles.	3
2	Control volume for a single particle.	4
3	Conversion of mass loss from moving particles to mass gain in control volume.	7
4	One particle path traversing a control volume.	9
5	Definition sketch.	12
6	Control volume K used to obtain the discrete equation for the nodal velocity $u_{i,k}$.	13
7	Definition sketch for derivation of particle momentum equation.	14
8	Circular cylinder co-ordinate system.	18
9	Notation for energy balance on gas.	21
10	Notation for discrete control volume K.	23
11	Nomenclature for particle energy balance with combustion and devolatilization.	25
12	Energy balance to relate energy release by reaction at temperatures T_P to the heat of reaction at T_o.	27
13	Energy balance to relate energy required for devolatilization at temperature T_P to that at T_o.	28
14	Definition sketch for scalar conservation.	30
15	Notation for discrete control volume K.	31
16	Nomenclature for radiation heat transfer derivation.	34
17	Nomenclature for particle emission	37
18	Nomenclature for particle absorption.	39
19	Nomenclature for particle outscattering.	41
20	Nomenclature for particle inscattering.	42
21	Boundary condition application for Gibb's radiation model.	45
22	Nomenclature for radiation transfer equation.	50

23 Discrete volume $\forall_K$ surrounding node K, and discrete solid angle Ω^m. 51
24 Definition sketch of control volume. 56
25 Figure showing fluxes across differential control volume faces. 59
26 Figure for application of Gauss' Theorem to a scalar. 60

1 INTRODUCTION

Under the direction of P. M. J. Hughes, CANMET sponsored research and code development by the Lockwood Group at Imperial College. This work culminated in a final report by Lockwood and Rizvi in 1985. In September 1987, a contract was begun by Thermal Science Ltd. that had two objectives:

1. The first objective was to further develop the axisymmetric Lockwood code, and to make a comprehensive set of runs using this code, for low volatile coal. Both these tasks were done under subcontract with Imperial College.

2. The second objective was to acquire the technology in Canada, via Thermal Science Ltd., so that future development work could be undertaken here.

A separate report related to the first objective will be issued by Imperial College. To achieve the second objective, every detail of the Lockwood code FAFNIR[1] has been studied, and the code has been run on several problems for both cold and combusting flows. Furthermore, comparisons have been made between the cold-flow predictions of an early version of FAFNIR and a similar code from the University of Waterloo.

Although a thesis by Rizvi (1985) provided some of the theoretical underpinnings of the code, many details related to the mass, momentum, thermal energy and radiant energy equations are not available. It is crucial to further development of the technology that the underlying equations be correct and fully understood, and that each approximation introduced be clearly stated. For many reacting flow problems, the computational grid should be allowed to expand and/or contract with the external boundaries. Furthermore, the internal boundaries of the gas control volume, around the solid or liquid particles, must follow the interface. The integral equations of motion, that serve as the starting point for the discrete solution method, should therefore include the effect of moving boundaries. One objective of this report is to provide a clear and detailed derivation of the equations of motion, including moving control-volume boundaries.

Perhaps the weakest part of FAFNIR is the radiation model. A literature review undertaken near the beginning of this study concluded that no fully satisfactory radiation model existed. A major effort in the contract was therefore devoted to the development of a new radiation model: the Finite Volume Method. The fundamental framework for the method and some applications were presented by Raithby and

[1] References are tabulated at the end of the main body of this report

Chui (1990); this work was totally supported by this contract. This model was later refined and extensively tested in a PhD thesis by E. Chui at the University of Waterloo in work that was partly supported by the present contract. This model has proved to be extremely powerful for solving radiation problems, and is believed to constitute a significant contribution to the field. Appendices B, C, D and E describe the model in detail. In Chapter 7 the model has been extended to include the effect of particulates on the radiation heat transfer.

This report does not include a detailed development of the chemical reaction models. The reaction models used in FAFNIR are extremely simple, and details have already been provided by Rizvi (1985) and other Imperial College reports.

2 NOTATION, VOLUME CONSERVATION AND MASS CONSERVATION

2.1 Notation

The problems of current interest involve a gas mixture and a second phase of solid or liquid "particles" that exchange mass, momentum, energy, and species with the gas. Chemical reactions can also occur in both phases. The conservation equations for this complex system are required for the gas and for the particles. These equations are written for a control volume that contains particles both inside the volume and straddling its boundary, as shown in Fig. 1. It is important that the outer surface of the control volume be permitted to arbitrarily distort in time. Also the particles change their volumes with time, with the result that the gas volume within the control volume changes even when the outer control volume boundary is fixed.

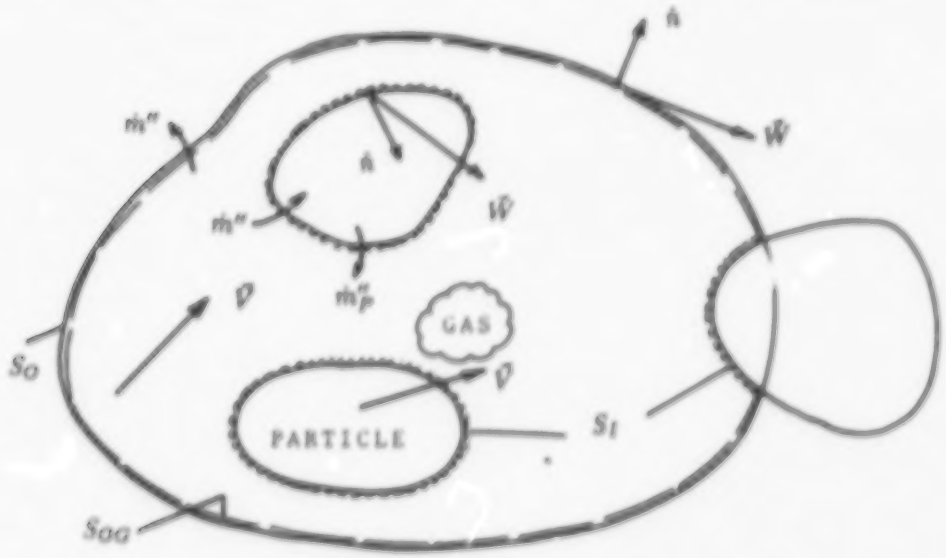

Figure 1: Notation for a control volume containing gas and particles.

The notation adopted here is defined in Fig. 1. S_O (solid line) is the outside surface area of the control volume, S_{OG} (long dashes) is the outside surface area that lies in the gas, and S_I is the total particle surface area within the control volume (short dashes). Note that the control surfaces lie on the gas side of the particle-gas

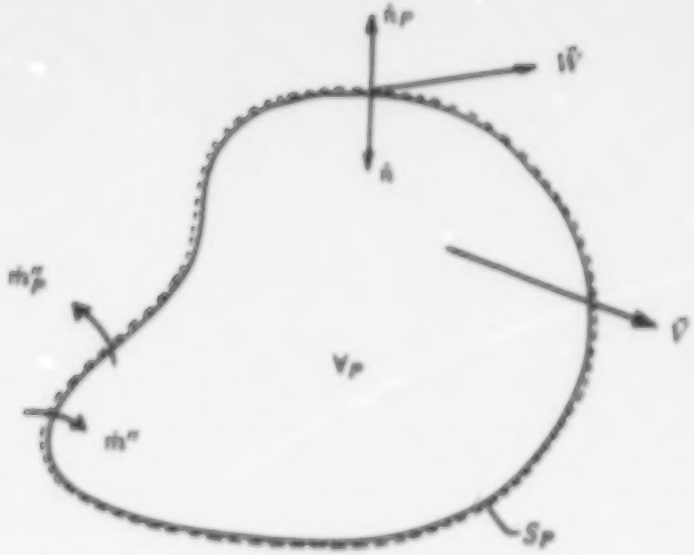

Figure 2: Control volume for a single particle.

interface. The control volume containing both gas and particles has volume $\forall$, and the gas control volume (that excludes the particles) has volume $\forall_G$. The unit normal at the control surface is $\hat{n}$, and is defined as positive when it is outward with respect to the gas control volume, as shown in Fig. 1.

The local control surface velocity is defined as $\vec{W}$, and the local material (liquid, solid or gas) velocity at any point is $\vec{V}$. Because the control volume boundaries around the particles are defined to lie at the interface , the $\vec{W}$ velocity on these surfaces are defined by the particle motion. In contrast, the $\vec{W}$ velocity at the S_O surface is specified by the analyst. The local mass flux $[kg/s - m^2]$ crossing the boundary in the direction of $\hat{n}$ is $\dot{m}''$.

The control volume for a single particle is shown in Figure 2. The outward unit normal is $\hat{n}_P = -\hat{n}$, and the local material and control surface velocities are $\vec{V}$ and $\vec{W}$ respectively, as already described. If the particle is devolatizing and/or shrinking or swelling $\vec{W}$ will not be generally equal to $\vec{V}$ at the particle boundary. The volume of a particle is $\forall_P$, and its surface area is S_P. S_P is part of the total internal surface area S_I described above. The local mass flux $[kg/m^2 - s]$ leaving the particle is $\dot{m}''_P$ (i.e., positive in the direction of $\hat{n}_P$). Note that at the particle surface $\dot{m}''$ (which is positive in the $\hat{n} = -\hat{n}_P$ direction) is the negative of $\dot{m}''_P$.

2.2 Volume Conservation

Applying Leibnitz rule (Eqs. (171) and (172) in Appendix A) with $f = 1$ to the particle control volume in Figure 2, the rate of volume increase of the particle is related to the velocity of its control surface by

$$\frac{d\forall_p}{dt} = \int_{S_p} \vec{W} \cdot \hat{n} dS = -\int_{S_p} \vec{W} \cdot \hat{n} dS \tag{1}$$

Each term in Eq. (1) is zero when the particle volume remains constant.

Applying Eqs. (171) and (172) to the gas control volume, again with $f = 1$, gives the following equation for the rate of increase of the gas volume (Fig. 1).

$$\frac{d\forall_G}{dt} = \int_{S_{CG}} \vec{W} \cdot \hat{n} dS + \int_{S_I} \vec{W} \cdot \hat{n} ds \tag{2}$$

If the particles do not change size, the second integral is zero for particles entirely within $\forall$, but it will have a non-zero value for the particles that straddle the surface S_O. This is reasonable since a particle leaving through S_O leaves more room within $\forall$ for the gas.

2.3 Mass Conservation For The Gas

Applying Leibnitz rule with $f = \rho(x_i, t)$ to the gas volume $\forall_G$ in Fig. 1 yields

$$\frac{d}{dt}\left(\int_{\forall_G} \rho d\forall\right) \equiv \frac{dM_G}{dt} = \int_{S_{CG}+S_I} \rho \vec{W} \cdot \hat{n} dS + \int_{\forall_G} \frac{\partial \rho}{\partial t} d\forall \tag{3}$$

The continuity equation for an infinitesimal gas control volume is (Panton, 1984)

$$\frac{\partial \rho}{\partial t} + \frac{\partial}{\partial x_j}(\rho u_j) = 0 \tag{4}$$

The last term in Eq. (3) therefore becomes

$$\int_{\forall_G} \frac{\partial \rho}{\partial t} d\forall = -\int_{\forall_G} \frac{\partial}{\partial x_j}(\rho u_j) d\forall = -\int_{S_{CG}+S_I} \rho \vec{V} \cdot \hat{n} dS \tag{5}$$

where the last equality is a result of Gauss' Theorem, Eq. (176) in Appendix A. Substituting Eq. (5) into Eq. (3) results in the following integral equation for mass conservation of the gas

$$\frac{dM_G}{dt} = \int_{S_{OO}+S_I} \rho(\vec{W} - \vec{V}) \cdot \hat{n} dS = - \int_{S_{OO}+S_I} \dot{m}'' dS \tag{6}$$

Some simple examples follow.

Example 1: $S_I = 0$ (no particles), $\vec{V} = 0$

$$\frac{dM_G}{dt} = \int_{S_O} \rho \vec{W} \cdot \hat{n} ds$$

In this case, the extra mass captured in the control volume is a result only of displacing the control surface outward through the gas.

Example 2: $S_I = 0$ (no particles), $\vec{W} = \vec{V}$
If the control volume boundary moves at the fluid velocity,

$$\frac{dM_G}{dt} = 0$$

This result is obviously correct because mass can't be transferred across the control volume surface when the surface and material velocities are the same.

2.4 Mass Conservation for a Particle

The mass conservation equation for the particle is derived following exactly the same steps as for the gas, except the integration is over the particle volume $\forall_p$. By Leibnitz rule

$$\frac{d}{dt} \int_{\forall_p} \rho d\forall = \frac{dM_P}{dt} = \int_{\forall_p} \frac{\partial \rho}{\partial t} d\forall + \int_{S_p} \rho \vec{W} \cdot \hat{n}_p dS \tag{7}$$

The differential equation for mass conservation is

$$\frac{\partial \rho}{\partial t} + \frac{\partial}{\partial x_j}(\rho u_j) = 0 \tag{8}$$

Substituting Eq. (8) into (7), and using Gauss' theorem, results in

$$\frac{dM_P}{dt} = \int_{S_p} \rho(\vec{W} - \vec{V}) \cdot \hat{n}_p dS \tag{9}$$

or

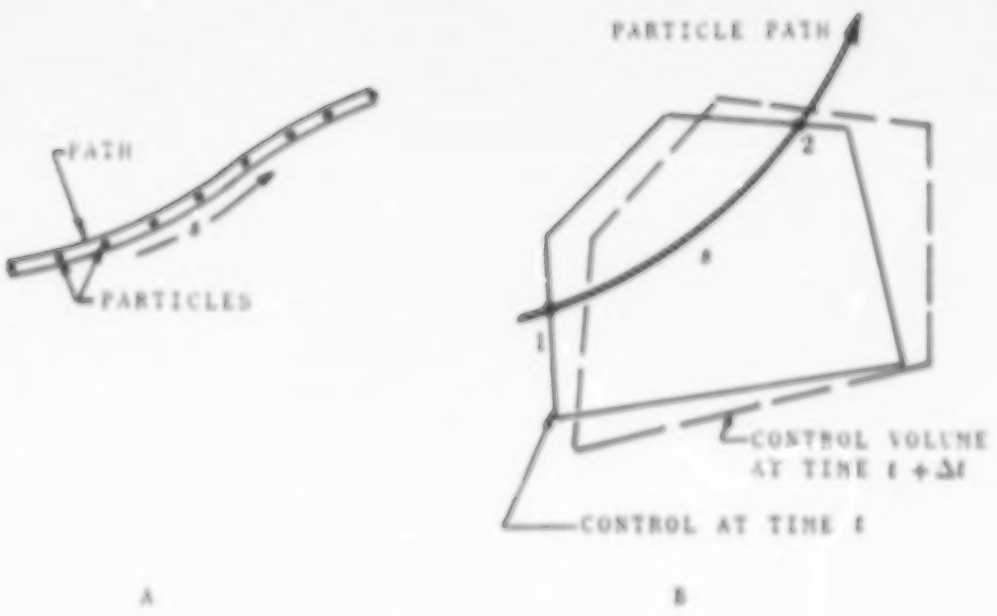

Figure 3: Conversion of mass loss from moving particles to mass gain in control volume.

$$\frac{dM_P}{dt} = -\int_{S_P} \dot{m}''_P dS \equiv -\dot{m}_P \tag{10}$$

In the last equation, $\dot{m}_P$ is the total rate of mass loss by the particle, defined in Figure 2.

2.5 Source of Mass From Moving Particles

The mass (as well as momentum, species and energy) balance on particles is applied using a control volume that follows each particle. The control volumes for the gas do not move with the particles, so a conversion is required to compute the "source" of mass, species, momentum, energy, etc. in the gas control volume that results from material transport across the particle interfaces. This section derives the simple conversion for mass.

In steady state, particles are being constantly injected into the flow and, because of turbulence, each particle will take a different path. Because it isn't practical to compute each path, a (large) number of paths are computed and it is assumed that $\dot{N}_P$ particles per second are released for a given path. A number of particles are shown along one such path in Figure 3A. The time between particles is $1/\dot{N}_P$, the local distance between particles is $|\vec{V}_P|/\dot{N}_P$ (where $\vec{V}_P$ is the velocity of the centre

of mass of the particle) so the number of particles per unit length along their path is $\dot{N}_P/|\vec{V}_P|$. Each particle loses mass at the rate $\dot{m}_P$. The total rate of mass loss, from the particles associated with this path, that is transferred to the gas during Δt within $\forall$ is therefore

$$\left\{\begin{array}{l}\text{Total rate of mass}\\ \text{transfer to gas within}\\ \forall \text{ from one particle}\\ \text{path in } \Delta t\end{array}\right\} = \int_{s_1(t)}^{s_2(t)} \frac{\dot{m}_P \dot{N}_P}{|\vec{V}_P|} ds \tag{11}$$

where s is distance along the path.

To find the total mass transferred from all particles within a control volume to the gas, Eq. (11) would have to be summed over all particle paths that traverse the control volume.

The mass conservation equation for the gas, Eq. (6), therefore becomes

$$\frac{dM_G}{dt} = -\int_{S_{CS}} \dot{m}'' dS + \sum_k \left\{\int_{s_1(t)}^{s_2(t)} \frac{\dot{m}_P \dot{N}_P}{|\vec{V}_P|} ds\right\}_{\text{path } k} \tag{12}$$

where k is the path number shown in Fig. 4A.

This integral over the path in Eqs. 11 and 12 can be simplified for special cases. In Fig. 4A, a particle that crosses at point 1 at time t_1 leaves at point 2 at time t_2. The velocity in Eq. (11) can be approximated as $(s_2 - s_1)/(t_2 - t_1)$, and $\dot{m}_P(t_2 - t_1) \approx (M_{P,1} - M_{P,2})$, so the integral in Eq. (11) can be approximated as

$$\left\{\begin{array}{l}\text{Total rate of mass}\\ \text{transfer to gas within}\\ \forall \text{ from one particle}\\ \text{path in } \Delta t\end{array}\right\} \approx (M_{P,1} - M_{P,2})\dot{N}_P \Delta t \tag{13}$$

For the strategy adopted by Imperial College (Rizvi,1985), a particle is tracked from A to B and spends only a fraction of its flight within the control volume of interest (see Fig. 4B). In this case the integral reduces to

$$\left\{\begin{array}{l}\text{Total rate of mass}\\ \text{transfer to gas within}\\ \forall \text{ from one particle}\\ \text{path in } \Delta t\end{array}\right\} \approx (M_{P,A} - M_{P,B})\dot{N}_P \frac{(t_2 - t_1)}{(t_B - t_A)} \Delta t \tag{14}$$

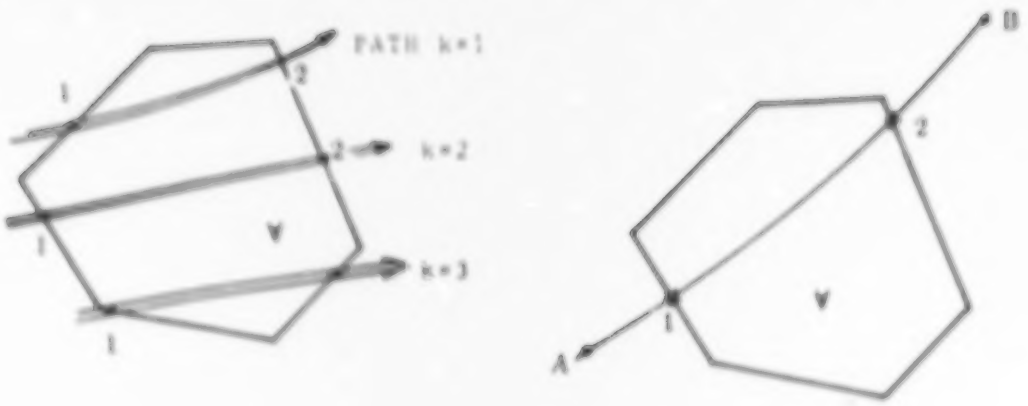

Figure 4: One particle path traversing a control volume.

where t_1, t_2, t_A and t_B are the times when one particle is at points 1, 2, A and B, respectively.

3 MOMENTUM CONSERVATION

The equations expressing conservation of momentum for the gas and for the particle are derived in this chapter. The equations for transfer of momentum between the phases are also developed.

3.1 Gas Momentum Equation

Applying the Leibnitz Rule (Eqs. (171) and (172)) with $f = \rho u_i$ to the gas volume in Fig. 1,

$$\frac{d}{dt}\int_{V_g} \rho u_i dV = \int_{S_{g1}+S_2} \rho u_i \vec{W}\cdot d\vec{A} + \int_{V_g} \frac{\partial}{\partial t}(\rho u_i) dV \tag{15}$$

The momentum equation for an infinitesimal gas control volume is (Panton, 1984):

$$\frac{\partial}{\partial t}(\rho u_i) = -\frac{\partial}{\partial x_j}(\rho u_j u_i) - \frac{\partial p}{\partial x_i} - \frac{\partial \tau_{ji}}{\partial x_j} + f_i^B \tag{16}$$

where p, τ_{ji} and f_i^B are the pressure, the surface stress and volumetric body forces on the fluid in the control volume respectively. Using Eq. (16), the last term in Eq. (15) becomes

$$\int_{V_g} \frac{\partial}{\partial t}(\rho u_i) dV = \int_{V_g} \left(-\frac{\partial}{\partial x_j}(\rho u_j u_i) - \frac{\partial p}{\partial x_i} - \frac{\partial \tau_{ji}}{\partial x_j} + f_i^B \right) dV \tag{17}$$

$$= -\int_{S_{g1}+S_2} (\rho u_i \vec{V}\cdot\vec{n} + p n_i + \tau_{ji} n_j) dA + \int_{V_g} f_i^B dV \tag{18}$$

where the volume integral has been replaced with the surface integral using Gauss' Theorem (Eqs. (176) or (179)). Substituting Eq. (18) into (16) results in the following integral equation for conservation of i-momentum.

$$\frac{d}{dt}\left(\int_{V_g} \rho u_i dV\right) = \int_{S_{g1}+S_2} \rho u_i (\vec{W}-\vec{V})\cdot d\vec{A} - \int_{S_{g1}+S_2} p\,\delta_i \cdot d\vec{A} - \int_{S_{g1}+S_2} \tau_{ji}(\vec{n}\cdot\delta_j) dA + \int_{V_g} f_i^B dV \tag{19}$$

where δ_j denotes the unit vector in the x_j direction.

A detailed examination of the terms follows.

$\int_{S_{CV}+S_I} u_i(\rho(\vec{W}-\vec{V})\cdot \hat{n}dS)$ — The term in parenthesis is the mass flow that crosses the surface area dS into V_{CV}. This mass flow times u_i is the i-momentum transport across dS. The integral is therefore the net i-momentum transported through the boundaries of the gas control volume V_{CV} from the particles and from the gas outside V.

$\int_{S_{CV}+S_I} p(-\hat{n})\cdot \hat{e}_i dS$ — This is the component of the pressure force in the i-direction acting on the gas at the surface of V_{CV}.

$-\int_{S_{CV}+S_I} \tau_{ji}\hat{n}\cdot\hat{e}_i dS$ — This is the component of viscous force in the i-direction acting on the boundary of V_{CV}.

$\int_{V_{CV}} f_i^B dV = F_i^B$ — The component of the total body force in the i-direction acting on the gas within V_{CV}.

$\frac{d}{dt}\left(\int_{V_{CV}} \rho u_i dV\right)$ — The rate of increase of i-momentum with time for all material within V_{CV}.

The momentum carried with the mass flow from the particles through S_I into the gas is represented as follows

$$\int_{S_I} u_i(\rho(\vec{W}-\vec{V})\cdot\hat{n}dS) = \int_{S_I} u_i \dot{m}''_p dS = -\int_{S_I} u_i \dot{m}'' dS \tag{20}$$

where $\dot{m}''_p$ is the mass flow rate leaving the particle surface per unit surface area, positive in the direction of $\hat{e}_p = -\hat{n}$ (see Fig. 5). The pressure and shear stresses acting on S_I represent the drag interaction between the gas and particles. Letting the force $\vec{F}_D^P$ be the drag force on particle P, or the portion of particle P that lies within S_{CV}, and substituting into Eq. (19),

$$\begin{aligned}\frac{d}{dt}\left(\int_{V_{CV}} \rho u_i dV\right) &= \int_{S_{CV}} -u_i \dot{m}'' dS - \int_{S_{CV}} (p\hat{e}_i + \tau_{ji}\hat{e}_j)\cdot\hat{n}dS + F_i^B \\ &+ \int_{S_I} \dot{m}''_p u_i dS - \sum_P \vec{F}_D^P \cdot \hat{e}_i\end{aligned} \tag{21}$$

The i-component of the drag force on particle P is defined as

$$F_{iD}^P = \vec{F}_D^P \cdot \hat{e}_i \tag{22}$$

The drag force on all of particle P is usually approximated by

Figure 5: Definition sketch.

$$F_D^P = C_D A_P^P \frac{1}{2}\rho |\vec{v}_G - \vec{v}_P| (\vec{v}_G - \vec{v}_P) \tag{23}$$

where A_P^P is the projected area of the particle normal to $\vec{F}$, $\vec{v}_G$ is a representative gas velocity in the vicinity of the particle, $\vec{v}_P$ is the velocity of the centre of mass of particle P, ρ is the gas density and C_D is the (presumed known) drag coefficient.

3.2 Notes on Discretization of the Gas Momentum Equation

Equation (21), for the control volume K shown in Fig. 6, can be approximated by

$$\frac{d}{dt}(M_{G,K} u_{i,K}) + \sum_l m_G^l u_i^l - \sum_l F_i^l = F_i^B + \sum_P m_P u_{i,P} - \sum_P F_{i,P}^D \tag{24}$$

where superscript l denotes the surface panel of the control volume, m_G^l is the mass flow rate of the gas (positive in the direction of δ) crossing panel l, F_i^l is the net surface force on the gas over panel l, F_i^B is the body force on the gas in direction i, and the last two terms represent the momentum transport to, and drag force on, the gas from the particles within $\forall_K$. The mass flow, velocity and surface force for each panel must be expressed in terms of the nodal variables to close the equation set, but standard methods are available for doing this, so these will not be discussed here.

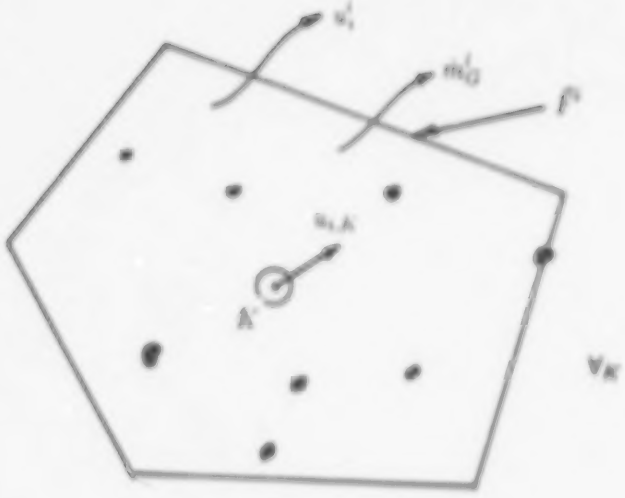

Figure 6: Control volume K used to obtain the discrete equation for the nodal velocity $u_{i,k}$.

From Eq. (6), the partially discretized mass equation is

$$\frac{dM_{G,K}}{dt} + \sum_j \dot{m}_G^j = \sum_p \dot{m}_P \tag{25}$$

Multiplying Eq. (25) by the nodal velocity $u_{i,K}$ and subtracting the result from Eq. (24)

$$M_{G,K}\frac{du_{i,K}}{dt} = -\sum_j \dot{m}_G^j(u_i^j - u_{i,K}) + \sum_j F_i^j + F_i^B + \sum_p \dot{m}_P(u_{i,P-surf} - u_{i,K}) - \sum_p^* F_{i,P}^D \tag{26}$$

The source of momentum from the particles to the gas involves the difference between the u_i velocity at the particle surface (i.e., $u_{i,P-surf}$) and the u_i velocity at the node (i.e., $u_{i,K}$). This term is often written and coded incorrectly.

In summary, Eq. (26) states that the mass times acceleration of the gas in i-direction equals the net i-momentum of gas transported in through the external control volume surfaces, plus the i-component of all forces on the gas at the external control volume surfaces, plus the i-component of the body force, plus the

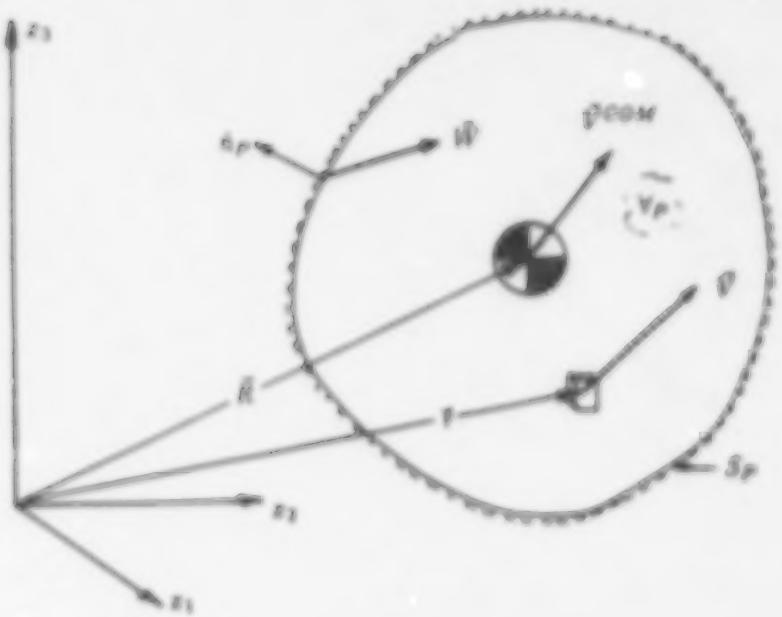

Figure 7: Definition sketch for derivation of particle momentum equation.

i-momentum transported from the particles to the gas, minus the sum over all particles of the i-component of the drag force from the gas on each particle, or portion of particle, that lies within the control volume.

3.3 Particle Momentum Equation

Newton's law applied to a particle would seem to be a matter understood by every high school physics student. Yet when mass is transferred across the particle boundary, perhaps by devolitilization or as reactants and products of combustion, the incorrect equation is sometimes quoted, the underlying assumptions are usually not fully understood, and the incorrect momentum transfer to the surrounding fluid is sometimes used. The correct equations, surprisingly, do not appear to have been derived until quite recently, when problems of rockets and space travel became important (e.g., Thorpe (1962)). The present derivation roughly parallels that of Panton (1984).

The strategy is to first derive an equation for the i-momentum of the particle, and then differentiate this to find the appropriate equation for mass times acceleration. The equations are written in terms of the location, velocity, and acceleration of the centre of mass, COM, defined by $\bar{R}$ in Fig. 7.

The following symbols are used in the derivation

$$M_p = \int_{v_p} \rho dV \quad = \quad \text{particle mass} \tag{27}$$

$$R_i = \int_{v_p} r_i \rho dV / M_p \quad = \quad i - \text{component of position vector to centre of mass} \tag{28}$$

$$v_i^{C.O.M} = \frac{dR_i}{dt} \quad = \quad \text{velocity of centre of mass} \tag{29}$$

$$P_i = \int_{v_p} \rho u_i dV \quad = \quad i - \text{momentum of particle} \tag{30}$$

The momentum equation for a differential control volume inside the particle is given by Eq. (16).

The starting point for finding the equation for P_i, the particle momentum, involves the use of Leibnitz rule with $f = \rho r_i$ to obtain

$$\frac{d}{dt}\left(\int_{v_p} \rho r_i dV\right) = \int_{v_p} \frac{\partial}{\partial t}(\rho r_i) dV + \int_{s_p} \rho r_i \vec{W} \cdot \hat{n} \rho dS \tag{31}$$

or

$$\frac{d}{dt}(M_p R_i) = \int_{v_p} \frac{\partial}{\partial t}(\rho r_i) dV + \int_{v_p} \frac{\partial}{\partial x_j}(\rho r_i W_j) dV \tag{32}$$

where Gauss' Theorem was used to obtain Eq. (32) from (31).

Mass conservation for the particle is

$$\left(\frac{\partial}{\partial t}(\rho r_i) = r_i \frac{\partial \rho}{\partial t}\right) = -r_i \frac{\partial}{\partial x_j}(\rho u_j) \tag{33}$$

where the spatial derivatives can be written as

$$\frac{\partial}{\partial x_j}(r_i \rho u_j) = \rho u_i + r_i \frac{\partial}{\partial x_j}(\rho u_j) \tag{34}$$

Eliminating the last term in Eq. (33) using (34), and using the resulting equation to eliminate the first term on the RHS of Eq. (31), and expanding the LHS,

$$M_p \frac{dR_i}{dt} + R_i \frac{dM_p}{dt} = \int_{v_p} \rho u_i dV - \int_{s_p} \rho r_i (\vec{V} - \vec{W}) \cdot \hat{n} \rho dS \tag{35}$$